UNIVERSITAT DE BARCELONA

Testing the Standard Model with radiative beauty and rare strange decays at LHCb

Pere Gironella Gironell

Tesi doctoral

Testing the Standard Model with radiative beauty and rare strange decays at LHCb

Autor:

Pere Gironella Gironell

Directors:

Dra. Carla Marín Benito
Dr. Eugeni Graugés Pous

UNIVERSITAT DE BARCELONA

Testing the Standard Model with radiative beauty and rare strange decays at LHCb

Memòria presentada per optar al grau de doctor per la Universitat de Barcelona

Programa de doctorat en Física

Autor:

Pere Gironella Gironell

Directors:

Dra. Carla Marín Benito
Dr. Eugeni Graugés Pous

Tutor:

Dr. Joan Soto Riera

Barcelona

UNIVERSITAT DE BARCELONA

Acknowledgements

En primer lloc, m'agradaria agrair al grup de LHCb a Barcelona, per l'oportunitat que m'han donat, que m'ha permès créixer com a persona. A l'Eugeni i en Lluís, per tot el que han fet durant aquests anys. A la Carla, que no tinc suficients paraules per descriure el meu agraïment, i als companys doctorands, Alejandro, Paula, Aniol i Albert. A la meva família per tot el suport que m'han donat. A tota la gent que he conegut i he fet amistat, tant a la Universitat com al CERN. Finalment, m'agradaria també agrair a tothom que ha fet possible aquesta tesis com a part de la Universitat de Barcelona, de l'ICCUB i de la col·laboració LHCb.

Contents

Resum **v**

1 Introduction **1**

2 The LHCb experiment **3**
2.1 The LHC at CERN 3
2.2 The LHCb experiment 4

3 Theoretical framework **13**
3.1 The Standard Model 13
3.2 The Cabibbo–Kobayashi–Maskawa matrix 15
3.3 Flavor changing neutral currents 16

4 The $K^0_S \to \pi\pi ee$ decay at LHCb **21**
4.1 Introduction 21
4.2 Reconstruction and selection 22
4.3 Invariant mass fit 28
4.4 Understanding the signal yield 29

5 Measurement of the photon polarization in $\Lambda_b^0 \to \Lambda\gamma$ decays **35**
5.1 Introduction 35
5.2 Data samples 38
5.3 Reconstruction and selection 40
5.4 Invariant mass fit 60
5.5 Proton helicity angle 66
5.6 Angular fit strategy 73
5.7 Uncertainties 83
5.8 Results 88
5.9 Conclusions 94

6 Conclusions and future prospects **95**

A Appendix **99**
A.1 Redecay 99
A.2 Agreement between data and simulation 103
A.3 BDT performance plots 109

A.4 BDT efficiency vs invariant mass 113
A.5 Invariant mass fit of the control mode 115
A.6 sFit strategy 116
A.7 Systematic uncertainties pseudo-experiments 120
A.8 Likelihoods and Feldman Cousins 129

Bibliography **133**

Resum

Aquesta tesi doctoral té com a objectiu l'estudi i avaluació del Model Estàndard (ME) de la física de les partícules, mitjançant les dades enregistrades pel detector LHCb. En concret, amb un estudi inicial d'una desintegració rara d'hadrons amb quarks s, $K^0_S \to \pi^+\pi^- e^+ e^-$, i principalment amb l'anàlisi angular d'una desintegració radiativa, $\Lambda^0_b \to \Lambda\gamma$. El Model Estàndard de partícules ha estat extremadament exitós en predir les nombroses mesures realitzades pels experiments, però alhora, també és incapaç d'explicar diversos fenòmens, des de la quantització de la gravetat o la natura dels neutrins fins a donar candidats vàlids pel que es coneix com a matèria i energia fosca. Nous models són desenvolupats contínuament per intentar corregir les mancances del ME, generant noves prediccions en observables que poden ser mesurats experimentalment. Així doncs, mesures de gran precisió poder ser usades per validar nous models.

L'experiment LHCb

Les dades utilitzades en aquesta tesi han estat enregistrades per l'experiment LHCb, un dels quatre grans detectors presents al Gran Col·lisionador d'Hadrons (LHC), situat a l'Organització Europea per a la Recerca Nuclear (CERN), Suïssa. El LHC és l'accelerador circular de partícules més gran del món, amb un anell d'un diàmetre aproximat de 27 km i a una profunditat de 150 m sota terra. Feixos de partícules, típicament protons, però no únicament, s'acceleren circularment en sentits contraris i es fan col·lisionar a grans energies en punts específics de l'anell, a on hi ha situat un detector que n'estudia les col·lisions. Els quatre grans detectors són: ATLAS, CMS, LHCb i ALICE. Els tres primers es centren en col·lisions protó-protó, mentre que l'experiment ALICE es centra en col·lisions de partícules més grosses, com el plom. Els estudis presentats en aquesta tesi usen dades de col·lisions de protons del període conegut com a Run 2, enregistrades durant els anys 2015-2018, a una energia de 13 TeV.

El detector LHCb ha estat dissenyat per estudiar partícules que tenen quarks b i c, amb l'objectiu d'estudiar la simetria de càrrega-paritat, per així entendre l'asimetria entre matèria i antimatèria present a l'univers, i també per examinar el MS fent mesures de decaïments rars. En qualsevol cas, nous programes de física han estat inclosos, des d'estudis de ions pesats, partícules exòtiques o partícules que contenent quarks s. Al LHC, les parelles de quarks (bb, cc) es generen majoritàriament en la direcció dels feixos, per aquest motiu el detector LHCb es va construir com un

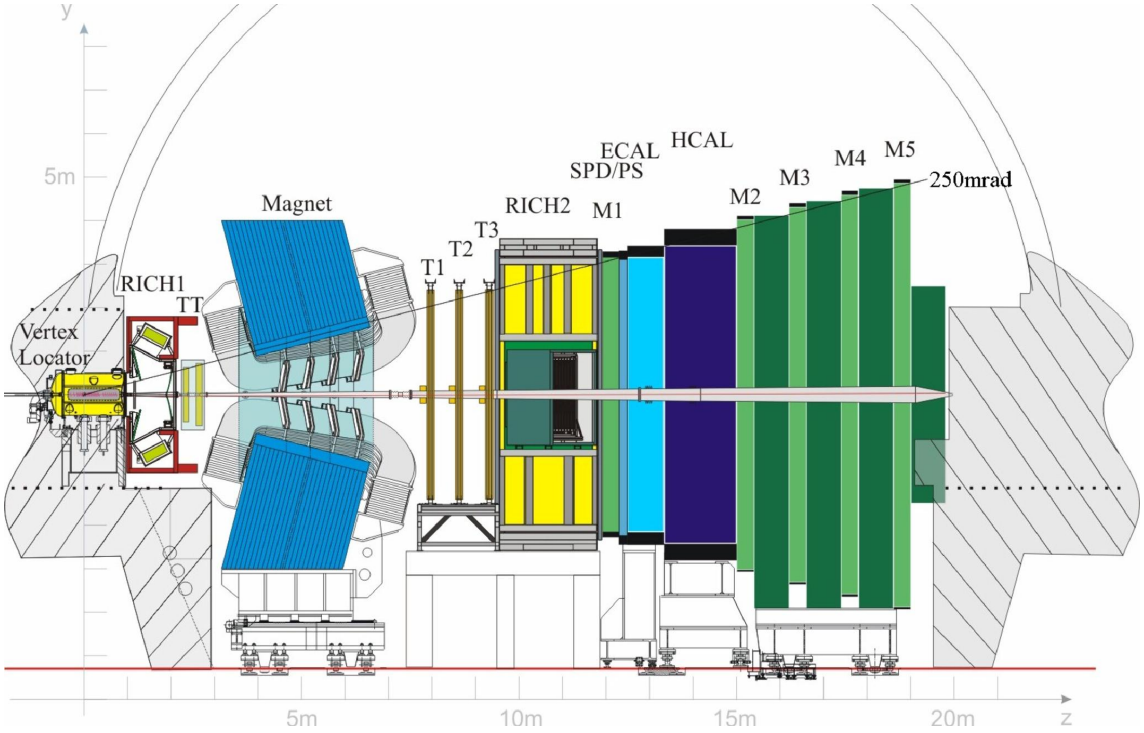

Figura 1: Descripció esquemàtica lateral del detector LHCb.

espectròmetre d'una sola direcció, cobrint un rang de pseudorapidesa de $2 < \eta < 5$, on $\eta = -\ln\left(\tan\left(\frac{\theta}{2}\right)\right)$ i θ és l'angle definit respecte a la direcció del feix. La Figura 1 mostra la secció lateral del detector de manera esquemàtica, on es pot observar que el detector no rodeja tot el punt de col·lisió sinó només una direcció.

El detector està format per diferents subdetectors, agrupats en diferents sistemes depenent de la seva funció. Tres grans sistemes són considerats, el sistema de traçabilitat, el d'identificació de partícules i el conegut com a sistema de "trigger".

El sistema de traçabilitat, com el nom indica, s'especialitza en determinar les trajectòries de les partícules carregades que es produeixen després de la col·lisió. Està format per varis subdetectors començant pel VELO, localitzat al voltant d'on les col·lisions de protons succeeixen amb objectiu de localitzar el vèrtex primari (PV), punt exacte on els protons xoquen, i dels vèrtexs secundaris (SV). Fins a les estacions T que detecten traces després de l'efecte que l'imant té sobre les partícules carregades. El sistema d'identificació de partícules usa els subdetectors RICH, basats en el fenomen Cherenkov, els Calorímetres i les estacions de muons, amb la finalitat de distingir les diferents partícules i obtenir l'energia de partícules no carregades, que no són traçables.

Milions de col·lisions succeeixen cada segon dins de LHCb, i no totes elles són rellevants físicament. Per aquest motiu el sistema de "trigger" fa servir diferents propietats de les col·lisions i de les partícules generades per reduir aquest número de col·lisions a un nivell més assequible per a ser enregistrades. Aquest sistema està format per dos nivells, el conegut com a nivell 0 (L0) i el trigger d'alt nivell (HLT).

El nivell L0 és extremadament ràpid i fa servir decisions basades en mesures dels moments de les partícules, passant així d'una freqüència de 40 MHz a 1 MHz. El HLT és capaç de reconstruir parcialment la col·lisió per reduir aquest número, en dos processos coneguts com a HLT1 i HLT2, finalment arribant a guardar a una freqüència d'entre 10 a 1 KHz.

Marc teòric

Dins el Model Estàndard de la física de partícules ens centrem en processos rars, molt suprimits, coneguts com a Corrents Neutres de Canvi de Sabor (FCNC). En aquesta tesi dos FCNC són estudiats, en el cas del decaïment $K^0_{\rm S} \to \pi^+\pi^- e^+ e^-$ una transició $s \to d\gamma$ i en el cas del decaïment $\Lambda^0_b \to \Lambda\gamma$ una transició $b \to s\gamma$. Aquestes transicions són rellevants perquè estan prohibides al nivell arbre del ME, fet que requereix la presència d'un cercle, "loop", on noves partícules molt massives i no esperades pel ME poden actuar, canviant així diverses propietats de les transicions.

Dos efectes teòrics afecten aquestes transicions a l'hora de fer-ne prediccions, un provinent de la interacció electrofeble en la interrelació entre els quarks, i l'altre amb la interacció forta en el moment de l'hadronització. Per poder tenir en compte els dos efectes, una teoria efectiva s'usa, la coneguda com a Expansió en Productes d'Operadors, que permet agrupar els diferents efectes en els anomenats coeficients Wilson i en operadors locals.

Diversos observables es poden fer servir per buscar efectes no predits pel ME; des de les fraccions de decaïment, observables angulars o la polarització del fotó. En el decaïment de $\Lambda^0_b \to \Lambda\gamma$ l'observable que mesurarem és la polarització del fotó, que en el ME està clarament predita a primer ordre, $\alpha_\gamma = 1$.

El decaïment $K^0_{\rm S} \to \pi\pi ee$ al LHCb

En aquest capítol ens centrem en transicions FCNC del tipus $s \to d\gamma$. En concret en els decaïments de $K^0_{\rm S} \to \ell^+\ell^-\ell^+\ell^-$ que mai s'han observat experimentalment, i que són extremadament suprimits pel ME, amb valors de les fraccions de decaïment de l'ordre de $\mathcal{O}(10^{-10} - 10^{-14})$. Nous models, com models de super-simetria o leptoquarks, prediuen increments en les magnituds d'aquestes fraccions. A més a més, les mesures d'aquests decaïments permetrien obtenir informació de diverses propietats dels decaïments $K^0_{\rm S} \to \gamma\gamma$ i $K^0_L \to \mu^+\mu^-$.

En concret, ens centrarem en el decaïment $K^0_{\rm S} \to \pi^+\pi^- e^+ e^-$ que és un canal de desintegració interesant per entendre els decaïments $K^0_{\rm S} \to \ell^+\ell^-\ell^+\ell^-$. Pel fet que la fracció de decaïment del $K^0_{\rm S} \to \pi^+\pi^- e^+ e^-$ és molt superior, que la seva topologia és similar i degut a la presència de leptons a l'estat final, aquest canal és pot fer servir com a normalització i també és esperable que contribueixi com a decaïment de "fons" (background). Per tots aquests motius l'estudi d'aquest canal és essencial per entendre els $K^0_{\rm S} \to \ell^+\ell^-\ell^+\ell^-$. En aquest estudi es fan servir dades obtingudes per l'experiment LHCb durant 2016 i 2017.

Observació

Els decaïments de mesons K^0_S són molt difícils de reconstruir i seleccionar al detector LHCb, ja que aquests tenen una vida llarga en comparació a la longitud del detector, cosa que provoca que la majoria de K^0_S decaiguin fora del VELO, el subdetector més sensible. El poc moment lineal de les partícules finals, sobretot la parella d'electrons, tampoc facilita la reconstrucció i selecció d'aquest decaïment, a causa de l'efecte Bremsstrahlung. Per aquests motius una reconstrucció i selecció especifica s'usa per seleccionar candidats de $K^0_S \to \pi^+\pi^- e^+ e^-$. En concret es demana que les trajectòries de les partícules deixin traces al VELO, que les traces siguin identificades com a provinents de dos pions i dos electrons i amb una bona qualitat, i un paràmetre d'impacte gran respecte al vèrtex primari, entre altres. A nivell de "trigger", no hi ha línies específiques per aquests decaïments al L0 i a HLT1, però una selecció especifica existeix a HLT2 per poder separar els candidats de senyal dels del fons. Una selecció final elimina el 99.5% dels candidats de fons deixant al voltant d'un 35% de candidats de senyal, procurant eliminar candidats de decaïments reals de fons com són el de $K^0_S \to \pi^+\pi^-$ i $K^0_S \to \pi^+\pi^-\gamma$.

Un cop la selecció és aplicada, es realitza un ajust a la massa invariant del mesó K^0_S per poder extreure'n la quantitat de candidats de senyal i la quantitat de candidats de fons. A la Figura 2 es pot veure l'ajust, on hi ha dues contribucions, una per la senyal i l'altra per un fons combinatori, en forma d'un polinomi de segon ordre. Obtenint així un total de 170 candidats del decaïment $K^0_S \to \pi^+\pi^- e^+ e^-$.

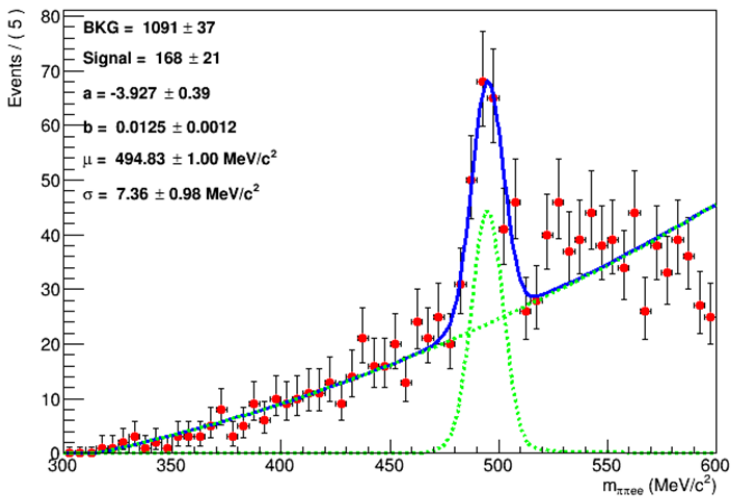

Figura 2: Ajust a la distribució de la massa invariant de K^0_S, després de la selecció per dades obtingudes durant 2016 i 2017 per l'experiment LHCb. Dues contribucions són presents, una pels candidats de senyal i una altra per candidats de fons.

Entenent el decaïment

Un cop realitzada l'extracció dels candidats de senyal és necessari entendre aquest número utilitzant les simulacions. Un pot extreure un número esperat de candidats

com a:

$$N^{exp}_{K^0_S\to\pi^+\pi^-e^+e^-} \sim \mathcal{L}\cdot N(K^0_S/\text{fb}^{-1})\cdot \mathcal{BR}\left(K^0_S\to\pi^+\pi^-e^+e^-\right)\cdot\epsilon^{MC}_{sel} \quad (1)$$

on $\mathcal{L}$ es la lluminositat, $N(K^0_S/\text{fb}^{-1})$ és un número aproximat de mesons K^0_S generats dins de l'acceptància del detector LHCb per fb^{-1}, $\mathcal{BR}\left(K^0_S\to\pi^+\pi^-e^+e^-\right)$ és la fracció de decaïment i ϵ^{MC}_{sel} és l'eficiència de la reconstrucció i selecció a les dades simulades. Tant la lluminositat com la fracció de decaïment són magnituds experimentalment ben conegudes, en canvi, $N(K^0_S/\text{fb}^{-1})\sim 10^{13}$ és un número aproximat i l'eficiència és difícil d'extreure.

L'eficiència extreta les dades simulades pot ser separada en diverses subeficiències. De rellevant importància són les subeficiències del "trigger" i de la identificació de partícules (PID), ja que es coneix que no estan ben reproduïdes a les simulacions. Així doncs, correccions són aplicades a aquestes dues subeficiències, en particular l'eficiència de trigger és recalculada utilitzant un mètode que es coneix com a TIS-TOS, permetent extreure l'eficiència de les mateixes dades. La subeficiència de PID és corregida usant un paquet de programari conegut com a PIDCalib, que fa servir mostres de calibració del detector LHCb per extreure les correccions.

Finalment, s'obté un número de candidats de senyal esperats de 1000, no compatible amb els candidats observats. Aquesta diferència pot ser deguda a uns quants fenòmens, des de l'aproximació utilitzada en $N(K^0_S/\text{fb}^{-1})$, fins a altres correccions que s'haurien d'aplicar a les eficiències extretes de les simulacions. L'ús d'un canal de normalització com el de $K^0_S\to\pi^+\pi^-$ ajudaria a entendre aquesta discrepància.

Mesura de la polarització del fotó a $\Lambda^0_b\to\Lambda\gamma$

En aquest capítol ens centrem en el decaïment radiatiu de $\Lambda^0_b\to\Lambda\gamma$, una FCNC de $b\to s\gamma$. Típicament, aquestes transicions s'han estudiat en decaïments de mesons, però en aquest anàlisi utilitzarem un barió, permeten així explotar el fet que tant l'estat inicial con final tenen un spin no nul. En particular, es fa servir la distribució angular del decaïment del barió Λ a una parella protó-pió, que és sensible a la polarització del fotó, α_γ. Aquest segueix la distribució teòrica següent:

$$\frac{\text{d}\Gamma}{\text{d}\left(\cos\theta_p\right)}\propto 1-\alpha_\gamma\alpha_\Lambda\cos\theta_p \quad (2)$$

on θ_p és l'angle entre la direcció del barió Λ, en el sistema de referència de la Λ^0_b, i la direcció del protó, en el sistema de referència de la Λ. Així doncs, podrem extreure la polarització del fotó fent un ajust a la distribució de l'angle θ_p. Aquest estudi usa dades del detector LHCb durant els anys 2015, 2016, 2017 i 2018 i ha estat publicat a la Ref. [1] i a la nota interna Ref. [2].

En primer lloc, s'han de reconstruir i seleccionar els candidats a $\Lambda^0_b\to\Lambda\gamma$. Aquesta reconstrucció no és trivial a causa de les seves característiques, ja que tant el fotó com el barió Λ són partícules neutres que no deixen traça als diferents

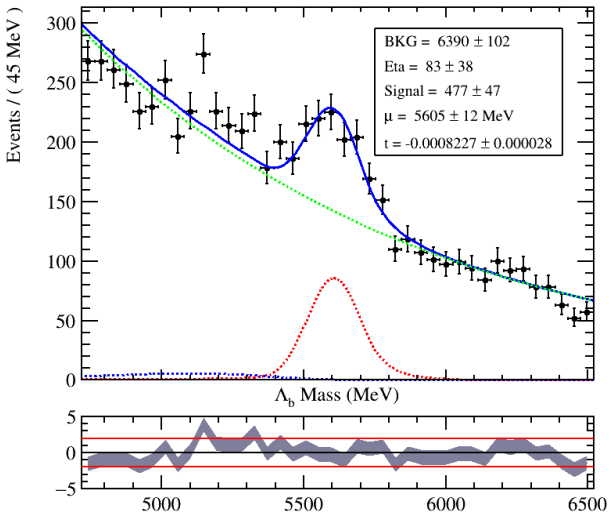

(a)

Figura 3: Ajust a la massa invariant del barió Λ_b^0, utilitzant dades de 2015, 2016, 2017 i 2018. Tres contribucions són considerades; per la senyal, el fons combinatori, i la de candidats parcialment reconstruïts del decaïment $\Lambda_b^0 \to \Lambda\eta$, amb linies de color vermell, verd, i blau puntejat respectivament.

subdetectors. A més a més, la direcció del fotó no és possible de mesurar al LHCb, i el barió Λ és una partícula amb una vida mitjana llarga, cosa que produeix, de manera similar al mesó K_S^0, que majoritàriament decaigui fora del subdetector més precís, el VELO. Això fa impossible la reconstrucció del vèrtex secundari. Per reconstruir i seleccionar candidats s'aprofita i es millora l'estratègia utilitzada per l'observació del decaïment $\Lambda_b^0 \to \Lambda\gamma$, molt recent i també realitzada per l'experiment LHCb.

Selecció i ajust

S'usa una reconstrucció específica per al canal, seguit d'una selecció suau i finalment d'un anàlisi multivariat, fent servir el que es coneix com a "arbre de decisió incrementat" (BDT). Aquest s'entrena amb simulacions per emular la senyal i en dades reals fora de la massa invariant de la Λ_b^0 per simular el fons, separant així les dues contribucions. El resultat de la BDT es maximitza per obtenir la màxima sensibilitat a la polarització del fotó.

Tot seguit es du a terme un ajust a la massa invariant del barió Λ_b^0 per obtenir-ne el número de candidats de senyal i de fons. A la Figura 3 es pot observar l'ajust a la massa invariant, amb tres contribucions, la de candidats de senyal, la de candidats de fons combinatori i finalment una contribució petita de candidats parcialment reconstruïts del decaïment $\Lambda_b^0 \to \Lambda\eta$. Finalment, s'aconsegueix el número de candidats de cada contribució en una finestra reduïda de massa invariant, per fer-ne un anàlisi angular.

Acceptància

Per poder obtenir la polarització del fotó a través de la distribució de l'angle del protó (θ_p) és necessari entendre els efectes que el detector LHCb i la selecció aplicades tenen. Aquests dos efectes són coneguts com a resolució i acceptància. La resolució es la precisió amb que el detector pot determinar el valor d'aquest angle, mentre que l'acceptància és directament l'efecte que la reconstrucció i selecció tenen sobre ell.

Per mesurar la resolució del detector s'usen dades simulades, on es pot estudiar la diferència entre els valors generats del angle del protó amb els valors mesurats pel detector simulat. Els resultats d'aquest estudi mostren que la resolució es pot negligir. Per mesurar l'acceptància, s'utilitzen també dades simulades, on es compara la diferència entre la distribució de l'angle abans de la selecció i després. Aquest efecte no és negligible i s'ha de tenir en compte a l'hora d'obtenir la polarització del fotó. Per comprovar la validesa de les dades simulades, s'utilitza un canal de control, el decaïment de $\Lambda_b^0 \to \Lambda J/\psi$.

Ajust angular i incerteses

Un cop se saben quins afectes s'han de tenir en compte i el número de candidats de senyal i fons a les dades, es pot realitzar un ajust angular per obtenir-ne la polarització del fotó, seguint:

$$\Gamma(\alpha_\gamma;\theta_p) = \frac{S}{S+B}\left[\Gamma_{sig}(\alpha_\gamma;\theta_p)\cdot \mathrm{A}(\theta_p)\right] + \frac{B}{S+B}\Gamma_{bkg}(\theta_p) \tag{3}$$

on S and B són el número de candidats de senyal i fons dins la finestra de massa, $\Gamma_{sig}(\alpha_\gamma;\theta_p)$ és la distribució angular teòrica de $\Lambda_b^0 \to \Lambda\gamma$, $\mathrm{A}(\theta_p)$ és l'acceptància i $\Gamma_{bkg}(\theta_p)$ és la distribució angular dels candidats de fons. L'acceptància es modela amb les dades simulades i la distribució del fons amb dades reals. Aquest ajust es valida amb la realització de pseudo-experiments.

Diverses incerteses sistemàtiques s'han de tenir en compte, provinents de les diferents modelitzacions de les distribucions de l'acceptància i del fons i també de l'ajust a la massa invariant, entre altres. Aquestes incerteses són obtingudes a partir de l'ús de pseudo-experiments. La incertesa sistemàtica mes grossa prové del poc volum de dades utilitzades per modelitzar la distribució angular dels candidats de fons.

La mateixa estratègia es realitza separant els candidats de senyal en candidats de $\Lambda_b^0 \to \Lambda\gamma$ i candidats de $\overline{\Lambda}_b^0 \to \overline{\Lambda}\gamma$, que fins al moment no estaven separats, poden obtenir així mesures de violació de càrrega-paritat.

Resultats

El resultat de l'ajust angular es mostra a les Figura 4 i 5, on es poden observar les contribucions dels candidats de senyal i dels candidats de fons, obtenint així un valor de la polarització del fotó i la corresponent incertesa estadística.

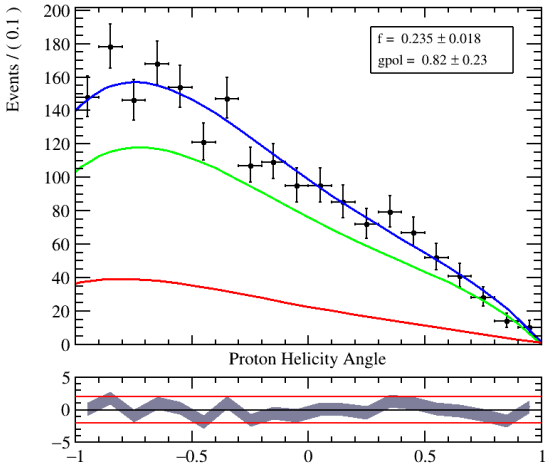

(a)

Figura 4: Ajust angular al cosinus de l'angle del protó. Dues contribucions són observables, provinents de la senyal i del fons.

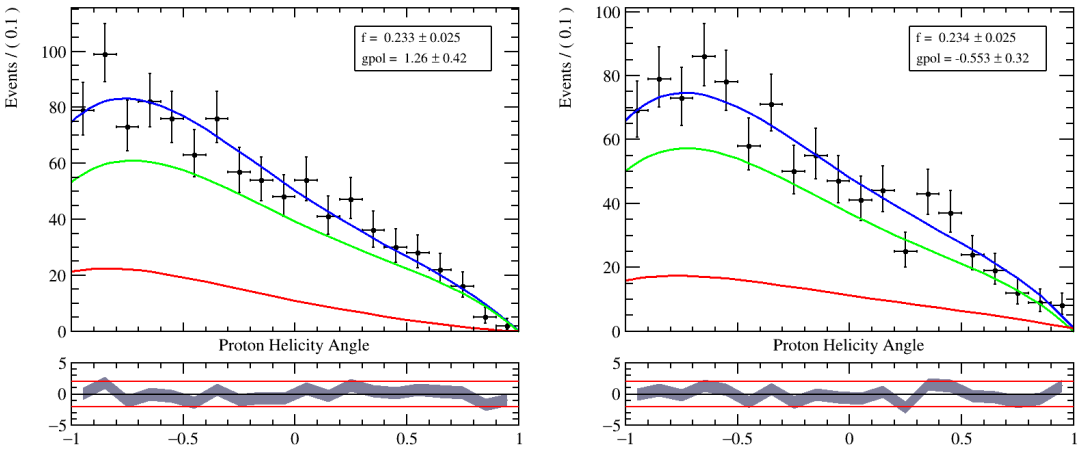

(a) (b)

Figura 5: Ajust angular al cosinus de l'angle del protó per candidats (a) $\Lambda_b^0 \to \Lambda\gamma$ and (b) $\overline{\Lambda}_b^0 \to \overline{\Lambda}\gamma$. Dues contribucions són observables, provinents de la senyal i del fons.

Ara bé, per definició la polarització del fotó està físicament limitada entre els valors de -1 i 1. Així doncs, per tal d'obtenir el valor final de la mesura de la polarització del fotó cal transformar els resultats i les seves incerteses dins del seu rang físic. Per fer-ho s'utilitza el mètode de Feldman-Cousins, que permet aquesta transformació.

Així doncs, el resultat de la mesura de la polarització del fotó que s'obté de les dades combinades és de:

$$\alpha_\gamma = 0.82^{+0.17}_{-0.26}\ (\text{stat.})\ ^{+0.04}_{-0.13}\ (\text{syst.})$$

i el resultat amb les dades separades en $\Lambda_b^0 \to \Lambda\gamma$ i $\overline{\Lambda}_b^0 \to \overline{\Lambda}\gamma$ és de:

$$\begin{aligned} \alpha_\gamma^- &> 0.56(0.44) \text{ at } 90\% \ (95\%) \text{ C.L.}, \\ \alpha_\gamma^+ &= -0.56^{+0.36}_{-0.33}\ (\text{stat.})\ ^{+0.16}_{-0.09}\ (\text{syst.}) \end{aligned}$$

Conclusions

En aquesta tesis s'han explorat dues transicions FCNC sensibles a física més enllà del Model Estàndard, utilitzant dades enregistrades pel detector LHCb durant el període de Run 2. Inicialment amb un estudi del decaïment de $K_S^0 \to \pi^+\pi^- e^+ e^-$, obtenint així la primera observació d'aquest mode dins del detector. En segon lloc, i com a base de aquesta tesis doctoral, s'ha realitzat l'estudi angular del decaïment $\Lambda_b^0 \to \Lambda\gamma$, fet que ha permès l'extracció i la mesura, per primer cop, de la polarització del fotó en una transició amb barions b.

1 Introduction

This thesis presents two analyses performed within the LHCb experiment, studying the decays of $K^0_S \to \pi^+\pi^- e^+ e^-$ and $\Lambda^0_b \to \Lambda\gamma$. Firstly, a preliminary analysis is presented focusing on a rare decay of strange mesons, $K^0_S \to \pi^+\pi^- e^+ e^-$. Secondly, the main focus of this thesis is presented in the form of the angular analysis of the $\Lambda^0_b \to \Lambda\gamma$ decay mode. Which allows to perform the first measurement of the photon polarization of $b \to s\gamma$ transitions in radiative b-baryon decays. These studies are performed using data collected during Run 2 by the LHCb experiment at CERN, at a center of mass energy of 13 TeV.

The goal of these studies is to test the current particle physics theoretical framework, the Standard Model. This theory, aiming to describe the nature of matter and its interactions, has been of great success to describe experimental results, since its conception in mid-late 20^{th} century, while also allowing to predict unobserved properties and particles, such as the existence of the top quark and the recent discovery of the Higgs boson. While highly successful it is also unable to answer many open questions and issues, such as: the inclusion of gravity as a quantized interaction or the oscillating nature of neutrinos. Cosmologically it is also unable to provide with dark matter and dark energy candidates, as required by the current observations, while also incapable of fully explaining the matter-antimatter asymmetry present in the universe. Although, new theories trying to take into account these flaws are continuously tested none has been able to surpass the Standard Model predictions. One of the approaches that tries to overcome the Standard Model is to test specific predictions, that are enhanced by New Physics theories, through the use of precision measurements. The thesis uses this strategy to test the Standard Model in the framework of rare decays of b- and s-hadrons, comprising theoretically highly suppressed decays.

This thesis is organized as follows. An introduction of the LHC and the LHCb experiment is presented in Chapter 2. It introduces the different systems and subsystems used by the LHCb experiment to detect particles and study decay modes of interest. Of extreme relevance are the tracking, particle identification and trigger systems. The tracking system is used to detect charged particle trajectories. The PID system is used to identify the species of the different particles produced in the collisions. Finally, the trigger system is used to be able to select events online, given the huge number of collisions happening at the LHCb collision point.

In Chapter 3, the Standard Model is introduced and specific focus is put on

rare decays, including both radiative and rare strange decays.

An opening analysis is presented in the framework of rare strange meson decays. The K^0_S to four lepton modes are highly interesting due to the huge suppression of their branching ratios, as is predicted by the Standard Model, while new theories can enhance them. In order to understand the characteristics of this highly suppressed transitions at the LHCb experiment, a study of the related but more abundant $K^0_S \to \pi^+\pi^- e^+ e^-$ mode is presented in Chapter 4.

The angular analysis of $\Lambda^0_b \to \Lambda\gamma$ is laid-out in Chapter 5. The helicity structure of this $b \to s\gamma$ transition is studied by exploiting the weak decay of the Λ baryon to a pion and proton pair. The different steps towards the first measurement of the photon polarization in radiative b-baryon decays are presented in the Chapter. Moreover a photon polarization measurement for both $\Lambda^0_b \to \Lambda\gamma$ and $\overline{\Lambda}^0_b \to \overline{\Lambda}\gamma$ is performed and new constraints on the theoretical parameters describing $b \to s\gamma$ transitions are obtained.

Finally, Chapter 6 presents the conclusions of the work done in this thesis, as well as possible improvements and future prospects.

2 The LHCb experiment

This chapter introduces the Large Hadron Collider (LHC) and one of the major experiments present at the collision points: the Large Hadron Collider beauty (LHCb) experiment. The LHCb experiment detector is used for the different analyses presented in this document and is the source of the datasets.

2.1 The LHC at CERN

The LHC is currently the largest and most powerful particle accelerator. It is located at the European Organisation for Nuclear Research (CERN) compound and it consists of a 27 km subterranean ring at the Franco-Swiss border close to the city of Geneva. The ring is composed of several sequences of superconducting magnets and radio-frequency cavities which conform the layout of the circular accelerator.

Inside the circular accelerator, two beams with opposite directions are boosted in separate pipes to reach speeds very close to the speed of light. Upon reaching the required energy they are deflected to collide in set points along the ring. Several experiments make use of the LHC accelerator and are placed along the ring. Four major experiments are set up in four different collision points, these are: ATLAS [3], CMS [4], LHCb [5] and ALICE [6].

The main program of the LHC focuses on accelerating proton beams thus resulting in proton-proton ($p-p$) collisions, but other particles such as heavy ions are also accelerated. The ALICE experiment main physics program is based in these heavy ion collision, while ATLAS, CMS and LHCb mainly focus on $p-p$ collisions. The ATLAS and CMS experiments have been very impactful for the physics community and the current particle physics model for their confirmation of the existence of the Higgs boson [7, 8]. While, the LHCb experiment has had great impact for its results in spectroscopy, tetraquarks and pentaquarks (quite recently), rare decay measurements, CP mixing and violation measurements and lepton flavor universality violation results in heavy flavor physics.

From the start of the LHC program in 2010 increasingly greater center of mass energies ($\sqrt{s}$) have been achieved for the $p-p$ collisions. The energy has increased from 7 TeV during 2010 and 2011 to 8 TeV in 2012, which corresponds to the Run 1 period, and up to 13 TeV from 2015 to 2018 corresponding to the Run 2 period. The proton beams are formed by bunches that cross each other every 25 ns. In

usual LHC runs these crossings are able to provide more than 40 million collisions per second at the different detectors. During the writing of this document, the LHC Run 3 has started and increased the center of mass energy to 13.6 TeV, which was the final energy planned for this circular accelerator.

2.2 The LHCb experiment

The LHCb detector [5,9,10] was designed to study particles containing b or c quarks, both aiming to understand the asymmetry between matter and antimatter present in the current universe and test the Standard Model by measuring rare decays. Nevertheless, the LHCb collaboration has extended its physics program beyond its original objectives to include other particle physics fields; such as exotica searches, heavy ion physics and strange decays, an example of this last field is presented in Chapter 4.

In the LHC, quark pairs (bb, cc) are boosted into the forward and backward directions due to the predominant gluon-gluon fusion mechanism. Therefore, the LHCb experiment was built as a single-arm forward spectrometer to exploit the forward direction. A schematic layout of the LHCb detector is shown in Fig. 2.1. It covers a pseudorapidity range of $2 < \eta < 5$, where $\eta = -\ln\left(\tan\left(\frac{\theta}{2}\right)\right)$ and θ is the angle defined with respect to the beam direction. The detector is formed by various sub-detectors, these are grouped in two main systems; the particle identification (PID) and tracking systems, both used to study the collisions happening at the interaction point. Along these, a trigger system is put in place combining the information from the different sub-detectors to make the decision, in real time, on whether the information of an event should be stored or not. The trigger system is a key component given the huge amount of collisions happening per second at the LHCb interaction point, thus rejecting non-interesting events.

2.2.1 The tracking system

As the name implies, the tracking system is in charge of detecting charged particles tracks. It measures the momenta and reconstructs the trajectory of charged particles produced in the event while also reconstructing the position of the $p-p$ interaction point, generally referred as the primary vertex (PV), as well as the posterior decay vertices, secondary (SV) and tertiary vertices. The system is formed by several sub-detectors; the Vertex Locator (VELO), the Tracker Turicensis (TT), the magnet and the T-stations (T1-T3), these are arranged from the interaction point onwards.

The VELO [11, 12] is located around the interaction point of the proton collisions, beeing is the closest detector to the proton beams in the full LHC system. Its objective is the determination of the PV location and the subsequent vertices, using their corresponding tracks. It is composed by a series of silicon-strip discs placed along the beam pipe (z-direction) and surrounding the interaction region, which provide a measure of the r and ϕ coordinates. The sub-detector is separated into two halves, allowing the VELO to be closed or open depending on whether the beam is set up for physics measurements or it is in an unstable phase. This

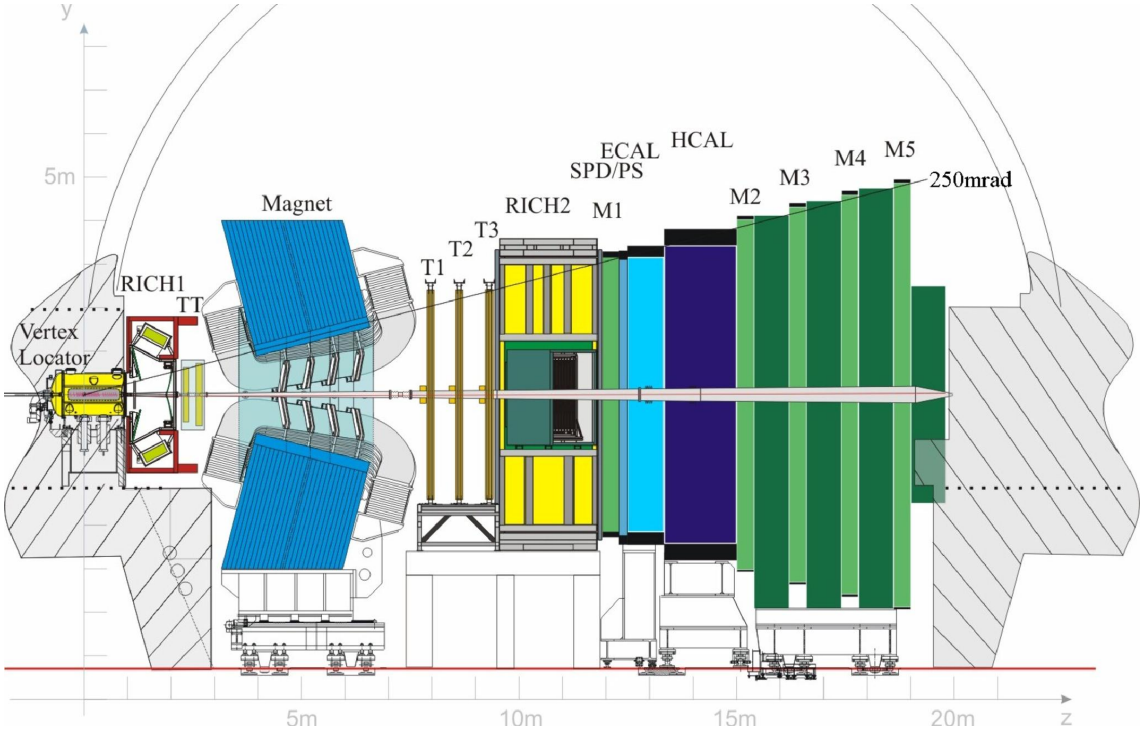

Figure 2.1: Schematic view of the lateral section of the LHCb detector.

system allows the VELO to be very close to the beam pipe, 8 mm, when physics runs are happening, enabling for a very good determination of the PV and track extrapolation. A diagram of the VELO is displayed in Fig. 2.2 (a).

The TT station [13] is located after the VELO and right before the dipole magnet, thus the charged particles have not been greatly affected by the magnet bending force. It is a planar tracking station made of four layers of silicon micro-strip sensors, perpendicular to the beam direction and covering the whole detector acceptance (150 cm wide, 130 cm high). The micro-strip sensor layout changes from one layer to another, with small rotations from the vertical axis for the 2nd and 3rd layers to provide a 3D track reconstruction.

The dipole magnet [14] is used to bend charged particles, thus allowing to measure their momentum and charge. It generates an almost homogeneous magnetic field in the vertical direction with an integrated field magnitude of about 4 Tm. The magnet polarity can be flipped (up-down), therefore allowing to diminish the possible systematic effects arising from detector asymmetries. For this reason, nearly half the data obtained by LHCb is produced with a polarity and the other half with the opposite one.

The T-stations are directly positioned after the dipole magnet and are divided into two regions: the inner tracker [15] and the outer tracker [16]. The inner tracker, which requires higher precision measurements due to the higher occupancy, covers the central part of the station, close to the beam pipe, and follows the same strategy as the TT with silicon micro-strips. The outer tracker is a straw-tube detector, the gas present inside the drift tubes is ionized when charged particles traverse it.

The gases present in the tubes are chosen to have a drift below 50 ns. The outer tracker covers the rest of the detector acceptance which is not covered by the inner tracker.

To reconstruct the particle trajectory the information of the four tracking sub-detectors is used. In particular, and depending on the particle path through the LHCb detector, five type of tracks can be distinguished. These are graphically represented in Fig. 2.2 (b), and are defined as follows:

- Long tracks: These are required to leave hits in the VELO, the TT and the T-stations, thus are able to traverse all tracking sub-detectors. Given that track information is provided by all the tracking sub-detectors, these tracks have the best momentum resolution of all the possible ones.
- Downstream tracks: These are only required to have hits in the TT and T-stations. Since no information is provided by the VELO, they have a worse momentum resolution. These tracks are useful to reconstruct long lived particles (K_s^0, Λ) that happen to decay after the VELO sub-detector.
- Upstream tracks: Tracks only detected by the VELO and the TT. They are typically bent out of the detector acceptance by the dipole magnet, due to their low momentum. They also pass through the Ring Imaging Cherenkov 1 (RICH) and are used as control tracks for PID algorithm.
- T tracks: These only leave hits in the T-stations. Similarly to Upstream tracks, they are used for the PID algorithms given that they also pass through the RICH2 detector.
- VELO tracks: Only detected by the VELO and are typically large-angle or backward tracks. Used to reconstruct the PV location.

Through the different sub-detectors the LHCb tracking system is able to obtain high precision measurements of the track momentum, with resolutions of 0.4% at 5 GeV to 0.6% at 100 GeV (long tracks) [10]. The resolution of the impact parameter (IP) is mostly dependant on the inverse of the transverse momentum of the track, with around 13 μm at very high transverse momentum up to 55 μm at 0.5 GeV. The resolution of the position of the PV is a function of the PV multiplicity resulting in, for example: 13 μm for the X and Y directions and 71 μm for the Z direction in a 25 tracks PV reconstruction.

It is finally worth mentioning that for most LHCb physics analyses only long or downstream tracks are used. In particular, the two analyses presented in this document, in Chapter 4 and Chapter 5, use long tracks given their good momentum resolution.

2.2.2 The PID system

The particle identification system is of extreme relevance for the LHCb detector, given the heavy flavor physics program that LHCb pursues. Requiring very precise identification of the particles arising from the decays of such heavy flavor particles,

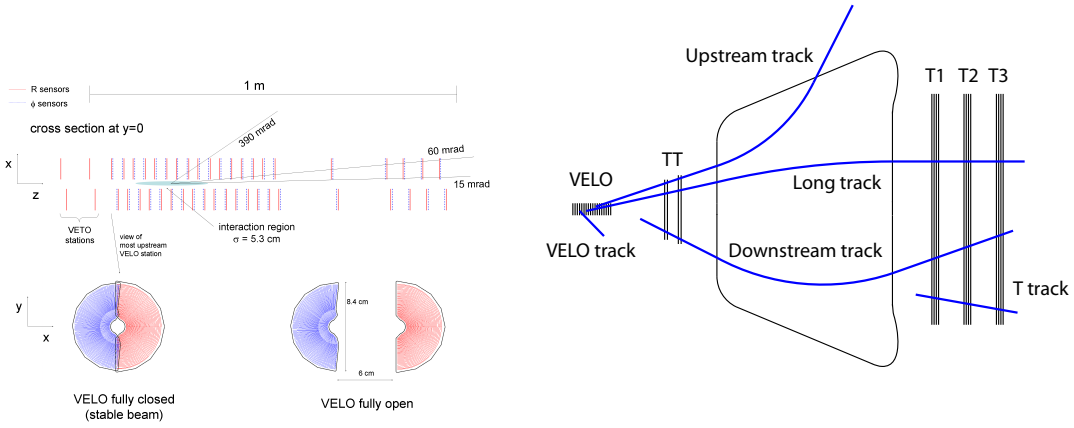

(a) (b)

Figure 2.2: (a) Diagrammatic view of the VELO sub-detector, showing the different modules along the z direction (beam pipe) and the open and closed VELO positions. (b) The LHCb track types are overlaid on top of an schematic representation of the tracking sub-detectors.

i.e. disentangling of different particle final states. This system is composed of different sub-detectors; the two RICH stations, the Calorimeters and the muon stations. The PID information provided by each sub-detector is combined through different processes, such as logarithmic likelihoods, neuronal networks and other multivariate classifiers to obtain a final set of PID identification variables with a high separation power for the different species present at the LHCb experiment.

There are two RICH sub-detectors, namely RICH1 and RICH2 [17]. The first one is placed just after the VELO, while the second one is placed between the T-stations and the Calorimeters. They are based on the Cherenkov effect [18], when a charged particle traverses a dielectric material at a higher velocity than the speed of light in that medium it emits light in a cone, whose angle is proportional to the speed of the traversing particle. The light emitted by the Cherenkov effect is focused and reflected through a complex system of mirrors (Fig. 2.3 (b)), to a detector system outside the LHCb acceptance, enabling the measurement of the cone angle. This information, combined with the momentum measurement done by the tracking systems, enables to measure the mass and charge of charged particles. These completely identify the type of charged particle. In Fig. 2.3 (a) the angle of the Cherenkov light cone is shown depending on the momentum of the particle, for different particle species. To have a broader coverage of possible particle momenta, the RICH1 sub-detector covers a low momentum range of $1 - 60$ GeV/c, while the RICH2 covers a higher momentum range, starting from 15 GeV/c and going beyond 100 GeV/c. This is done by using different gases in each of the RICH detectors, in Run 2 RICH1 uses C_4F_{10} and RICH2 uses CF_4.

The Calorimeter system [19, 20] focuses on providing identification of neutral particles while also measuring their energy. Moreover it also assists with the trigger

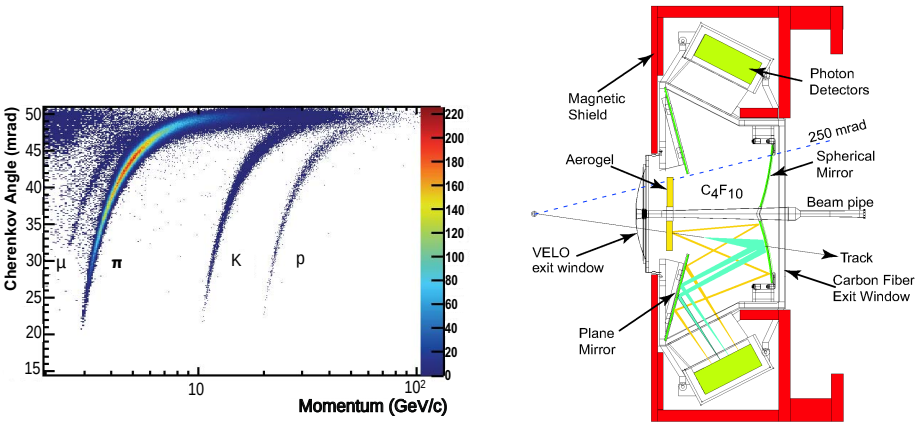

(a) (b)

Figure 2.3: (a) Reconstructed Cherenkov angle for isolated tracks, as a function of track momentum in the medium (C_4F_{10}). The Cherenkov bands for muons, pions, kaons and protons are clearly visible. (b) The LHCb track types are overlaid on top of an schematic representation of the tracking sub-detectors.

system decisions and the PID of charged particles. This system is formed by four sub-detectors placed right after the RICH2 and the first muon chamber, in sequence these are: the Scintillator Pad Detector (SPD), the PreShower detector (PS), the Electromagnetic Calorimeter (ECAL) and the Hadron Calorimeter (HCAL). All sub-detectors are made out of cells whose size is variable and depends on how close they are to the beam pipe, the closer the smaller the cells, due to the higher occupancy in the inner regions. The SPD detects charged particle hits with a fast readout and serves different purposes. The fast readout enables it to be used in the first stages of decision-making of the trigger system, where the SPD occupancy is used as a measure of the event multiplicity. The other major function is the separation of electrons from photons, detected later on by the PS and the ECAL sub-detectors. A layer of lead is situated in between the SPD and the PS, with a 2.5 radiation length (X_0) and is used to start electromagnetic showers. The dispersion of these are measured by the PS and the following calorimeters in order to be able to disentangle electrons from charged hadrons. The ECAL aims to detect electromagnetic particles and measure their energy, it is formed by layers of scintillating material and lead, with a thickness of 25 X_0. The ECAL is designed to have a resolution of:

$$\frac{\sigma(E)}{E} = \frac{10\%}{\sqrt{E\,[\mathrm{GeV}]}} \oplus 1\% \tag{2.1}$$

The HCAL is placed to detect hadrons, which barely interact with the ECAL, and is used for both the trigger system and energy measurements. The HCAL is not able to cover the full length of the hadronic showers, therefore its measured energy is not precise, but it provides a very fast estimate of their energy. It is made of layers of

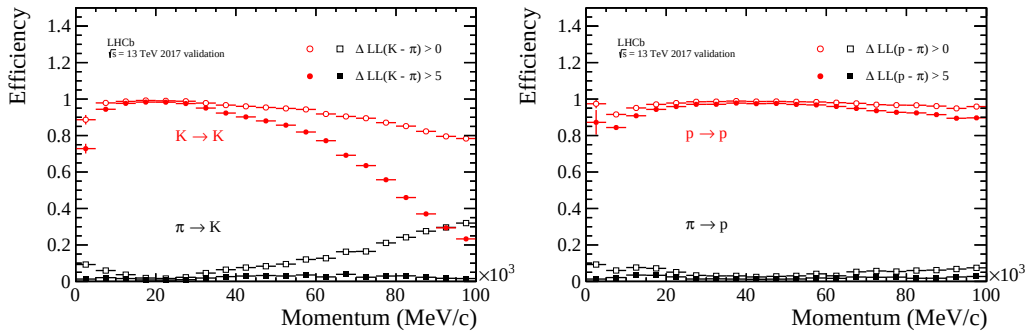

(a) (b)

Figure 2.4: (a) Kaon identification efficiency (red) and pion miss-identification (black) using 2017 data as a function of the track momentum. (b) Proton identification efficiency (red) and pion miss-identification (black) using 2017 data as a function of the track momentum. Two requirements on the difference of a logarithmic likelihood variable are imposed with open and filled markers

scintillating material and iron, and has a resolution of:

$$\frac{\sigma(E)}{E} = \frac{65\%}{\sqrt{E\,[\text{GeV}]}} \oplus 9\% \tag{2.2}$$

The muon stations [21] are composed of five sub-stations, one is placed just before the Calorimeters and the others are placed after the HCAL, M1 and M2-M5, correspondingly. They are rectangular Multi Wire Proportional Chambers (MWPC), with the exception of the center of M1 which uses, Gas Electron Multiplier (GEM) detectors. The muon stations aim is the identification of muons while also doing triggering functions. The positioning of the different stations is done to maximize the interaction probability of muons, since they barely interact with the other subdetectors. The M1 is used as additional input to the p_T measurement for the trigger system. The cell sizes of the muon chambers depend on the their distance with respect to the beam pipe, and M2-M5 stations have the MWPC alternated with layers of iron to increase the muon interaction probability.

The usage of this PID system allows to obtain a very high performance when disentangling different particle species [22]. In Fig. 2.4, the identification efficiency and miss-identification of several species (K, p, π) is presented with respect to the track momentum for a Run 2 sample (2017). Two requirements on the difference of logarithmic likelihoods for the species are imposed. For photons, the resolution of the energy detected by the calorimeters is expected to be around 90 MeV. And a multivariate tool, IsPhoton [23], is able to reach a 95% photon efficiency while rejecting more than 50% of π^0.

2.2.3 The trigger system

The trigger system [24] is designed to select online interesting collisions for the physics program that LHCb pursues from the 40 million of bunch crosses that the

LHC accelerator provides each second (40 MHz). This huge rate needs to be reduced to a manageable level, which has evolved during Run 1 and Run 2. Two sub-systems, from now one referred to as triggers, are put in place to subsequently reduce the rate while keeping the most interesting events, these are: the Level 0 (L0) and the High Level Trigger (HLT). A diagram summarizing the LHCb trigger scheme for Run 2 (2015-onwards) is shown in Fig. 2.5 (a).

The L0 trigger is a very fast hardware based triggering system which reduces the rate from 40 MHz from 1 MHz. Its decisions are driven by momentum measurements, with the information needed to make the decision coming from the different Calorimeter sub-detectors and muon stations. This trigger system has two major disadvantages, the need of a fast response requires simple calculations that lead to a limited precision of the momentum measurements, worse than the offline precision. And lacks flexibility, due to its hardware nature. These two have been solved with the Upgrade of the LHCb trigger system for Run 3

The HLT trigger is a software base triggering system and is further split into two sub-levels, HLT1 and HLT2. The two trigger sub-levels allow to further reduce the rate to $\mathcal{O}(1-10)$ kHz, depending on the data-taking period. The HLT runs separately from the detector in the Event Filter Farm, allowing to be run in a different time-line than the collisions itself. There are differences in the trigger flow during the Run 1 in Run 2, for the purposes of this document, only HLT Run 2 is detailed.

HLT1 does a partial event reconstruction, selecting displaced tracks and vertices, and muon pairs. Most of the software resources during collisions periods are used by the HLT1 and its output is buffered to disk, to be later used by the HLT2. The HLT2 does the full reconstruction of the event, thus allowing for both inclusive and exclusive selections of events. These selections are also referred to as trigger lines throughout this document. During the LHC filling periods, the HLT2 uses most of the computing resources to select physically relevant events saved on the buffer-disks. HLT2 can run asynchronous and is able to archive the same level of reconstruction quality than the offline reconstruction, due to the possibility to perform the alignment and calibration of the detector while collisions are happening (online), in-between the HLT1 and HLT2.

The LHCb experiment Upgrade prepared for Run 3 tackles the issues presented earlier. The hardware part of the L0 system is removed in favour of a fully software-based system, thus greatly improving the flexibility of the whole LHCb trigger system. A summarizing diagram of the Run 3 trigger Upgrade is also shown in Fig. 2.5 (b).

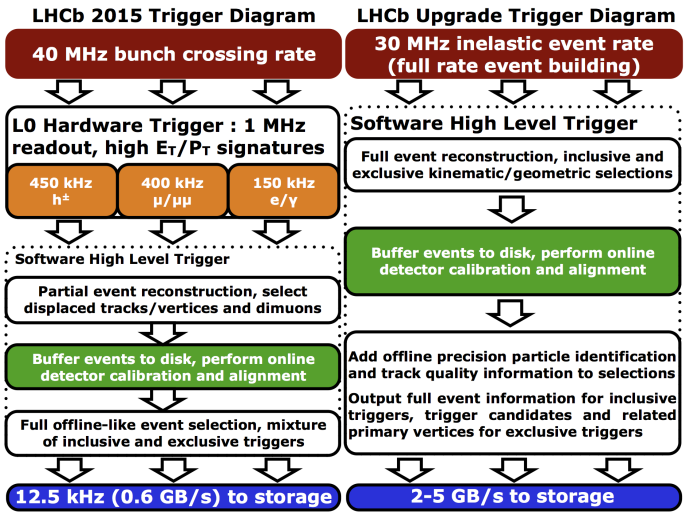

(a) (b)

Figure 2.5: Diagrams of the LHCb trigger for (a) Run 2 and (b) Run 3.

3 Theoretical framework

3.1 The Standard Model

The Standard Model (SM) of Particle Physics [25] is the current established theory describing the foundations of the universe, including the most elementary particles and three out of the four known fundamental interactions; electromagnetic, weak force and strong force. The theory gives mechanisms to predict properties of particles and their interactions, and so far it has been the most successful theory to describe high energy phenomena.

The SM presents the matter in the universe as formed of fermionic particles, which have half-integer spin and thus follow Pauli's exclusion principle. These elements are classified according to whether they interact strongly or not, hence forming two groups; quarks and leptons. Each group includes six particles, which are ordered by their mass. Table 3.1 summarizes the fermion spectrum. It is worth noting that for each particle a corresponding anti-particle exists, thus the SM describes a total of 24 elementary fermionic particles.

Quarks, which interact strongly, are: up (u), down (d), charm (c), strange (s), top (t) and bottom (b). These are grouped in three generations of up-like and down-like quarks, having $2/3$ and $-1/3$ electric charge, respectively. The leptonic particles are: electron (e), muon (μ), tau (τ), electron neutrino (ν_e), muon neutrino (ν_μ) and tau neutrino (ν_τ). Pairs are formed by a lepton and its namestake neutrino. Leptons have an integer charge, electron-like leptons have -1 electrical charge while neutrinos are electrically neutral (0).

The SM also describes the interactions that these elementary particles have, as: electromagnetic, weak or strong interactions. The other known interaction, gravity,

	1st	2nd	3rd	Electric charge
Quarks	u	c	t	$1/3$
	d	s	b	$-2/3$
Leptons	e	μ	τ	1
	ν_e	ν_μ	ν_τ	0

Table 3.1: Fermionic particles in the SM classified by their generation and electric charge

Table 3.2: Interactions in the SM and their associated gauge bosons.

Interaction	Boson
Electromagnetic	γ
Weak	$W^{\pm}$ / Z
Strong	g
Higgs field	H^0

is not included in the SM since it cannot be described as a quantum field theory, the framework used to describe the SM. Nevertheless in the field of particle physics, given the mass of the elementary particles described in the SM, the gravitational force can be neglected in front of the other forces.

The SM describes interactions as the exchange of particles, namely gauge bosons. Each interaction has its own mediating particle, in the form of; the photon (γ) for the electromagnetic interaction, the Z and $W^{\pm}$ bosons for the weak interaction and the gluons (g) for the strong one. These are bosons and have spin 1. Similarly to how the electric charge represents the electromagnetic interaction, the weak interaction has the flavor charge and the strong interaction has the color charge. Quarks have color, flavor and electric charges, while leptons have only flavor and electric charges. The gauge bosons that mediate the interactions are summarized in Table 3.2. The electromagnetic and the weak interactions form a unified interaction at high energies ($\Lambda_{EW} = 246$ GeV), referred to as the electroweak interaction.

The SM is described using a relativistic Quantum Field Theoy (QFT) [26], where particles are defined as excited states of underlying quantum fields and the forces are the interaction terms of the different quantum fields. The SM is a local gauge theory, meaning that there are local transformations of the quantum fields that do not change the physical observables of the theory. The SM symmetry group [27–30] is the group product of

$$SU(3)_C \otimes SU(2)_L \otimes U(1)_Y \tag{3.1}$$

where $SU(3)_C$ is the group corresponding to the color interactions, Quantum Chromodynamics (QCD), and $SU(2)_L \otimes U(1)_Y$ is the electroweak interaction which only couples to left-handed fermions (L). The subscript Y refers to the weak hypercharge, that can be related to the electric charge (Q) and the weak isospin (T_3) as $Y = 2Q - T_3$. This symmetry group is unable to tackle the existence of massive particles, as the corresponding mass terms are not invariant under the electroweak symmetry. To account for this discrepancy, the Higgs mechanism was proposed [31], providing particles with mass through spontaneous symmetry breaking, and thus introducing a new scalar boson field, the Higgs boson. Through this mechanism the fermions and the $W^{\pm}$ and Z bosons [32, 33] become massive while the photon and the gluon remain massless. The Higgs mechanism was confirmed in 2012 by two different collaborations at the LHC experiment by discovering the Higgs boson [7,8], which marked a huge milestone for the SM of Particle Physics.

The SM can be described by the following Lagrangian

$$\mathcal{L}_{SM} = \mathcal{L}_{QCD} + \mathcal{L}_{EW} + \mathcal{L}_{Higgs,Yukawa} \tag{3.2}$$

where $\mathcal{L}_{QCD}$ and $\mathcal{L}_{EW}$ are the QCD and electroweak Lagrangians and the $\mathcal{L}_{Higgs,Yukawa}$ group the self-coupling terms of the Higgs boson and its interactions with the fermions.

Even though the SM is quite a robust theory, several aspects of the universe we live in cannot be described by it. Starting from the previously discussed gravitational force, which cannot be described in a QFT framework; neutrino oscillations, indicative of their massive nature; to the dark matter and dark energy, which the model provides no explanation to. Most relevantly for this document, the SM is able to provide a small matter-antimatter asymmetry, but unable to be compatible with the current measurements of the universe asymmetry by several orders of magnitude. Several extensions of the SM, referred to as Beyond the SM (BSM) models, have been proposed to try to account for these un-answered aspects, such as the minimal left-right symmetric models. But so far no model has been able to overthrow the SM. Therefore, it is necessary to keep searching for New Physics (NP) signs in different physics fields. In this form, high precision measurements of SM observables are of extreme relevance to look for experimental deviations from the SM. One of the experiments focusing on these measurements is the LHCb experiment, which stands as the base of this Thesis. No clear direct signs of NP effects have been observed up to date

3.2 The Cabibbo–Kobayashi–Maskawa matrix

The quantum state of quarks can be represented in two bases, flavor and mass. The corresponding eigenstates can be related through a 3×3 complex unitary matrix, the Cabibbo–Kobayashi–Maskawa (CKM) matrix (V_{CKM}) [34, 35]

$$V_{\text{CKM}} = \begin{pmatrix} V_{ud} & V_{us} & V_{ub} \\ V_{cd} & V_{cs} & V_{cb} \\ V_{td} & V_{ts} & V_{tb} \end{pmatrix} \tag{3.3}$$

where V_{ij} is the complex matrix element that provides the strength of the weak transition from a i quark (up-like) to a j quark (down-like). The total 18 free parameters from a 3×3 complex matrix are reduced to 4 due to the unitary nature of the CKM matrix and the freedom to select the phases of the quarks, thus allowing to reabsorb several of these free parameters. The parameters in the CKM matrix are not predicted by the SM and need to be measured. There are two common parametrizations of the CKM matrix in the literature, in the Wolfenstein one [36], the CKM matrix is defined as:

$$V_{\text{CKM}} = \begin{pmatrix} 1 - \frac{\lambda^2}{2} & \lambda & A\lambda^3 (\rho - i\eta) \\ -\lambda & 1 - \frac{\lambda^2}{2} & A\lambda^2 \\ A\lambda^3 (1 - \rho - i\eta) & -A\lambda^2 & 1 \end{pmatrix} + \mathcal{O}(\lambda^4) \tag{3.4}$$

where A, λ, ρ and η are the four free parameters, with measured values of $A \approx 0.81$, $\lambda \approx 0.225$, $\rho \approx 0.14$, $\eta \approx 0.35$ [37]. The matrix elements are proportional to orders of λ clearly showing a hierarchical structure. The coupling of quarks of the same family, i.e. diagonal terms, are the strongest ($\mathcal{O}(\lambda^0)$), while the coupling of the first family with the third family are the most suppressed ones($\mathcal{O}(\lambda^3)$). The η parameter ($\eta = 0.35$) is the only source of Charge-Parity (CP) violation in the SM. The measurement of the different CKM matrix elements and their relations is essential to validate the SM in the quark sector, thus one of the main goals of the LHCb experiment [38].

It is worth mentioning that a similar mixing matrix is present in the lepton sector, in the form of the Pontecorvo–Maki–Nakagawa–Sakata (PMNS) matrix [39, 40], relating the neutrino eigenstates, i.e. giving rise to neutrino oscillation.

3.3 Flavor changing neutral currents

Rare decays of hadrons are flavor changing neutral transitions, which are highly suppressed by the SM, commonly resulting in very small branching fractions ($< \mathcal{O}(10^{-6})$). They are of particular interest to probe for NP effects, as small contributions from these BSM models may lead to noticeable deviations from their expected properties by the SM. In this Section the focus is put on rare beauty ($b \to s$) and rare strange decays $s \to d$.

Flavor changing transitions require the mediation of $W^{\pm}$ bosons, which forces a change in the electrical charge. Consequently, neutral flavor changing transitions are forbidden at tree level in the SM, but are allowed at the loop-level with an additional flavor change via a virtual quark. These kind of transitions are referred as Flavor Changing Neutral Currents (FCNC) and can be represented using the Feynman diagram in Fig. 3.1. The strength of the different virtual quark diagram contributions is proportional to the square of the virtual quark mass and inversely proportional to the $W^{\pm}$ mass. This suppression is known as the Glashow-Iliopoulos-Maiani (GIM) mechanism [41], which was able to predict the existence of the charm quark before its discovery. The GIM suppression along the hierarchy suppression of the CKM matrix make it so FCNC are good experimental targets to test the validity of the SM and search for BSM physics. One of such cases is the effect that new virtual particles, too massive to be physically created at the current colliders, may have on these kind of transitions.

These transitions are theoretically challenging due to all the different processes that need to be considered and are typically factored into two different contributions. The first one arises from the hadronization process of the quark, i.e. mediated by the strong force, which is also referred in the literature as long-distance contribution. The second one arises from the electroweak interaction itself, and its usually denoted as short-distance contribution. An approach to model them is via the usage of effective Hamiltonians. An effective Hamiltonian describing this transitions can be built using the Operator Product Expansion (OPE) formalism [42], where both long- and short-distance contributions are separated. For the general use case of a b-quark

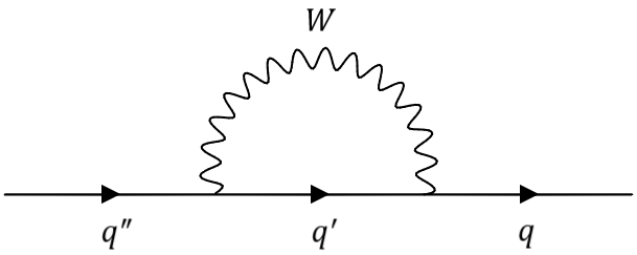

Figure 3.1: Feynman diagram of a general FCNC transition at one-loop level. q, q' and q" correspond to possible quark flavors.

to s-quark FCNC transition:

$$\langle s|\mathcal{H}_{eff}|b\rangle = -\frac{G_F}{\sqrt{2}} V_{\text{CKM}} \sum_i \mathcal{C}_i(\mu)\langle s|\mathcal{O}_i(\mu)|b\rangle \tag{3.5}$$

where G_F is the Fermi constant, $\langle s|$ and $|b\rangle$ are the final and initial states, V_{CKM} are the CKM matrix elements involved and μ is the energy scale. The long-distance contributions are embedded in the local operators, $\mathcal{O}_i$, referencing different possible processes in the transition. The short-distance effects are encoded in the Wilson coefficients $\mathcal{C}_i$. Of particular relevance for rare decays are: $\mathcal{O}_7$, and $\mathcal{O}_{9,10}$, which account for electromagnetic and semi-leptonic processes, respectively. The energy scale, μ, is usually chosen depending on the observable, for rare beauty decays it is set to the bottom quark mass and for the rare strange to the kaon mass.

3.3.1 Rare radiative beauty decays

A case of FCNCs are radiative beauty decays. These correspond to the transition of a b-quark to an s- or d-quarks with the emission of a photon, denoted as $b \to q\gamma$. The effective Hamiltonian for these transitions [43], at first order is:

$$\mathcal{H}_{b\to q\gamma} = -\frac{G_F}{\sqrt{2}} V_{tq}^* V_{tb} \left(\mathcal{C}_7\mathcal{O}_7 + \mathcal{C}_7'\mathcal{O}_7'\right) \tag{3.6}$$

where V_{tq}^* and V_{tb}^* are the corresponding CKM elements, $\mathcal{O}_7$ ($\mathcal{O}_7'$) are the electromagnetic operators proportional to the left (right) projectors [43] and $\mathcal{C}_7$ ($\mathcal{C}_7'$) are the Wilson coefficients (WC), embedding the strength of the left (right) contribution. As noted earlier, only left-handed quarks are subject to the SM electroweak interaction, therefore the only contribution to right-handed currents in the SM is due to chirality flips, proportional to the squared mass of the quarks.

In this document, the focus lies on $b \to s\gamma$ transitions. These are diagrammatically shown in Fig. 3.2, and are more available experimentally than $b \to d\gamma$ transitions, due to the larger CKM suppression of processes from the third family to the first family. In the SM right-handed currents due chirality flips are suppressed by a factor $|r|^2$ (at first order) [44]:

$$|r| = \frac{\mathcal{C}_7'}{\mathcal{C}_7} \approx \mathcal{O}\left(\frac{m_s}{m_b}\right) \approx 0.02 \tag{3.7}$$

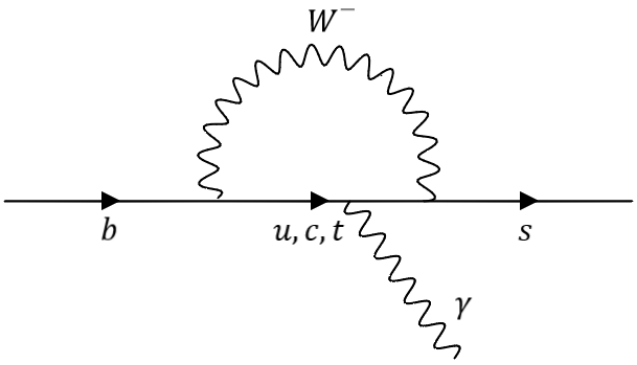

Figure 3.2: Feynman diagram of a general FCNC transition at one-loop level.

where $m_{s,b}$ are the masses of s and b quarks. Given their suppression, the search for right-handed currents in $b \to s\gamma$ is very sensitive to NP effects as BSM models may enhance them. Equivalent transitions of anti-quarks have an opposite suppression as only right-handed anti-quarks couple to the electroweak interaction.

Experimentally, mesonic states of beauty quarks have been used to probe these transitions as they are hugely abundant in the different b-factories. Nonetheless, the LHCb experiment has recently observed and searched for radiative decays of b-baryons [45, 46]. Several observables are able to probe for NP effects: branching fractions, angular observables and the photon polarization itself. With each observable providing with different dependencies on the Wilson coefficients.

Branching fractions information of radiative beauty decays have been experimentally measured with precision at BaBar [47], Belle [48] and by the LHCb experiment [45, 49]. The branching fraction is proportional to $\left|\mathcal{C}_7 + \mathcal{C}_7^{'}\right|^2$, thus allowing to obtain circular constrains in the $\mathcal{C}_7 - \mathcal{C}_7^{'}$ plane. Hence, other complementary observables are required to search for enhancements of right-handed currents. Angular observables sensitive to the photon polarization are able to achieve so, by obtaining complementary dependencies to $\mathcal{C}_7$ and $\mathcal{C}_7^{'}$. Several measurements have been performed by BaBar [50] and also the LHCb experiment [51–53] to different b-meson transitions and angular observables. The study of the virtual photon polarization in $B^0 \to K^{*0}e^+e^-$ decays at very low di-electron invariant mass [54] by the LHCb experiment is of particular relevance as it currently holds the strongest constraint for right-handed currents.

Photon polarization

The photon polarization is a very compelling observable as the photons emitted by $b \to s\gamma$ transitions are predicted to be mostly left-handed in the SM, due to the nature of the electroweak interaction. The photon polarization is defined as the normalized difference of left-handed and right-handed polarized photons:

$$\alpha_\gamma = \frac{N(\gamma_L) - N(\gamma_R)}{N(\gamma_L) + N(\gamma_R)} = \frac{1 - |r|^2}{1 + |r|^2} \tag{3.8}$$

where $|r|$ is presented in Eq. 3.7. The photon polarization is physically bounded from -1 to 1, for fully right- and fully left-handed photons, respectively. At first order the SM predicts $\alpha_\gamma = 1$ [44, 55]. While some observables in radiative b-mesons decays are sensitive to this parameter, no direct measurements have been performed as the helicity structure of such decays is quite complex due to the loss of information on the quark chirality at the hadronization process.

The observation of the radiative b-baryon decay $\Lambda_b^0 \to \Lambda\gamma$, by the LHCb experiment [45], the first of its kind, opened the way to directly measure the photon polarization of this particular baryonic decay. Thus in this document, the first direct measurement of the photon polarization in radiative beauty decays is presented in Chapter 5, by exploiting the rich angular structure of baryonic beauty decays.

3.3.2 Rare strange decays

Another set of interesting rare decays are $s \to d$ FCNC transitions, as they are even more suppressed than rare beauty decays, hence good probes for the SM validity via their precise measurements. Kaon decays in general are theoretically quite challenging given the non-perturbative essence of the long distance effects dominating them [56, 57]. They are usually described in the framework of OPE and Chiral Perturbation Theory (CHPT) [58, 59], for long-distance dynamics. The CHPT allows to systematically expand decay amplitudes in terms of the mass and momentum, enabling the parametrization of the hadronic uncertainties using various low-energy constants. The knowledge on these constants dominates the theoretical prediction uncertainties, which are very diverse for the different decay modes. Rare strange decays are typically dominated by these long-distance dynamics. Nevertheless, it is worth noting that there are decays in the field that are dominated by SD contributions, such as the $K \to \pi\nu\overline{\nu}$, considered a golden mode due to its clean theoretical predictions.

Of relevance for this document are the decays of $K^0_{S(L)} \to \ell^+\ell^-\ell^+\ell^-$ which are expected to be dominated by long-distance effects, and fully related to the effects in the decays of $K^0_{S(L)} \to \gamma\gamma$. These four lepton final state decay modes can also be used to predict short-distance effects on $K^0_L \to \mu^+\mu^-$ by resolving the ambiguous sign of $\mathcal{A}\left(K^0_L \to \gamma\gamma\right)$ [60, 61]. The predicted branching fraction for the $K^0_{\rm S}$ meson modes are [61]:

$$\mathcal{B}\left(K^0_{\rm S} \to e^+e^-e^+e^-\right) \sim 1 \cdot 10^{-10} \tag{3.9}$$

$$\mathcal{B}\left(K^0_{\rm S} \to \mu^+\mu^-e^+e^-\right) \sim 8 \cdot 10^{-12} \tag{3.10}$$

$$\mathcal{B}\left(K^0_{\rm S} \to \mu^+\mu^-\mu^+\mu^-\right) \sim 1 \cdot 10^{-14} \tag{3.11}$$

Given the small branching fraction these present, these modes are experimentally challenging to observe. Nevertheless, BSM can greatly enhance their magnitude, thus both upper limit measurements and observations of these modes may help determine possible NP effects.

In Chapter 4 a point of entry is presented for the study of these never-seen modes, by analyzing the $K^0_{\rm S} \to \pi^+\pi^-e^+e^-$ transition, much less suppressed in the SM and thus much more available in the experimental sites.

4 The $K^0_S \to \pi\pi ee$ decay at LHCb

4.1 Introduction

Even though the main focus of the LHCb experiment are particles containing b- or c-quarks, due to its huge production, particles with s-quarks are highly abundant. Which allowed the LHCb experiment to obtain relevant results in the field of rare strange decays. Most relevantly, the world-best measurements of the branching ratio of $K^0_S \to \mu^+\mu^-$ [62–64], which has been sequentially improved with the addition of more LHCb data. Also the measurement of the branching ratio of $\Sigma \to p\mu^+\mu^-$ decays [65] with a significance of 4.1σ, using only Run 1 data.

Of interest are the very rare strange decays, $K^0_S \to \ell^+\ell^-\ell^+\ell^-$, which are FCNC processes that have never been experimentally observed before. In the SM, these decays are highly suppressed with predicted branching fractions of the order $\mathcal{O}(10^{-10})$ for $K^0_S \to e^+e^-e^+e^-$ and down to $\mathcal{O}(10^{-14})$ for $K^0_S \to \mu^+\mu^-\mu^+\mu^-$ decays as presented in Chapter 3. Beyond the SM models can predict large enhancements of the branching fractions, such as SUSY models [66], Leptoquarks models [67,68] and dark-sector benchmark models [69]. Thus experimental anomalies might indicate the presence of NP effects. Additionally, the measurements of both K^0_S and K^0_L decays into four leptons would allow to measure the unknown sign of the amplitude, $\mathcal{A}(K^0_L \to \gamma\gamma)$ [60, 61], enabling to precisely predict the short-distance contribution to $K^0_L \to \mu^+\mu^-$ decays.

The $K^0_S \to \pi^+\pi^-e^+e^-$ mode is of particular interest for the study of $K^0_S \to \ell^+\ell^-\ell^+\ell^-$ as it can be used as a normalization channel for such decays while also being a possible background source given the similar topology and the presence of leptons as final state particles, the electron pair. Specifically, final states with low-energy electrons are of extreme difficulty to reconstruct and to properly calibrate the efficiencies due to the high-energy losses produced by the Bremsstrahlung effect. For both motives, the usage of the $K^0_S \to \pi^+\pi^-e^+e^-$ decay as proxy to study the highly suppressed fully-leptonic decays is ideal given its comparatively high abundance, $\mathcal{B}(K^0_S \to \pi^+\pi^-e^+e^-) = (4.7 \pm 0.7 \pm 0.4) \times 10^{-5}$ [37]. In addition, $K^0_S \to \pi^+\pi^-e^+e^-$ candidates are expected to be important background contributions to the $K^0_S \to e^+e^-e^+e^-$ and $K^0_S \to \mu^+\mu^-e^+e^-$ analyses.

In this chapter, a preliminary study of the $K^0_S \to \pi^+\pi^-e^+e^-$ decay using data obtained by the LHCb experiment is laid-out. The study uses LHCb datasets from 2016 and 2017 data-taking periods. Collisions from 2018 were unavailable at the

start of this study and thus not used thereafter. Data from Run 1 is not used due to the lack of a proper trigger configuration, hugely impacting the availability to select $K^0_S \to \pi^+\pi^-e^+e^-$ events at the trigger level during that period. A study of the $K^0_S \to \pi^+\pi^-e^+e^-$ decay mode using Run 1 by the LHCb experiment is presented in Ref. [70], which prompted the creation of a new trigger line for the Run 2 data-taking period, able to reconstruct and select $K^0_S \to \pi^+\pi^-e^+e^-$ candidates online. The study presented in this Chapter uses dedicated online and offline selections to be able to discriminate signal from background candidates. A maximum likelihood fit is performed to the K^0_S invariant mass to extract the signal yield from the data samples. The expected yield for the $K^0_S \to \pi^+\pi^-e^+e^-$ is extracted from efficiency computations using the simulation samples, taking into account the recorded luminosity and the branching ratio. The obtained yield is studied to match the yield obtained from the real data collisions.

4.2 Reconstruction and selection

Decays of K^0_S mesons are difficult to reconstruct and select due to the long lifetime they present with respect to the LHCb experiment and the small transverse momentum the final states carry. Typically, K^0_S candidates decay outside the VELO sub-detector. Therefore tracks of its decay products are mostly reconstructed as downstream tracks ($\sim 65\%$), which have a much worse momentum resolution than long tracks. For this reason, the study imposes that the K^0_S candidate is formed of four long tracks. As a general overview of both online and offline selections, the K^0_S candidate is reconstructed from four tracks identified as two pions (π) and two electrons (e) with good track quality, low ghost probability and large impact parameter (IP) with respect to the PV. It also imposes that that the maximum distance of closest approach (DOCA) between all pairs of tracks is small, coherent with four particles coming from from the same vertex (SV). The reconstructed K^0_S trajectory has to be compatible with originating from the PV and having a good vertex quality while imposing a small maximum invariant mass.

Bremsstrahlung corrections are set in place at the reconstruction step in order to account for the energy losses of the electrons. Each electron track has an associated Calorimeter region, depending on their trajectory. Photons detected in these regions are considered to be possible Bremsstrahlung candidates of the corresponding track [71]. It is worth noting that low-energy electrons produce even lower-energy photons which cannot be detected by the LHCb experiment. In particular, the detector can only detect photons with transverse momentum higher than 75 MeV/c, therefore some energy is missed due to this effect. In opposition, overcorrections to the energy may occur due to miss-association of photons to electron tracks. For the K^0_S candidate reconstruction and selection, both electron tracks are treated so they are unable to share the same associated Bremsstrahlung photon, avoiding potential excessive corrections.

L0	HLT1
L0Muon	Hlt1TrackMVA
L0MuonNoSPD	Hlt1TwoTrackMVA
L0DiMuon	Hlt1TrackMVALoose
L0DiMuonNoSPD	Hlt1TwoTrackMVALoose
L0Electron	Hlt1TrackMuon
L0ElectronHi	Hlt1TrackMuonMVA
L0ElectronNoSPD	Hlt1DiProton
L0Hadron	Hlt1DiProtonLowMult
L0HadronNoSPD	Hlt1B2PhiGamma_LTUNB
L0HighSumETJet	Hlt1B2GammaGamma
L0Photon	Hlt1SingleElectronNoIP
L0PhotonHi	Hlt1SingleMuonNoIP
L0PhotonNoSPD	Hlt1SingleMuonHighPT
	Hlt1DiMuonLowMass
	Hlt1DiMuonHighMass
	Hlt1DiMuonNoL0
	Hlt1DiMuonNoIP
	Hlt1B2HH_LTUNB_PiPi
	Hlt1B2PhiPhi_LTUNB
	Hlt1MultiDiMuonNoIP
	Hlt1MultiMuonNoL0
	Hlt1Bottomonium2PhiPhi
	Hlt1Bottomonium2KstarKstar

Table 4.1: List of trigger lines at L0 and HLT1 step used for the $K^0_S \to \pi^+\pi^-e^+e^-$ online selection

Trigger selection

The trigger selection is based on the triggering steps presented in Sec. 2.2.3. No specific trigger lines are in place at L0 and HLT1 to select $K^0_S \to \pi^+\pi^-e^+e^-$ candidates. An unusual approach to select as much candidates as possible is used. In each $p-p$ collision at the LHC, multiple K^0_S mesons are expected to be produced. Therefore, other physically interesting events, which are triggered, and thus saved, by the LHCb experiment, contain several K^0_S mesons. Hence, the $K^0_S \to \pi^+\pi^-e^+e^-$ candidates used in this study are reconstructed and selected from other triggered events, as underlying decays. For this purpose the Trigger independent of Signal (TIS) is required on any of various L0 and HLT1 lines, meaning that the event has not been triggered by the signal mode ($K^0_S \to \pi^+\pi^-e^+e^-$) but due to other particles present in the collision. The list of trigger lines used is displayed in Table 4.1. Due to the huge amount of trigger lines chosen and the TIS requirement, the selection is expected to be K^0_S decay independent, meaning that the efficiency to select a K^0_S meson is independent of the final state. Thus the same efficiency is expected for $K^0_S \to \pi^+\pi^-e^+e^-$ and, for example $K^0_S \to \pi^+\pi^-$ decays, at this stage.

At the HLT2 stage the line `Hlt2DiElectronElSoft` is used to select $K^0_S \to$

Variable	Units	Requirement
Track χ^2_{IP}		< 1000
Track ProbNNe		> 0.1
Tracks sum of Ghost Prob.		< 0.1
Tracks product of $(\chi^2_{\text{IP}} - 16)$		> 2000
Tracks product of IP	mm^2	> 0.8
Tracks DOCA	mm	< 0.2
Tracks cos(Angle)		< 0.999997
K^0_S Vtx Z - PV Z	mm	> 0
K^0_S IP/(Vtx Z - PV Z)		< 0.02
K^0_S Vtx Z	mm	< 600
K^0_S Vtx $(X^2 + Y^2)$	mm^2	< 36
K^0_S DIRA		> 0
K^0_S M	MeV/c^2	< 1000

Table 4.2: Requirements included in the `Hlt2DiElectronElSoft` trigger line.

$\pi^+\pi^-e^+e^-$, imposing a Trigger on Signal (TOS) requirement. The line was implemented at the start of Run 2 and thus was not present in Run 1. It selects two tracks consistent with an electron pair and originating from a good quality vertex displaced from the PV. The invariant mass of the parent particle is required to be small and its trajectory consistent with originating close to the PV. Details on the HLT2 selection can be found in Table 4.2.

Offline selection

Two offline selections steps are used, the stripping and a final selection. Both follow the same overall strategy as the trigger with tighter requirements. Additional cuts are applied to the pion tracks. Transverse momentum requirements are imposed to the pions along with a small ghost probability, small DOCA and being incompatible with a kaon hypothesis. The stripping selection is referred as `StrippingKshort2eePiPi_eeFromTracks` and is found in Table 4.3.

After the stripping step, no indication of $K^0_S \to \pi^+\pi^-e^+e^-$ candidates can be observed in data, as can be seen in Fig. 4.1, showing the K^0_S invariant mass window of $300 - 600$ MeV/c^2. The final selection follows the previous steps with even tighter requirements and removes possible physical background contributions. The cuts imposed at the selection level are detailed in Table 4.4. The values of these cuts are selected by comparing $K^0_S \to \pi^+\pi^-e^+e^-$ simulated signal candidates and background candidates extracted from the data high mass side bands (> 600 MeV/c^2) once the stripping selection is imposed.

Two physical background contributions are vetoed by imposing requirements to the invariant masses of the electron and pion pairs. Specifically these are background candidates coming from $K^0_S \to \pi^+\pi^-\gamma$ and $K^0_S \to \pi^+\pi^-$ decays. The photon candidate in the $K^0_S \to \pi^+\pi^-\gamma$ decay mode can interact with the detector material to result in the same final state as the signal mode, i.e. $\gamma \to e^+e^-$. Therefore a

Variable	Units	Requirement
e p_{T}	MeV/c	> 100
e χ^2_{IP}		> 16
e Ghost Prob.		< 0.5
e PIDe		> -4
π p_{T}	MeV/c	> 100
π Ghost Prob.		< 0.5
π PIDK		< 5
e^+e^- Mass	MeV/c^2	< 5000
e^+e^- p_{T}	MeV/c	> 200
Tracks(π) DOCA	mm	< 1
K^0_{S} IP	mm	< 1
K^0_{S} M	MeV/c^2	< 800
K^0_{S} τ	ns	> 0.08953
K^0_{S} Vtx χ^2		< 50

Table 4.3: Stripping selection used for the $K^0_{\mathrm{S}} \to \pi^+\pi^-e^+e^-$ studies.

requirement is imposed to the dielectron invariant mass to reject candidates compatible with a null invariant mass. Additionally, two electron tracks arising from the underlying event can be combined with a $K^0_{\mathrm{S}} \to \pi^+\pi^-$ decay to obtain the same final state. Consequently, a cut is imposed to the invariant mass of the pion pair to reduce this background contribution, as the $K^0_{\mathrm{S}} \to \pi^+\pi^-$ mode is the primary decay channel of K^0_{S} mesons. The presence of these two physical background contributions can be directly observed in data after the stripping step. In Fig. 4.2 (a) a significant amount of candidates is present very close to the null dielectron invariant mass, consistent with arising from a photon. For the $K^0_{\mathrm{S}} \to \pi^+\pi^-$ background contribution, (Fig. 4.2 (b)), a peak is observed in the pion pair invariant mass distribution compatible with the K^0_{S} mass hypothesis.

This final selection step, including the vetoes, is able to reject 99.95% of background candidates while keeping around 35% of signal candidates. It is worth pointing out that after the different selection steps, the already small simulated samples are reduced considerably.

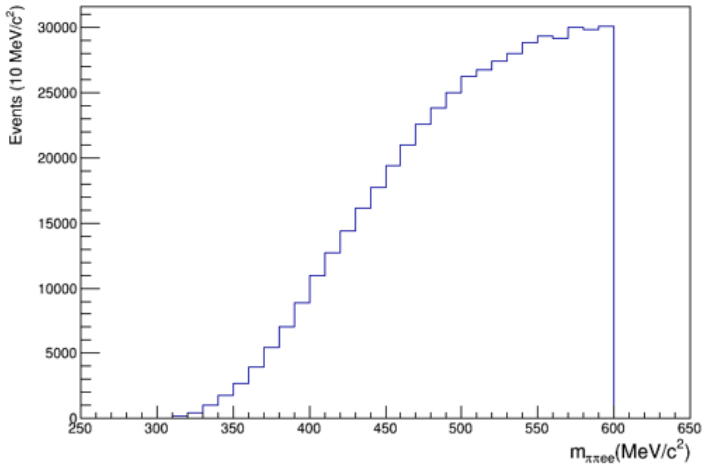

Figure 4.1: Invariant mass distribution $(300 - 600\ \text{MeV}/c^2)$ of the reconstructed K^0_S data candidates for 2016. The stripping selection is imposed.

Variable	Units	Requirement
e ProbNNe		> 0.5
π ProbNNπ		> 0.5
e^+e^- M	MeV/c^2	< 200
e^+e^- M	MeV/c^2	> 20
$\pi^+\pi^-$ M	MeV/c^2	< 470
K^0_S IP	mm	< 0.4
K^0_S χ^2_{IP}		< 15
K^0_S DIRA		> 0.9999995
K^0_S χ^2_τ		< 15
K^0_S (Vtx Z- PV Z)·M/p_Z	mm/c	> 2

Table 4.4: selection requirements to K^0_S candidates after the stripping selection.

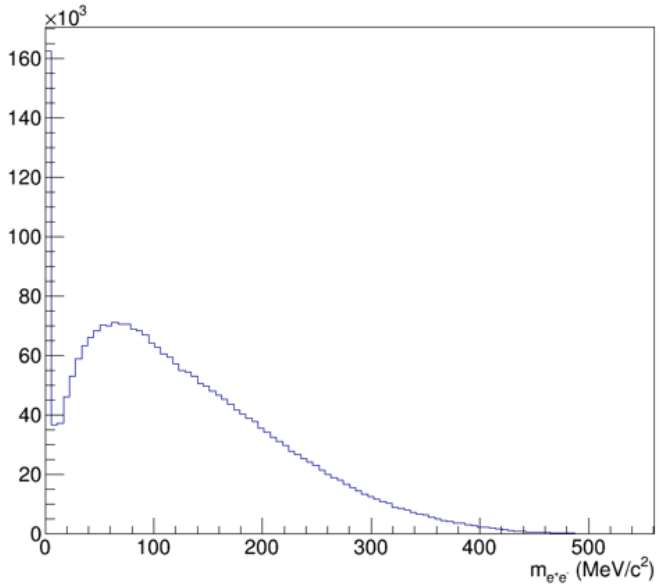

(a)

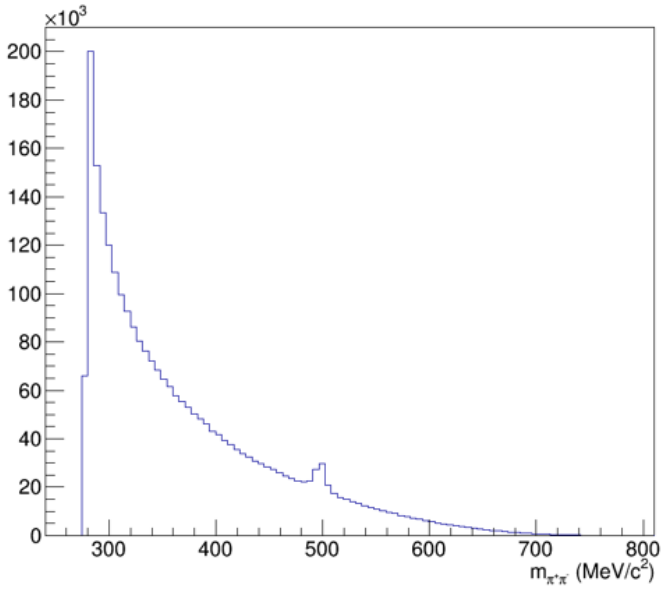

(b)

Figure 4.2: Invariant mass distributions of the (a) electron pair and (b) pion pair corresponding to the 2016 period of data-taking. The stripping selection is imposed. Notice the peak of events at (a) $m_{ee} \sim 0$ corresponding to a photon-like invariant mass and at (b) $m_{\pi\pi} \sim 500$ corresponding to a K_s^0-like invariant mass.

4.3 Invariant mass fit

After the selection, a disentanglement of the signal candidates from the remaining combinatorial background candidates is essential to extract the signal yield. To do so, an unbinned maximum likelihood fit is performed to the candidates K^0_S invariant mass distribution, in the $300 - 600$ MeV/c^2 range.

The invariant mass distribution of the signal contribution is modeled as a double-sided Crystal Ball, previously described in detail in Eq. 5.9, to account for effects, such as the energy lost due to Bremsstrahlung, affecting the tails of the invariant mass distribution. The tail parameters of the distribution $(n_L, n_R, \alpha_L, \alpha_R)$ are fixed using a fit to the simulation samples, to reduce the number of free parameters in the fit to data. The mean and width of the Gaussian core (μ, σ) are allowed to be free in the fit to data. The combinatorial background is modeled using a second order polynomial, with both parameters (a, b) free to vary in the fit to data. The selection step removed the two more dangerous partially reconstructed backgrounds, thus no other background sources are considered.

The result of the invariant mass fit to the 2016 and 2017 data-taking periods is shown in Fig. 4.3. The values of the parameters are displayed Table 4.5 along with the signal and background yields. A clear peak can be observed, compatible with the K^0_S invariant mass. The combinatorial background contribution is observed to increase along the invariant mass, as expected, due to the combinatorial increase of the four tracks at higher energies. The signal yield is found to be:

$$N_{sig} = 170 \pm 20 \tag{4.1}$$

μ (MeV/c^2)	495 ± 1
σ (MeV/c^2)	7 ± 1
p_0	-3.9 ± 0.4
p_1	0.0125 ± 0.0012
N_{sig}	168 ± 21
N_{comb}	1091 ± 37

Table 4.5: Parameters of the invariant mass fit to data candidates of 2016 and 2017 data-taking periods for the $K^0_S \to \pi^+\pi^-e^+e^-$ study.

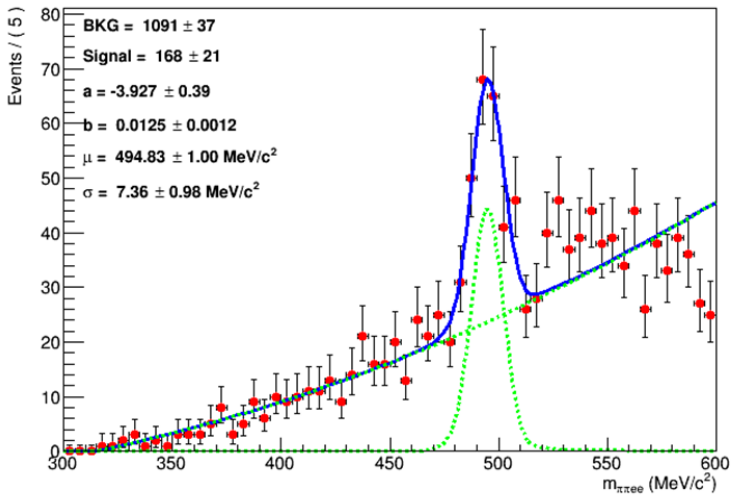

Figure 4.3: Invariant mass distribution of K^0_S candidates corresponding to the 2016 and 2017 periods of data-taking after all selection steps are imposed. The result of the invariant mass fit is overlaid. The total PDF is represented by the solid blue curve, while the signal and combinatorial background are displayed by dashed green lines.

4.4 Understanding the signal yield

The goal of this study is to do the first analysis of the $K^0_S \to \pi^+\pi^-e^+e^-$ decay inside the LHCb experiment, to be used to analyze rarer decay modes with similar topology. To do so, the expected number of $K^0_S \to \pi^+\pi^-e^+e^-$ is extracted using the simulated samples. The branching ratio of the $K^0_S \to \pi^+\pi^-e^+e^-$ decay mode has been measured with high precision by NA48 [37], thus the signal yield obtained from the data candidates is expected to match the yield extracted from the simulated samples. The expected yield can be expressed as:

$$N^{exp}_{K^0_S\to\pi^+\pi^-e^+e^-} = \mathcal{L}\cdot\sigma_{pp}\cdot f_{K^0_S}\cdot\mathcal{BR}\left(K^0_S\to\pi^+\pi^-e^+e^-\right)\cdot\epsilon^{MC}_{acc}\cdot\epsilon^{MC}_{sel} \tag{4.2}$$

where $\mathcal{L}$ is the luminosity for each data-taking period, σ_{pp} is the $p-p$ cross-section, $f_{K^0_S}$ is the K^0_S hadronization fraction and $\mathcal{BR}\left(K^0_S\to\pi^+\pi^-e^+e^-\right)$ is the $K^0_S \to \pi^+\pi^-e^+e^-$ branching ratio and ϵ^{MC}_{sel} is the efficiency of the selection and reconstruction in the simulation samples. In particular, during Run 1 the number of K^0_S produced inside the LHCb acceptance per fb^{-1} was estimated to be of the order of $N(K^0_S/\text{fb}^{-1}) \sim 10^{13}$. While the number depends on the center-of-mass energy of the collisions, its dependence is expected be small. Thus, the rough approximation is expected to still hold for Run 2, with a K^0_S-meson cross section of round 0.3 barn, further discussed in Ref. [72]. The expected yield presented in Eq. 4.2 can be rewritten as:

$$N^{exp}_{K^0_S\to\pi^+\pi^-e^+e^-} \sim \mathcal{L}\cdot N(K^0_S/\text{fb}^{-1})\cdot\mathcal{BR}\left(K^0_S\to\pi^+\pi^-e^+e^-\right)\cdot\epsilon^{MC}_{sel} \tag{4.3}$$

where ϵ^{MC}_{sel} does not include the LHCb acceptance efficiency, as it is implicitly included in $N(K^0_S/\text{fb}^{-1})$. In Table 4.6 the values of the different parameters of Eq. 4.3

$\mathcal{L}$	3 fb^{-1}
N(K^0_S/ fb^{-1})	10^{13}
$\mathcal{BR}\,(K^0_S \to \pi^+\pi^- e^+ e^-)$	$(4.79 \pm 0.15) \cdot 10^{-5}$

Table 4.6: Values of the different inputs to the computation of the expected yield.

Selection	Efficiency (ϵ)
Reco. & Strip.	$(2.80 \pm 0.04) \cdot 10^{-4}$
Trigger	$(8.9 \pm 0.7) \cdot 10^{-2}$
Mass window	0.97 ± 0.10
Final Selection	0.36 ± 0.05

Table 4.7: Efficiencies of the different selection steps. Directly extracted as the ratio of yields for each step using the simulated samples.

are shown. It is worth noting that the luminosity is smaller than the total 2016 and 2017 luminosity due to the unavailability to access several datasets during the time the study was being completed. The computation of the different selection efficiencies is discussed next.

Efficiency calculation

The total selection efficiency can be expressed as:

$$\epsilon_{finalsel.} = \epsilon_{reco,strip} \cdot \epsilon_{trig} \cdot \epsilon_{mass} \cdot \epsilon_{sel} \tag{4.4}$$

where $\epsilon_{reco,strip}$ is the efficiency of the reconstruction algorithms and the stripping selection, ϵ_{trig} is the online selection efficiency, namely trigger, ϵ_{mass} is the efficiency after imposing the invariant mass window and ϵ_{sel} is the selection efficiency. Each efficiency term is computed, using the simulation samples, as the ratio of the number of $K^0_S \to \pi^+\pi^- e^+ e^-$ signal candidates after the selection step and the number in the previous selection step, e.g. $\epsilon_{sel} = N^{MC}_{sel}/N^{MC}_{mass}$. The different selection efficiencies are presented in Table 4.7

Since the simulation samples are used as proxy to mimic the behaviour of real $K^0_S \to \pi^+\pi^- e^+ e^-$ signal candidates, a good agreement between data and the simulation samples distributions is essential in order to extract the correct efficiencies at each selection step. However, it is known that the simulation samples are unable to precisely reproduce various PID distributions and low level trigger decisions. For this purpose, corrections are applied to both the trigger efficiencies and also the selection efficiency, since it imposes cuts in PID distributions of the electrons and pions.

The selection efficiency can be further split into two separate efficiencies, as shown in Eq. 4.5. The first one includes the kinematic and geometric cuts and is expected to be well reproduced at first order in the simulations samples. The second one imposes cuts to PID distributions, namely the ProbNNX variables, shown in Table 4.4.

$$\epsilon_{sel} = \epsilon_{kin,geo} \cdot \epsilon_{PID} \tag{4.5}$$

Particle	Simulation (ϵ)	PIDCalib (ϵ)
e^+	0.77 ± 0.11	0.73 ± 0.01
e^-	0.76 ± 0.11	0.75 ± 0.01
π^+	0.94 ± 0.14	0.90 ± 0.01
π^-	0.97 ± 0.13	0.90 ± 0.01

Table 4.8: Efficiencies of the ProbNN requirement to the four final state particles of the $K^0_S \to \pi^+\pi^- e^+ e^-$ decay. The efficiencies are computed using two methods, the first one uses directly the yields from the simulation samples while the second uses the PIDCalib package.

Corrections are applied to ϵ_{PID} using the PIDCalib package [73]. The tool uses calibration samples, from various particle species, in order to compute the efficiency of a PID selection requirement in different kinematic bins. The decay modes used in the calibrations samples are chosen for their high yield and purity. For the purposes of this study, the electron and pion phase-space are parameterized in bins of transverse momentum (p_T) and pseudorapidity (η). The corrected PID efficiency, averaged out for all events, is extracted using this data-driven technique. The corrected efficiencies are presented in Table 4.8 and are compared to the efficiency values extracted directly from simulation. The PID corrections lower the overall efficiency but are compatible to the direct efficiencies from simulation, given the statistical uncertainty.

The L0 and HLT1 TIS trigger requirement, discussed previously in Sec. 4.2, can be assumed to be K^0_S decay independent. Consequently, the $K^0_S \to \pi^+\pi^-$ channel is used as a control mode to extract the trigger efficiency using a data-driven approach, the TISTOS method. The TISTOS method, discussed in detail in Ref. [74], computes the efficiency of a TIS selection within a TOS sub-sample. These are assumed to be fully uncorrelated with each other. This technique provides a good data-driven proxy to compute the trigger efficiency.

The $K^0_S \to \pi^+\pi^-$ mode has a very large branching fraction, thus having a huge yield in the data samples. Candidates of this control mode are selected by only imposing a single requirement in the form of a stripping line, `StrippingKs2PiPiForRnS`. Due to the huge amount of $K^0_S \to \pi^+\pi^-$ candidates the stripping selection has very strict requirements. It requires two tracks forming a vertex with large transverse momentum, separated from the PV (large IP) and with small DOCA. The reconstructed K^0_S is required to have a mass between $400 - 600\,\text{MeV}/c^2$, and originating from the PV. The number of $K^0_S \to \pi^+\pi^-$ candidates after the stripping selection is imposed is still too large to be saved by the LHCb experiment, given the limited computing resources. Therefore, before the stripping selection, a prescale factor of a 1000, only accepting 1 of each 1000 events, is applied. The invariant mass distribution of data $K^0_S \to \pi^+\pi^-$ candidates for the 2016 data-taking period after this selection can be seen in Fig. 4.4. A clean peak around the K^0_S invariant mass can be observed, as the tight stripping selection is able to remove most of the background candidates.

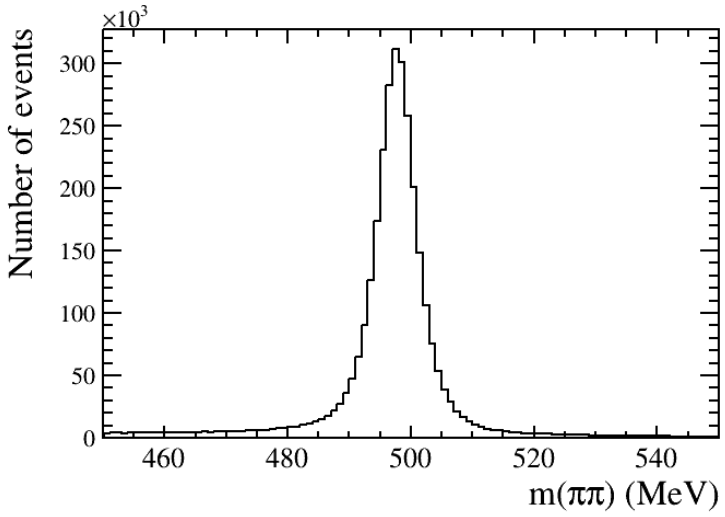

Figure 4.4: Invariant mass distribution of K^0_S candidates from the control mode $K^0_S \to \pi^+\pi^-$, after the stripping requirement is imposed, for the 2016 data-taking period.

Trigger	Simulation (ϵ)	TISTOS (ϵ)
L0 TIS	0.128 ± 0.003	0.206 ± 0.003
L0 TIS & HLT1 TIS	0.019 ± 0.001	0.027 ± 0.001

Table 4.9: Efficiencies of the trigger requriment imposed in the $K^0_S \to \pi^+\pi^-e^+e^-$ study. The efficiencies are computed using two methods, the first one uses directly the yields from the simulation samples while the second uses the TISTOS method with $K^0_S \to \pi^+\pi^-$ candidates.

The trigger efficiencies using the TISTOS method are computed, in a smaller window of 10 MeV around the K^0_S invariant mass, as the ratio:

$$\epsilon^{trig} = \frac{N^{trig}_{TISTOS}}{N^{trig}_{TOS}} \tag{4.6}$$

where N^{trig}_{TOS} are the number of events passing the TOS requirement of a trigger selection and N^{trig}_{TISTOS} are the number of events passing both TOS and TIS requirements. In Table 4.9 the TISTOS method efficiencies are displayed along the efficiencies extracted directly from the simulation samples. The TISTOS efficiency of L0 TIS and HLT1 TIS has an overall larger efficiency. The HLT2 efficiency cannot be computed by this method, as the TOS requirement on the trigger line, `Hlt2DiElectronElSoft`, is explicitly not decay independent. The HLT2 efficiency is extracted from the simulation samples. No major disagreements are expected between data and simulation at this step, as the requirements imposed by the trigger line are mostly kinematic and geometric.

Expected yield

The expected yield $K^0_S \to \pi^+\pi^- e^+ e^-$ during 2016 and 2017 can be estimated using Eq. 4.3. Given that $N(K^0_S/\text{fb}^{-1}) \sim 10^{13}$ is an approximate measurement of the number of K^0_S mesons inside the LHCb acceptance during Run 1, the expected yield is also an approximation. First order corrections to the efficiencies due to the known simulation and data disagreements are applied while other corrections are expected to be negligible given the overall accuracy of the result.

The expected yield using corrected simulation samples is:

$$N^{exp}_{K^0_S \to \pi^+\pi^- e^+ e^-} \sim 1000 \pm 225 \tag{4.7}$$

which is found not to be compatible with the experimental yield obtained previously. Even though the precision of the result is not at the highest level, it is unable to explain the discrepancy on the yields. Further considerations are explained thereafter.

4.4.1 Conclusions

This study was the first milestone towards the usage of the $K^0_S \to \pi^+\pi^- e^+ e^-$ decay mode as a relevant mode to both, study rarer strange decays and to further deepen the knowledge on low energetic electrons at the LHCb experiment. In this study, the $K^0_S \to \pi^+\pi^- e^+ e^-$ mode has been observed for the first time by the LHCb detector using 2016 and 2017 data. However, the observed yield does not to match the expected yield, extracted using the branching ratio of $K^0_S \to \pi^+\pi^- e^+ e^-$ decays, the luminosity of the different data-taking periods, the number of K^0_S mesons created inside the LHCb acceptance and the efficiencies extracted from the simulation samples.

Several considerations have to be taken into account for future studies; instead of adopting the strategy of using the number of K^0_S mesons inside the LHCb acceptance, $N(K^0_S/\text{fb}^{-1})$, the expected yield could be normalized to the yield of the $K^0_S \to \pi^+\pi^-$ mode. A strategy using this approach is presented in Refs [63, 64], also by the LHCb experiment, where the $K^0_S \to \pi^+\pi^-$ mode is used to normalize another very rare strange mode, $K^0_S \to \mu^+\mu^-$. Nevertheless, other factors must also be taken into account. Even though major corrections were applied to the efficiency computations to extract the expected yield, effects considered as second order may be very relevant in view of the results. Consequently a full study of each selection step efficiency may be beneficial to understand the differences.

The lack of simulated samples for the 2017 data-taking period of $K^0_S \to \pi^+\pi^- e^+ e^-$ decays along the small statistics the current 2016 samples present, during the period this study was produced, halted further studies. The inclusion of data and simulation samples for 2018 data-taking would also be highly useful to understand the discrepancies presented in this Chapter.

5 Measurement of the photon polarization in $\Lambda_b^0 \to \Lambda\gamma$ decays

5.1 Introduction

This Chapter presents the main topic of this thesis, the study of the $\Lambda_b^0 \to \Lambda\gamma$ radiative decay, which corresponds to a FCNC mediated by a $b \to s\gamma$ transition. The measurement of the photon polarization in these kind of transitions, as presented in Sec. 3.3, is known to be very sensitive to NP effects. For mesonic b-decays, the helicity structure is complex to analyse since the information on the chirality of the quark is lost during the hadronization process. However, both $b-$factories; BaBar [50] and Belle [75] and the LHCb experiment [51, 52, 54] have performed measurements of the photon polarization, albeit indirectly, for both B^0 and B_s^0 mesons. The first measurement of polarized photons at LHCb in $b \to s\gamma$ transitions corresponds to the analysis of $B^+ \to K^+\pi^-\pi^+\gamma$ decays [51] using the up-down asymmetry. Analyses of angular observables, sensitive to the photon polarization of the virtual photon, in $B^0 \to K^{*0}e^+e^-$ decays at very low dielectron invariant mass were performed in Refs. [54, 76], and currently provide the strongest constraints for right-handed currents in $b \to s\gamma$ transitions. For B_s^0 decays, the photon polarization has been experimentally studied by analyzing the time dependence of the $B_s^0 \to \phi\gamma$ decay rate [52].

Alternatively, baryonic radiative b-decays are good experimental subjects to directly measure the photon polarization given the non-zero spin of both the initial and final state particles [77]. Only the LHCb experiment has been able to perform an observation of one of these radiative transitions. Thanks to the large production of Λ_b^0 baryons in the $p-p$ collisions at the LHC [78] and the ability to reconstruct photons at such energies. The first observation of the $\Lambda_b^0 \to \Lambda\gamma$ decay using data recorded by LHCb during 2016 is reported in Ref. [45]. Providing with a very solid foundation to measure the photon polarization of $\Lambda_b^0 \to \Lambda\gamma$ decays. Given the favorable nature of these baryonic transitions, and to probe the validity of the SM. Searches for similar decays have been recently performed by the LHCb such as the search for the $\Xi_b^- \to \Xi\gamma$ decay [46].

The $\Lambda_b^0 \to \Lambda\gamma$ decay is explicitly useful to measure the helicity structure of the $b \to s\gamma$ transition via an angular analysis of the final state particles. In particular, the weak decay of the Λ baryon ($\Lambda \to p\pi$) gives full access to its helicity and,

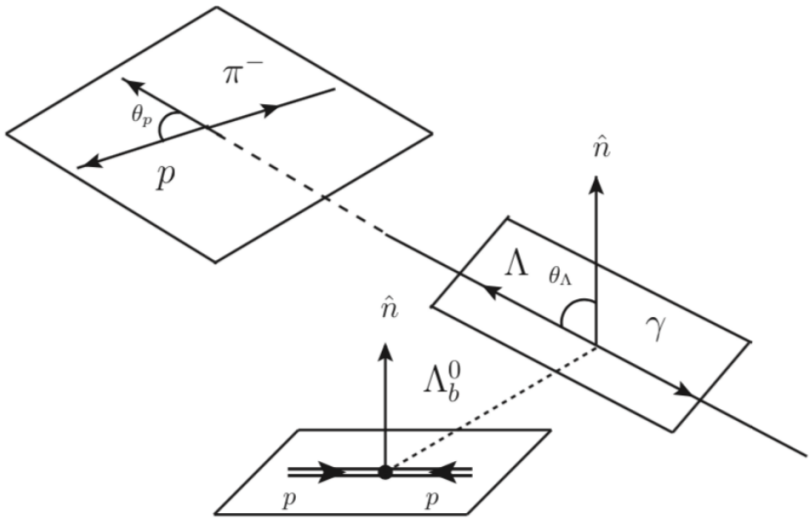

Figure 5.1: Schematic view of the $\Lambda_b^0 \to \Lambda\gamma$ decay, from Ref. [83].

therefore, able to probe the complete $b \to s\gamma$ transition [79].

The angular distribution of $\Lambda_b^0 \to (\Lambda \to p\pi)\,\gamma$ is given by the differential decay width [80]:

$$\frac{\mathrm{d}\Gamma}{\mathrm{d}\,(\cos\theta_p, \cos\theta_\Lambda)} \propto 1 - \alpha_\Lambda P_{\Lambda_b^0} \cos\theta_p \cos\theta_\Lambda - \alpha_\gamma \left(\alpha_\Lambda \cos\theta_p - P_{\Lambda_b^0} \cos\theta_\Lambda\right) \tag{5.1}$$

where $P_{\Lambda_b^0}$ is the initial Λ_b^0 polarization, α_Λ is the Λ weak decay parameter and α_γ is the photon polarization as presented in Eq. 3.8. The angles involved are shown in Fig. 5.1 and specifically are; θ_Λ, the angle between the Λ direction and the Λ_b^0 spin direction in the Λ_b^0 rest frame, and θ_p, the angle between the proton direction in the Λ rest frame and the Λ direction in the Λ_b^0 rest frame. Eq. 5.1 can be further expressed, by integrating over each individual angle, as:

$$\frac{\mathrm{d}\Gamma}{\mathrm{d}\,(\cos\theta_\Lambda)} \propto 1 - \alpha_\gamma P_{\Lambda_b^0} \cos\theta_\Lambda \tag{5.2}$$

$$\frac{\mathrm{d}\Gamma}{\mathrm{d}\,(\cos\theta_p)} \propto 1 - \alpha_\gamma \alpha_\Lambda \cos\theta_p \tag{5.3}$$

independent of each other and sensitive to the photon polarization. Unfortunately, in the LHC the Λ_b^0 polarization, $P_{\Lambda_b^0}$, has been measured to be very small. The CMS and LHCb experiments have performed measurements that are consistent with zero for this production polarization [81, 82]. Therefore the sensitivity to the photon polarization using Eq. 5.2 is suppressed by this factor. It is worth pointing out that this angular description of $\Lambda_b^0 \to \Lambda\gamma$ decays would serve as a theoretically clean method to extract $P_{\Lambda_b^0}$, if no non-SM contribution is assumed and statistics suffice.

On the other hand, Eq. 5.3 provides access to the photon polarization by measuring the angular distribution of $\Lambda_b^0 \to \Lambda\gamma$ candidates in $\cos\theta_p$ up to α_Λ, which

is precisely determined, $\alpha_\Lambda = 0.754 \pm 0.004$ as the average of the measured values by BESIII in Λ and $\overline{\Lambda}$ decays [84]. Throughout this document, if not stated otherwise, the inclusion of the charge-conjugate process to $\Lambda_b^0 \to \Lambda\gamma$, i.e. $\overline{\Lambda}_b^0 \to \overline{\Lambda}\gamma$, is implied.

The result of this Chapter's study has been published in Ref. [1] and presented in a confidential LHCb internal note [2].

5.1.1 Strategy

The angular analysis of the final state particles of $\Lambda_b^0 \to \Lambda\gamma$ decays provides access to the photon polarization of such transitions by studying θ_p, referred throughout as: the proton helicity angle. The special topology of this decay, described in Sec. 5.3, requires the usage of specific online and offline reconstruction and selection tools. Unfortunately, the essential online reconstruction and selection to properly identify such decays, was not present for Run 1, therefore the analysis is only making use of Run 2 LHCb data. Further details on the samples used throughout the study, both simulated and real data, are presented in Sec. 5.2

The selection of $\Lambda_b^0 \to \Lambda\gamma$ candidates used for this analysis is an extended and improved version from the one developed for the first observation of this decay mode in Ref. [45] and uses simulated samples throughout. Dedicated HLT2 and stripping lines are used, followed by a linear cut based selection, referred to as preselection, and a multivariate classifier (MVA), which is fundamental to reduce the large combinatorial background. A data driven approach, utilizing $\Lambda_b^0 \to pK^-J/\psi$ decays, is used to correct for possible differences between data and simulation samples. The selection steps are described in detail in Sec. 5.3.

Two selection configurations, depending on the output of the MVA classifier are considered. The first one retains a larger amount of signal candidates but leads to a reduced signal over background ratio, while the second achieves a lower signal yield but with a larger signal purity. The first option is expected to yield a better statistical significance. The second, being much cleaner, is expected to have smaller systematic uncertainty arising from background contributions and its finally used as a cross-check. An unbinned maximum likelihood fit to the invariant mass of the reconstructed Λ_b^0 candidates, detailed in Sec. 5.4, is performed to determine the number of signal and background candidates present in data after each corresponding selection.

The distribution of the proton helicity angle, from this moment forth also referred as the angular distribution, is used to directly measure the value of the photon polarization. Potential effects arising from both the detection and the selection procedure and the limited precision of the detector are carefully studied using the simulation samples. These effects, namely acceptance and resolution, are presented in Sec. 5.5. On one hand the effect of the resolution is found to be negligible, however, the effect of the acceptance cannot be neglected and thus is thoughtfully validated, by using $\Lambda_b^0 \to \Lambda J/\psi$ as a control channel.

The shape of the angular distribution for signal candidates, studied from simu-

lation and multiplied by the acceptance, is used to fit the proton helicity distribution to extract the photon polarization. The description of this angular fit is detailed in Sec. 5.6. Two different approaches to measure the photon polarization, with different strategies to separate the signal candidates from the remaining background candidates after the full selection, are considered. Both make use of a fit to the reconstructed Λ_b^0 invariant mass candidates. The first approach extends the angular fit to take into account the angular distribution of the background and the fraction of signal and background candidates. Therefore fitting both signal and background contributions to the proton helicity distribution. The second approach uses the sPlot technique [85] which provides weights to each candidate given the probability of being part of the signal or background distributions, using the Λ_b^0 invariant mass. This approach, however, is found to be less efficient with respect to the first approach given the statistically low amount of signal candidates present in the data samples, giving a lower statistical sensitivity to the photon polarization measurement, is fully detailed in App. A.6. The angular fit was blinded to avoid any analyst biases until every part of the analysis was completed. The stability of the fit and sensitivity studies are validated using simulated pseudo-experiments.

The $\Lambda_b^0 \to \Lambda\gamma$ selected candidates can be separated in $\Lambda_b^0 \to \Lambda\gamma$ and $\overline{\Lambda}_b^0 \to \overline{\Lambda}\gamma$ decays by measuring the charge of the proton-pion pair (self-tagged decays). Hence, the first study of $b-$ and $\bar{b}-$decays using this observable is also performed using the same angular strategy.

Lastly, statistical and systematical uncertainties, arising from the choices of the analysis strategy, are evaluated in Sec. 5.7. Results are presented in Sec. 5.8.

5.2 Data samples

The data samples used throughout this Chapter are presented in this section. The data collected by the LHCb experiment during Run 2 of the LHC is used. This corresponds to 2015, 2016, 2017 and 2018 years of data-taking at a center of mass energy of $\sqrt{s} = 13\,\text{TeV}$, for a total integrated luminosity of $\mathcal{L} = 5.8\,\text{fb}^{-1}$. Each year of data-taking has approximately half the samples with one magnet configuration and the other half with the opposite magnet polarity to take into account possible production asymmetries between positive and negative charged particles.

The selection procedure, presented later in this Chapter, groups the data into three categories depending on the data-taking configuration for each year: 2015 and 2016 data-taking years are treated together while 2017 and 2018 are treated individually. The two existing magnet configurations are treated together in all categories, given the small differences that these entail for this particular analysis.

Simulated samples, also referred to as Monte Carlo (MC) samples, are used. Reproducing the different data-taking conditions to develop the selection, model the invariant mass distribution and describe the acceptance. The simulation uses a complex chain of computing tools to reproduce the whole process, starting from the $p-p$ collisions inside the LHCb experiment, the detector response to the particles

produced up to the digitization, reconstruction and trigger process, in the same way the experimental data is treated [86–91].

Signal MC samples are generated for each data-taking year, along with various other decay modes of interest for this Chapter. A summary of all the simulated samples is shown in Table 5.1. The simulation chain is grouped in software versions, referred to as `Sim` versions. The event type number refers to the configuration used at generator-level for each decay channel, including possible selection cuts at that level. Most relevantly, a cut is applied on the photon at generator level requiring to have high transverse momentum for 2017 and 2018 signal samples ($p_T > 1.5$ GeV/c). The `ReDecay` techinque [92], which re-uses part of the simulation process to generate several events, is also used to reduce the computing time and save disk space, as typically simulated samples use a large amount of computing resources. A description of the technique is described in Appendix A.1, along a validation of its use for the signal mode. As a direct consequence of the usage of the photon cut at generation level and the ReDecay technique, the number of generated events for the 2017 and 2018 data-taking periods is substantially lower than the events generated with 2016 conditions. To further reduce the computing resources used to generate and keep the samples, the 2016, 2017 and 2018 samples are required to pass the stripping selection (see Sec. 5.3).

Decay channel	Event type	Year	Sim version	Events
$\Lambda_b^0 \to \Lambda\gamma$	15102307	2016	Sim09b	37000779
	15102320	2017	Sim09h-ReDecay01	837578
	15102320	2018	Sim09h-ReDecay01	838830
$\Lambda_b^0 \to \Lambda J/\psi$	15144103	2016	Sim09h	3005560
	15144103	2017	Sim09h	3044782
	15144103	2018	Sim09h	3081860
$\Lambda_b^0 \to pK^- J/\psi$	15144001	2016	Sim09c	1046532
	15144001	2017	Sim09h	4011113
	15144001	2018	Sim09f	10020715
$\Lambda_b^0 \to \Lambda\eta$	15102512	2016	Sim09c-ReDecay01	8968920

Table 5.1: Simulation samples used in the analysis, event type, year, simulation version, number of simulated events used to build the samples.

No dedicated MC samples in 2015 data-taking conditions are used. Instead, 2016 simulation is used for the study of both 2015 and 2016 data due to the known similarities in the conditions of both years and the small integrated luminosity that 2015 presents.

In the simulation of signal samples, the photon polarization is generated to be fully left-handed, as predicted in the SM. The generator-level proton helicity angle is checked to follow the expected distribution, described in Eq. 5.3, and it is shown in Fig. 5.2.

The usage of simulated samples to cope with the lack of real data proxies to characterize the different decay channels is known to be very good but not perfect.

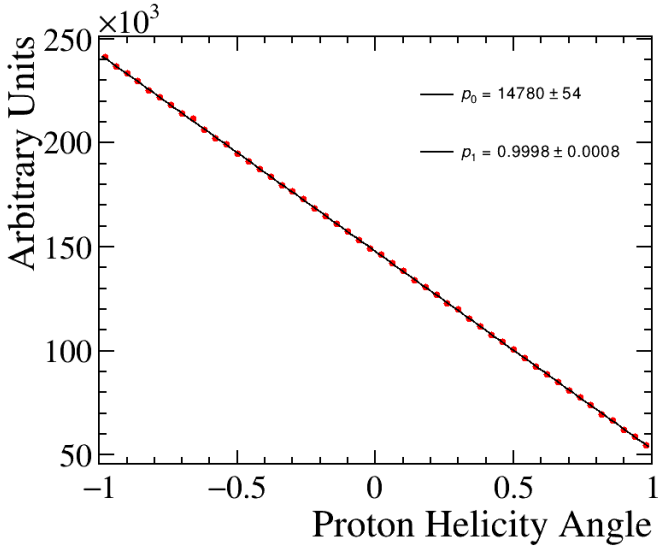

Figure 5.2: Generator-level distribution of $\cos\theta_p$ for signal events with a fit to the photon polarization. Error bars are plotted. The fitted function is $W(\theta_p) = p_0 \cdot (1 - \alpha_\Lambda \cdot p_1 \cdot \cos\theta_p)$, comparing it to Eq. 5.3, p_1 corresponds to the fitted photon polarization.

There are different aspects in which the simulated samples are not able to properly describe the data. In particular, it is known that the kinematic properties of the Λ_b^0 are not well reproduced in simulation, which is further aggravated by the use of the `ReDecay` technique. This difference and the procedure used to address it is detailed in the next section. Other properties, such as PID distributions, are also affected by it. Typically having relevant effects when efficiencies play a role in the process, since this is not the case for this study, these effects are expected to be very low. Nevertheless, no correlations are found between the different PID variables used in the reconstruction and selection and the proton helicity distribution, thus any possible discrepancies can be fully neglected.

5.3 Reconstruction and selection

The selection and reconstruction of $\Lambda_b^0 \to \Lambda\gamma$ candidates at the LHCb experiment is quite challenging given its topological characteristics. Both, the photon and the Λ baryon, are neutral particles which leave no tracks on the detectors and the Λ is considered a long lived particle in the LHCb environment. This last characteristic along with the impossibility to measure the direction of the photon within the LHCb experiment makes it impossible to obtain information of the b-baryon decay vertex (known as secondary vertex, SV) and requires the need of a particular strategy to reconstruct $\Lambda_b^0 \to \Lambda\gamma$ decay candidates.

The first observation of the $\Lambda_b^0 \to \Lambda\gamma$ radiative decay, archived by the LHCb experiment using 2016 data, is described in Ref. [45] and provides a successful strategy to overcome the previously mentioned obstacles. Therefore, the same strategy,

with small adaptations, is detailed in this section, and is used to reconstruct and select the $\Lambda_b^0 \to \Lambda\gamma$ candidates for the full Run 2 data. Additionally, the selection and reconstruction of the $\Lambda_b^0 \to pK^-J/\psi$ and $\Lambda_b^0 \to \Lambda J/\psi$ decay candidates is also detailed. In a general manner, comparisons between simulated signal candidates and data candidates, outside the expected Λ_b^0 invariant mass signal region, for different distributions are used to define the selection strategy.

5.3.1 Selection and reconstruction of signal candidates

The lack of a secondary vertex complicates the reconstruction of the Λ_b^0 baryon momentum, but it does not impede it. Firstly, Λ baryon candidates are reconstructed from the combination of two good-quality highly energetic tracks forming a good vertex but incompatible with originating from any primary vertex (PV), as well as compatible with the proton (p) and a pion (π) hypotheses. Most of the Λ baryons decay outside the VELO given the relatively large lifetime that they present in the LHCb experiment framework. Unfortunately, the lack of information from the VELO sub-detector makes it more difficult to reconstruct them and worsens the resolution of such decays. Consequently, only Λ candidates that happen to decay inside the VELO are considered (long tracks) in this Chapter. As already pointed out, these are a minority, the inclusion of Λ decays outside the VELO (downstream tracks) would naively increase the statistics a factor five. Secondly, a photon (γ), reconstructed as a calorimeter cluster, is combined with the Λ candidate. No tracks can be associated with the photon candidate, therefore it is assumed to originate at the interaction point (i.e. the PV). The Λ_b^0 candidate is computed by the direct sum of the Λ and γ momenta, and its trajectory is determined by its momentum and the PV position.

A detailed description of relevant variables that are used in the different selection steps are presented as follows:

$\mathbf{p_T}$ Transverse momentum; momentum of the particle in the perpendicular plane to the LHC beam direction.

$\boldsymbol{\eta}$ Pseudorapidity; Angle of a particle with respect to the beam axis defined as: $\eta = -\ln\left[\tan\left(\theta/2\right)\right]$

IP Impact Parameter; the minimum distance of a track with respect to a vertex (or track extrapolation). If not stated otherwise the vertex of interest is the PV, therefore a small IP typically indicates that the track has been produced at the PV (prompt).

DOCA Distance of closest approach; defines a minimum distance, similar to the IP, of two tracks. Small DOCA values indicate a high possibility of tracks coming from the same point, i.e. forming a vertex.

MTDOCA Mother trajectory DOCA; the minimum distance between a particle and its extrapolated mother trajectory.

FD Flight distance; Distance the particle travels before decaying. Computed as the difference between the production initial-vertex and the decay final-vertex

position.

DIRA Cosine of the angle between the momentum of the track and the direction of flight from the PV.

Track and vertex χ^2 Quality of the track or vertex reconstruction. Typically, considered along the number of degrees of freedom (ndof).

IP/MTDOCA/FD χ^2 Significance of the measured distance (IP/MTDOCA/FD) taking into account the quality of the computation (uncertainty). As an exemplification, a value of χ^2_{IP} larger than 16 indicates that the minimum distance between a track and the vertex is bigger than 4σ.

Particle identificators Includes DLL, ProbNNX, PIDX, IsMuon, CL and IsPhoton. Combine the information provided by the particle identification system of the LHCb experiment to estimate the particle hypothesis. Most noticeably, the Confidence Level (CL) is used to distinguish charged tracks from neutral tracks and the IsPhoton [23] tool is used to distinguish photons from neutral hadrons utilizing the information of SPD, ECAL and HCAL clusters.

Track ghost probability Uses a multivariate analysis (MVA) classifier to provide the likelihood of a track to be a pseudorandom combination of hits from the different tracking stations. Thus requiring smaller values increments the probability of being a real track.

Trigger selection

The online selection, also referred as trigger selection, uses the three triggering steps presented in Sec. 2.2.3 to differentiate $\Lambda_b^0 \to \Lambda\gamma$ candidates from possible background candidates. At L0, the presence of a photon (ECAL cluster) with a high transverse energy (E_T) is exploited by requesting a positive decision from either `L0Photon` or `L0Electron` trigger lines, which allow to use both calorimeter clusters with and without hits in the associated SPD cell. The line triggering can be produced by either a particle used to reconstruct the candidate of interest (signal photon) or a particle arising from the underlying event (arbitrary photon from the rest of the $p-p$ collisions in the same event). These requirements are referred as; Trigger on signal (TOS) and Trigger independent of signal (TIS), respectively. Throughout all the trigger steps presented in this Section, the TOS requirement is imposed. During the different years of data taking and for different trigger configurations (TCK), the required photon transverse energy in the L0 lines has changed. A summary of these changes for the major data and simulations samples can be found in Table 5.2. The effect of the threshold variations is discussed later on.

After L0, the HLT1 selection for b-hadron decays typically exploits the large transverse momentum and large impact parameters of the final state particles (tracks). In particular, a positive decision of the `Hlt1TrackMVA` trigger line is required. This line exploits the previous properties for a final state particle, relevant given the highly asymmetric decay of the Λ baryon, as the proton carries most of the total momentum.

Samples	Year	TCK	L0Photon	L0Electron
Data	2016	5641	118	98
	2016	5647	116	100
	2017	5895	113	96
	2017	5896	96	88
	2017	5897	103	88
	2018	All	123	99
Simulated	2016	5647	116	100
	2017	5897	103	88
	2018	6308	123	99

Table 5.2: Values of the energy thresholds for L0Photon and L0Electron lines depending on year and TCK. The values are given in ADC, for Run 2 one ADC corresponds to 24 MeV.

As a last step for the online selection of $\Lambda_b^0 \to \Lambda\gamma$ candidates, a dedicated selection named Hlt2RadiativeLb2L0GammaLL is used. The candidate is reconstructed online following the strategy presented at the beginning of this Section with specific requirements, detailed in Table 5.3. The selection requirements for this line are stable between the different years and TCK configurations.

Offline selection

The offline reconstruction and selection is aligned with what has been presented in the online part. Three different steps are used to do so, firstly the stripping selection and then a preselection, which paves the way to finally use a multivariate classifier (MVA).

The stripping selection used is named StrippingLb2L0Gamma, which reconstructs the candidates offline and further filters them similarly to the HLT2 trigger selection, it is detailed in Table 5.4. In general, the stripping selection is aligned with the online selection. Specifically, tighter requirements on the track quality, the momenta and transverse momenta of reconstructed pions and protons are imposed, particularly interesting is the π p_T cut that has a relevant effect presented in Sec. 5.5. For the photon, a tighter transverse momenta is also imposed along a particle identification requirement.

A normalized distribution of the reconstructed invariant mass of Λ baryon candidates in the data samples after the stripping requirement is shown in Fig. 5.3. A narrow peak around the world average Λ mass, with an experimental resolution coherent with what is expected from the LHCb experiment can be observed, along two long tails coming from background contribution covering a broader spectrum of invariant mass values. The figure shows a small amount of background candidates with respect to real Λ candidates present, therefore indicating a good performance from the previous selection steps. Moreover, this points out that remaining $\Lambda_b^0 \to \Lambda\gamma$ background candidates, after the full selection, arise from combinations with real Λ candidates.

Variable	Units	Requirement
Track p	MeV/c	> 2000
Track p_{T}	MeV/c	> 250
Track χ^2_{IP}		> 36
Track χ^2		< 3
p DLLp		> 0
Tracks DOCA	mm	< 0.2
γ p	MeV/c	> 5000
γ p_{T}	MeV/c	> 2000
Λ p_{T}	MeV/c	> 1500
Λ IP	mm	> 0.1
Λ χ^2_{Vtx}/ndof		< 15
Λ χ^2_{FD}		> 0
Λ τ	ps	> 2
Λ ΔM	MeV/c^2	< 20
γ p_{T} + Λ p_{T}	MeV/c	> 5000
Λ_b^0 χ^2_{MTDOCA}		< 9
Λ_b^0 p_{T}	MeV/c	> 1000
Λ_b^0 ΔM	MeV/c^2	< 1000

Table 5.3: Requirements included in the `Hlt2RadiativeLb2L0GammaLL` trigger line.

Variable	`Lb2L0Gamma`	Units
Track χ^2_{IP}	> 16	
max(p, π) Track χ^2/ndof	< 3	
min(p, π) Track χ^2/ndof	< 2	
Track Ghost Prob.	< 0.4	
π p_T	> 300	MeV/c
π p	> 2000	MeV/c
p p_T	> 800	MeV/c
p p	> 7000	MeV/c
p DLLp	$>$ -5	
Tracks χ^2_{DOCA}	< 30	
Λ p_T	> 1000	MeV/c
Λ ΔM	< 20	MeV/c^2
Λ IP	> 0.05	mm
Λ χ^2_{Vtx}/ndof	< 9	
γ p_T + Λ p_T	> 5000	MeV/c
Λ_b^0 p_T	> 1000	MeV/c
Λ_b^0 ΔM	< 1100	MeV/c^2
Λ_b^0 χ^2_{MTDOCA}	< 7	
γ CL	> 0.2	
γ p_T	> 2500	MeV/c

Table 5.4: Stripping selection for the $\Lambda_b^0 \to \Lambda\gamma$ decay channel.

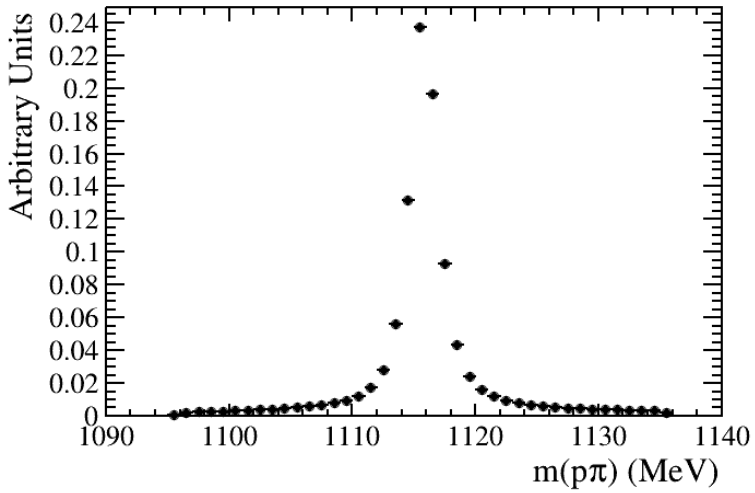

Figure 5.3: Normalized invariant mass distribution of the proton-pion pair, forming Λ candidates, of the 2018 data samples after the stripping requirement has been applied. In natural units.

The preselection is designed to reduce the number of total candidates while keeping as many signal candidates as possible. To do so, and analogously to previous selection steps, the election of the different variables and cuts is done by comparing the simulated sample signal distributions with real data distributions outside the invariant mass region of the expected Λ_b^0 candidates, i.e. background candidates. In this case, data candidates below 5100 MeV or above 6300 MeV are considered for this purpose. The preselection also includes tighter rectangular cuts in other quantities previously used in the stripping and HLT2 selections. On top of that, π candidates coming from the Λ decay are required to be first detected in the initial region of the VELO, where the density of VELO modules is higher, since it was found to significantly reduce background candidates. Loose PID requirements on both the proton and the pion are also demanded along a smaller mass window for Λ candidates, further removing possible combinatorial background. Another remarkable aspect is the requirement of the photon transverse momentum ($\gamma\ p_T$) to be larger than 3 GeV, superseding and aligning the different requirements made by the L0 trigger selection for the different years and samples. Possible concerns, arising from the different computation procedure of the photon transverse momentum by the L0 with respect to the offline systems, are considered to be negligible after this last requirement. The summary of the different requirements for the preselection stage are found in Table. 5.5. The preselection has an average background rejection of 98% and a 50% signal efficiency for the different years of data-taking.

5.3.2 Control channels reconstruction and selection

Two decay modes, $\Lambda_b^0 \to \Lambda J/\psi$ and $\Lambda_b^0 \to pK^- J/\psi$, are used to control different aspects of the analysis presented in this Chapter given their similarities. The exploited decay chains for the control modes are are $\Lambda_b^0 \to (\Lambda \to p\pi)\,(J/\psi \to \mu\mu)$ and $\Lambda_b^0 \to pK^-\,(J/\psi \to \mu\mu)$. The selection and reconstruction of the control candidates

Variable	Units	Requirement
Track Ghost Prob.		< 0.2
Track p	GeV/c	$\in (3, 100)$
$\pi^\pm$ first hit Z	mm	< 270
p ProbNNp		> 0.2
π ProbNNpi		> 0.2
γ p_{T}	MeV/c	> 3000
Λ IP	mm	> 0.15
Λ χ^2_{IP}		> 16
Λ χ^2_{FD}		> 225
Λ M	MeV/c^2	$\in (1110, 1122)$
Λ_b^0 MTDOCA	mm	< 0.05
Λ_b^0 χ^2_{MTDOCA}		< 5
Λ_b^0 p_{T}	MeV/c	> 4000
Λ_b^0 ΔM	MeV/c^2	< 1000

Table 5.5: Preselection requirements applied on $\Lambda_b^0 \to \Lambda\gamma$ candidates.

is chosen to be the same for the different data-taking years. Control modes are commonly chosen for their experimental cleanliness, either by having a high decay rate (yield) or because they are experimentally easy to select given their decay properties or topology. In this case, the precise muon detection systems that the LHCb experiment possess are exploited, via the J/ψ decay into a muon pair. These two control modes have been explored by the LHCb experiment in various other analyses using different approaches [82, 93]. The $\Lambda_b^0 \to pK^- J/\psi$ is used to control and correct the agreement between data and simulated samples of the Λ_b^0 baryon properties. The $\Lambda_b^0 \to \Lambda J/\psi$ mode is also used to cross-check the corrections, and most relevantly to control the acceptance of the signal channel, which in both cases is dominated by the hadronic part of the decay, this is further detailed in Sec. 5.5.

The $\Lambda_b^0 \to \Lambda J/\psi$ decay has a similar topology to the signal mode, formed by a Λ and with the photon being replaced by a J/ψ which is reconstructed using its dimuon final state. The Λ_b^0 reconstruction for this mode is done to be as similar as possible to the signal mode, therefore the SV, whose reconstruction is possible for this decay mode, is not reconstructed. Therefore a dedicated stripping line, `Lb2L0Gamma_Lb2L0Jpsi`, is used, and is detailed in Table 5.6. The only differences with regards to the signal mode arise from the selection of J/ψ mesons instead of photon candidates, while the Λ selection and the combination is identical. The trigger selection is however different for the control mode, due to the presence of a J/ψ instead of a photon in the final state. Several trigger lines focusing on the presence muons, and dimuon pairs, are used for this purpose. In particular, candidates are required to have a positive decision from `L0Muon` or `L0DiMuon` at the L0 level, `Hlt1DiMuonHighMass` or `Hlt1TrackMuon` in HLT1 and `Hlt2DiMuonDetachedJPsi` in HLT2. These trigger lines mainly have requirements on the momenta, transverse momenta, dimuon mass and impact parameters of the muons. The last step of the selection strategy for this mode is the offline selection which is found in Table. 5.7

Given the purity and high yield of this mode, no further selection is required. A preliminary fit to the Λ_b^0 invariant mass for this mode is displayed in Fig. 5.4. Presenting a narrow peak around the world average Λ_b^0 mass, corresponding to signal $\Lambda_b^0 \to \Lambda J/\psi$ candidates, and an exponential distribution for the combinatorial background, which populate a broader invariant mass spectrum.

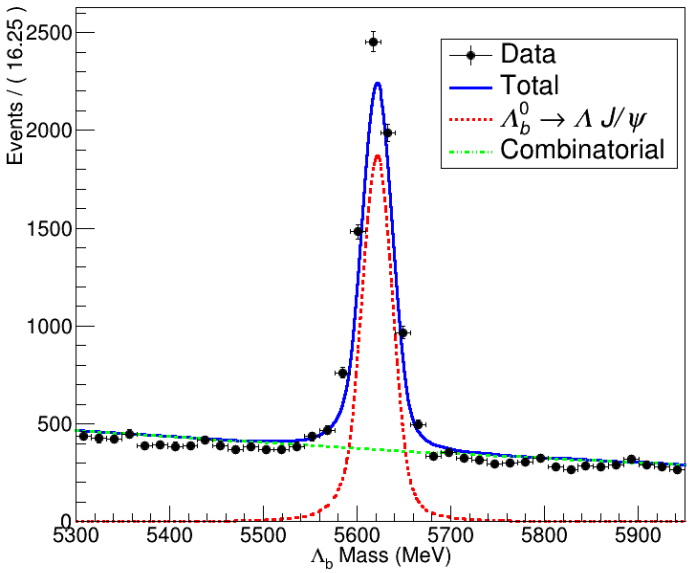

Figure 5.4: Preliminary fit to the invariant mass distribution of the $\Lambda_b^0 \to \Lambda J/\psi$ candidates using 2016, 2017 and 2018 data samples after the all the selection requirements are imposed.

The $\Lambda_b^0 \to pK^- J/\psi$ channel is used to correct the known discrepancies in the simulated samples for the Λ_b^0 baryon candidates, whose properties are decay independent. Consequently, and contrary to the $\Lambda_b^0 \to \Lambda J/\psi$ decay channel, the selection is not required to closely follow the signal mode strategy, instead maximizing the purity and yield is its only target. To do so, the reconstruction and selection is based on the one used in Ref. [93], with small modifications. In particular, at the trigger level, positive decisions are required from `L0Muon` or `L0DiMuon` at L0 level and `Hlt1TrackMVA` or `Hlt1TrackTwoMVA` in HLT1. For HLT2, one of several lines, focusing on topological and muon lines, are required to have a positive decision; `Hlt2Topo2Body`, `Hlt2TopoMu[2,3,4]Body` `Hlt2DiMuonDetached`. The offline selection is simplified and is detailed in Table 5.8.

5.3.3 Simulation corrections

The different selection steps use, in one way or another, the simulation samples as the basis to distinguish signal from background contributions. This fact is most noticeable in the MVA selection, which explicitly uses simulation as proxy for signal to train the classifier. Therefore a good agreement between data and simulation is extremely relevant to optimize the whole candidate selection.

Variable	`Lb2L0Gamma_Lb2L0Jpsi`	Units
Track χ^2_{IP}	> 16	
max(p, π) Track χ^2/ndof	< 3	
min(p, π) Track χ^2/ndof	< 2	
Track Ghost Prob.	< 0.4	
π p_T	> 300	MeV/c
π p	> 2000	MeV/c
p p_T	> 800	MeV/c
p p	> 7000	MeV/c
p DLLp	> -5	
μ Track χ^2	< 5	
μ `IsMuon`	= True	
Tracks χ^2_{DOCA}	< 30	
Λ p_T	> 1000	MeV/c
Λ ΔM	< 20	MeV/c^2
Λ IP	> 0.05	mm
Λ χ^2_{Vtx}	< 9	
J/ψ p_{T} + Λ p_{T}	> 5000	MeV/c
Λ_b^0 p_T	> 1000	MeV/c
Λ_b^0 ΔM	< 1100	MeV/c^2
Λ_b^0 χ^2_{MTDOCA}	< 7	
J/ψ ΔM	< 100	MeV/c^2
J/ψ χ^2_{DOCA}	< 30	mm
J/ψ χ^2_{Vtx}	< 25	

Table 5.6: Stripping selection for the $\Lambda_b^0 \to \Lambda\gamma$ decay channel. In the first section, Track refers only to the proton and pion from the Λ candidate.

Variable	$\Lambda_b^0 \to \Lambda J/\psi$	Units
Track χ^2/ndof	< 4	
π ProbNNpi	> 0.2	
p ProbNNp	> 0.2	
μ ProbNNmu	> 0.2	
Λ ΔM	< 6	MeV/c^2
Λ IP	> 0.15	mm
Λ χ^2_{IP}	> 16	
Λ χ^2_{FD}	> 225	
J/ψ ΔM	< 60	MeV/c^2
J/ψ χ^2_{Vtx}	< 16	
Λ_b^0 p_T	> 4000	MeV/c

Table 5.7: Selection for the $\Lambda_b^0 \to \Lambda J/\psi$ decay channel for all data-taking years

Variable	$\Lambda_b^0 \to pK^-J/\psi$	Units
p p_T	> 400	MeV/c
p p	> 7500	MeV/c
K p_T	> 400	MeV/c
K p	> 2000	MeV/c
p PIDp	> 0	
p PIDp $-$ p PIDK	> 8	
K PIDK	> 0	
p `IsMuon`	$=$ False	
K `IsMuon`	$=$ False	
J/ψ M	> 3000	MeV/c^2
J/ψ M	< 3200	MeV/c^2
Λ_b^0 $\chi^2_{\rm SV}$	< 4	
Λ_b^0 DIRA	> 0.9999	

Table 5.8: Selection for the $\Lambda_b^0 \to pK^-J/\psi$ decay channel for all data-taking years.

The Λ_b^0 kinematics are known not to be that well reproduced in simulation, in particular the Λ_b^0 production dependency with $p_{\rm T}$ has been observed in e.g. Ref. [78]. The Λ_b^0 properties are controlled via the $\Lambda_b^0 \to pK^-J/\psi$ decay. The properties do not depend on the final decay of the Λ_b^0, therefore this mode is used given its high purity and yield in the data samples.

To start with the simulation corrections, an even cleaner subset of $\Lambda_b^0 \to pK^-J/\psi$ candidates in data after the selection is obtained through the use of the sPlot technique [85], which allows to unravel the signal candidate distribution from the background one by exploiting a control distribution, in this case the Λ_b^0 invariant mass distribution. The signal and combinatorial background invariant mass distributions are described with a double-sided Crystal Ball (Eq. 5.9) and a first order polynomial, correspondingly. The values of the tail parameters of the signal distribution are fixed from a fit to the simulation samples while the mean and the width of the signal distribution and the polynomial parameter are let free in the data fit. This procedure is repeated for each year of data taking individually. A complete explanation of the usage of this scheme to fit invariant mass distributions is found in Sec. 5.4. The results of the fits to data are shown in Fig. 5.5 and the shape parameters are reported in Table 5.9. A good description of the data samples is obtained with this simple model.

A set of per event weights (sWeights) is obtained for $\Lambda_b^0 \to pK^-J/\psi$ candidates for each data-taking year. Comparisons of the simulated signal data samples versus sWeighted data samples are produced. As expected from the known simulation problems, major differences are observed for the Λ_b^0 kinematics. These differences are shown in Figs. 5.6 and 5.7 for the Λ_b^0 p, $p_{\rm T}$ and pseudorapidity (η) distributions. Consequently, the differences between the $\Lambda_b^0 \to pK^-J/\psi$ samples are also expected to be present in the simulated $\Lambda_b^0 \to \Lambda\gamma$ signal candidates.

To solve the problematic differences, corrections are obtained as binned 2-

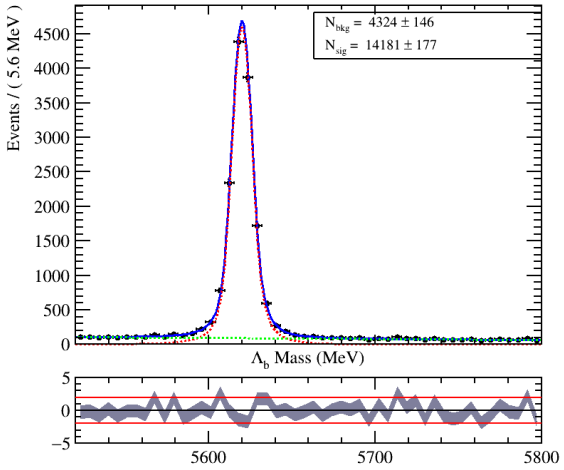

(a)

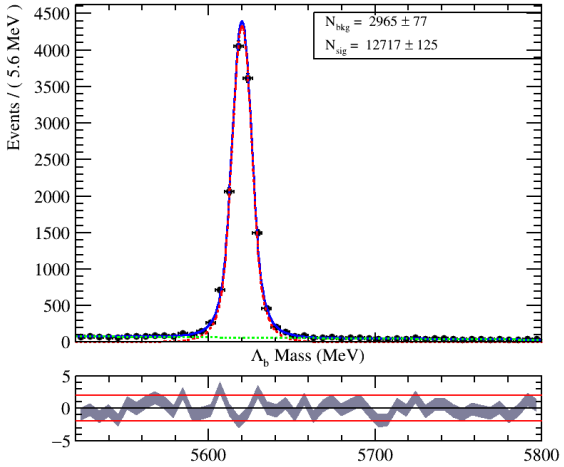

(b)

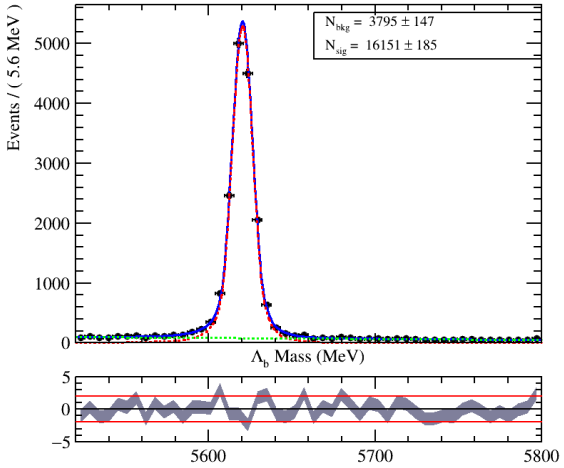

(c)

Figure 5.5: Invariant mass distributions of $\Lambda_b^0 \to pK^-J/\psi$ selected candidates for (a) 2016, (b) 2017 and (c) 2018 years (natural units). The results of a fit with a double-sided Crystal Ball (red) and a first order polynomial (green) are overlaid.

Parameter	2016	2017	2018
α_R^{sig}	-1.59 ± 0.09	-1.48 ± 0.09	-1.67 ± 0.08
α_L^{sig}	1.67 ± 0.09	1.49 ± 0.07	1.66 ± 0.08
n_R^{sig}	3.2 ± 0.7	5.2 ± 1.4	3.3 ± 0.8
n_L^{sig}	2.5 ± 0.6	5.0 ± 3.5	2.3 ± 0.05
μ^{sig}	5619.94 ± 0.07	5619.90 ± 0.08	5620.23 ± 0.07
σ^{sig}	6.32 ± 0.09	6.0 ± 0.1	6.25 ± 0.08
p_0^{bkg}	$(-1.60 \pm 0.03) \cdot 10^{-4}$	$(-1.659 \pm 0.009) \cdot 10^{-4}$	$(-1.64 \pm 0.02) \cdot 10^{-4}$

Table 5.9: Parameters of the $\Lambda_b^0 \to pK^-J/\psi$ invariant mass fit using a double-sided Crystal Ball and a first order polynomial for each data-taking year.

dimensional (2-D) ratios between sWeighted data and simulated $\Lambda_b^0 \to pK^-J/\psi$ candidates. The Λ_b^0 p_{T} and η distributions provide a good coverage of the disagreement, and are used for this purpose. The binned 2-D ratios used as corrections for the simulated samples are shown in Fig. 5.7 (right) for each year individually. Corrections are applied to the simulation samples as per event weights, extracted from the 2-D (Λ_b^0 p_{T}, Λ_b^0 η) bin that corresponds to each event. The reweighted $\Lambda_b^0 \to pK^-J/\psi$ distributions are overlaid in Figs. 5.6 and 5.7, showing a much better agreement with the data samples. Having observed the good behaviour of this method, the corrections are applied to both $\Lambda_b^0 \to \Lambda\gamma$ and $\Lambda_b^0 \to \Lambda J/\psi$ simulation samples and are used in the following steps of this Chapter.

Variables related to the Λ baryon and the final state hadrons are also checked, using $\Lambda_b^0 \to \Lambda J/\psi$ candidates. These are found to be in good agreement between data and simulation once the Λ_b^0 kinematic distributions are corrected and are shown in App. A.2.

5.3.4 Multivariate classifier

After the preselection, a multivariate analysis (MVA) tool is exploited to further discriminate the signal candidates from the combinatorial background, which is dominated by the random combinations of photons with Λ baryons. A Boosted Decision Tree (BDT) [94] using the XGBoost algorithm [95, 96] implemented through the scikit-learn [97] machine learning python package is trained for this purpose. The BDT combines the discriminating power of the different variables into a single continuous one. The final selection depends on which value is chosen for this all-in-one variable, which is typically optimized for the purpose of the study. MVA methods provide an improvement with respect to linear selections, since they exploit correlations between different variables, as present in this analysis. But they do not come for free as they usually require more computing power and computing time.

Three BDT's are trained independently for three sets of Run 2 LHCb data corresponding to 2015 & 2016, 2017 and 2018. The BDT requires of a training procedure, thus needing signal and background samples. Generally, an increment of the statistics used in the process of training the BDT also increases its overall performance. Thus, a single BDT would naively be more suitable than three separate

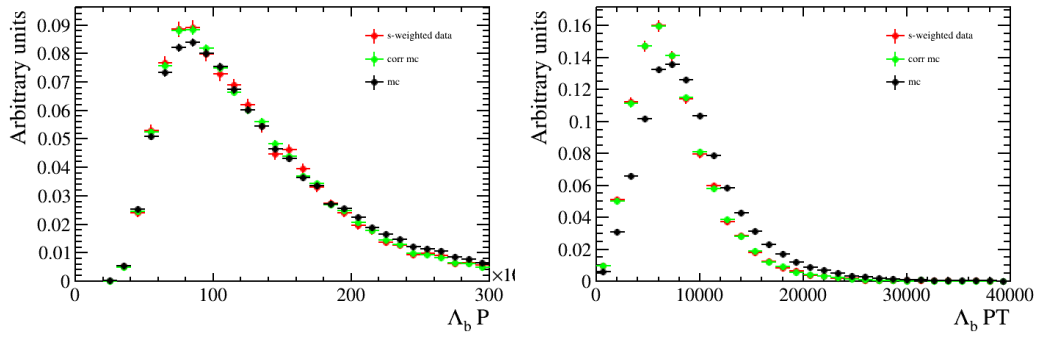

(a)

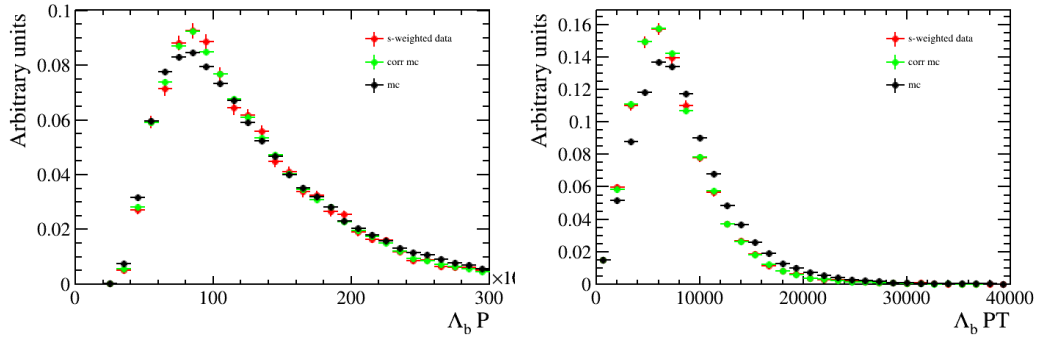

(b)

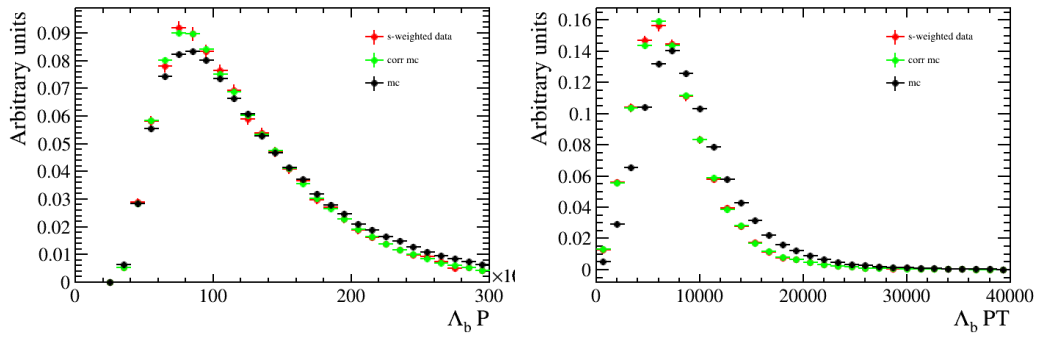

(c)

Figure 5.6: Λ_b^0 momentum (left) and transverse momentum (right) distributions of $\Lambda_b^0 \to pK^-J/\psi$ sWeighted data candidates (red), simulated (black) and corrected simulated candidates (green) for (a) 2016, (b) 2017 and (c) 2018.

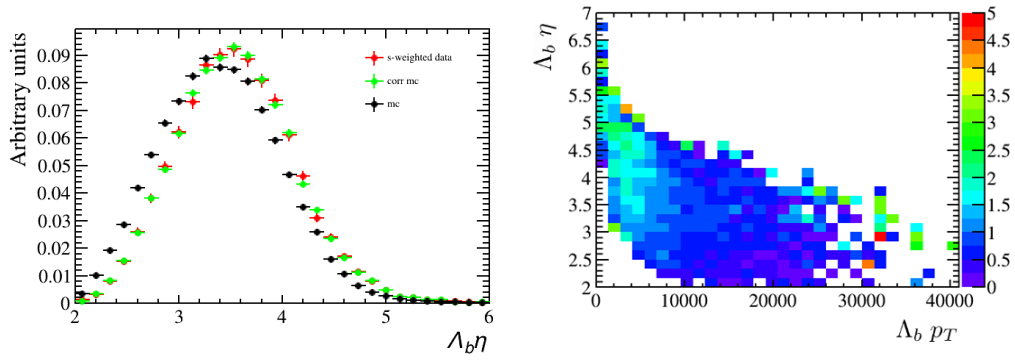

(a)

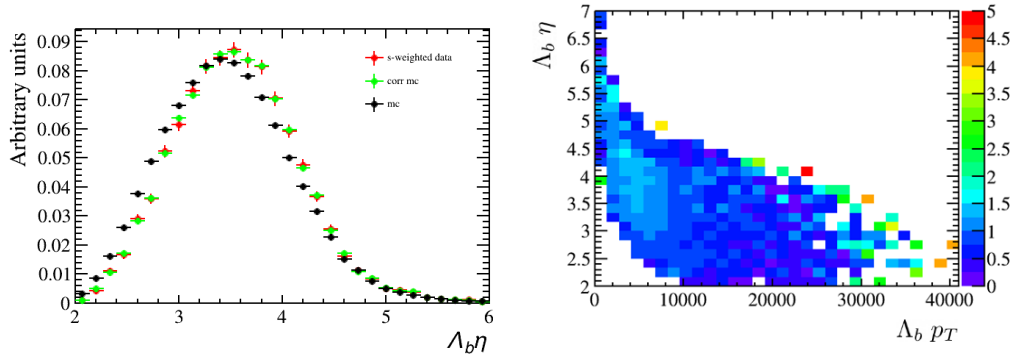

(b)

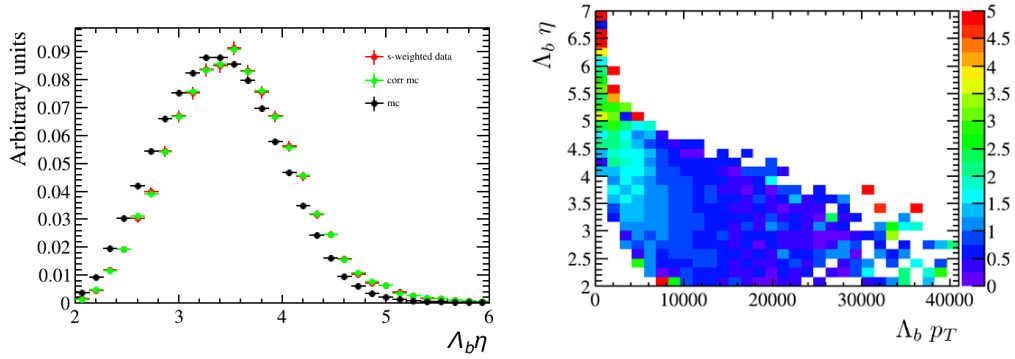

(c)

Figure 5.7: On the left, Λ_b^0 pseudorapidity distributions of $\Lambda_b^0 \to pK^- J/\psi$ sWeighted data candidates (red), simulated (black) and corrected simulated candidates (green). On the right, corrections in 2-D bins of Λ_b p_T and Λ_b η obtained as the ratio of sWeighted data and simulation samples of $\Lambda_b^0 \to pK^- J/\psi$ for (a) 2016 (b) 2017 and (c) 2018.

ones for this study. Nevertheless, when the samples differ from each other, outside of a statistical uncertainty perspective, this may not be the case. A study was performed to choose which option is best suited, studying the performance of the BDT depending on which combination of samples for different data-taking periods are used. The study balances the use of more statistics when training a BDT to increase its performance, with possible differences between data samples, coming from the online LHCb selection, which may cause a loss of performance. Differences between 2015, 2016, 2017 and 2018 arise mostly from different configurations of the HLT1 trigger during data-taking along with the L0 trigger line thresholds. It is worth pointing out that even though the different thresholds are aligned with a tighter cut offline, residual effects may be present due to the L0 transverse energy computation. Using a BDT for each data-taking period provides a slightly better performance than other options, and is the strategy used.

The corrected simulated signal $\Lambda_b^0 \to \Lambda\gamma$ candidates for each set are used as signal proxies and data candidates with a reconstructed Λ_b^0 invariant mass above Λ_b^0 Mass > 6100 MeV/c^2 are used as background proxies, as no real $\Lambda_b^0 \to \Lambda\gamma$ candidates are expected in that mass region. Candidates with masses much lower than the Λ_b^0 invariant mass are not considered given the fact that possible physical backgrounds, in addition to combinatorial background, may be present in that region.

Sixteen input variables are used for the BDT's, listed in Table 5.10 and common to all three. The variables used for the hadronic part of the decay include transverse momenta and impact parameters among other geometric and kinematic variables such as the DOCA of the proton and the pion and the flight distance of the Λ, which are described at the start of this section. For the photon, the transverse momentum is used along with the pseudorapidity, which is an addition to the BDT with respect to Ref. [45]. A complex set of isolation variables, referred to as momentum asymmetries, are also included for both the Λ and the photon candidates. These correspond to $\mathcal{A}_p(\Lambda), \mathcal{A}_{p_T}(\Lambda)$ and $\mathcal{A}_{p_T}(\gamma)$ for a cone of magnitude one, they are defined as:

$$\mathcal{A}_p(X) = \frac{p_X - p_{cone}}{p_X + p_{cone}}, \tag{5.4}$$

the normalized difference between the momentum of a given particle (X) and the total momentum of the tracks in a cone around the particle, equivalently for the transverse momentum. These variables are useful to remove certain background candidates, mainly arising from other not fully reconstructed decay modes, as particles that have not been properly reconstructed will enhance the cone total momentum over the momentum of the particle X.

The internal parameters of the XGBoost BDT algorithm are optimized using a parameter space grid search for each BDT independently. The parameters used for this optimization are as follows: the number of trees, the learning rate, the maximum depth and the minimum splitting loss, more information on these can be found in Ref. [97]. The chosen configurations for the different BDT's are shown in Table 5.11.

Variables
$p\ p_T + \pi^{\pm}\ p_T + \gamma\ p_T$
$\pi^{\pm}\ p_T$
$\pi^{\pm}$ IP
p IP χ^2
Tracks DOCA
$\gamma\ p_T$
$\gamma\ \eta$
$\Lambda\ p_T$
Λ IP
Λ IP χ^2
Λ FD
$\Lambda_b^0\ p_T$
Λ_b^0 MTDOCA
$\Lambda\ \mathcal{A}_p$ Cone(1.0)
$\Lambda\ \mathcal{A}_{p_T}$ Cone(1.0)
$\gamma\ \mathcal{A}_{p_T}$ Cone(1.0)

Table 5.10: Input variables common to the three BDT's.

Year BDT	Num. trees	Learning rate	Max. depth	Min. split loss
2015+16	600	0.2	2	0.3
2017	1000	0.1	3	0.1
2018	1000	0.1	3	0.3

Table 5.11: Internal parameters of the three BDT's, corresponding to the 2015 & 2016, 2017 and 2018 BDT.

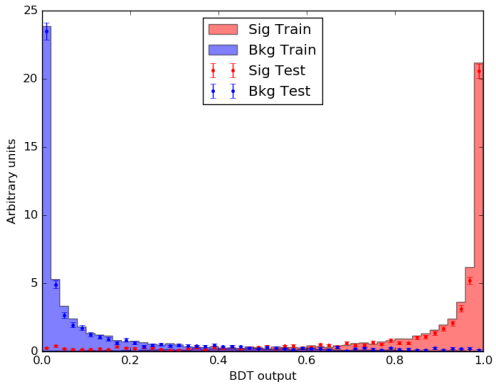

(a)

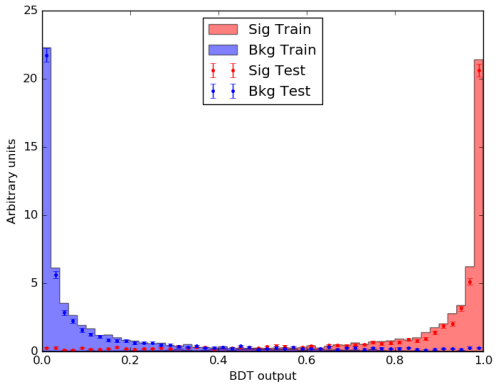

(b)

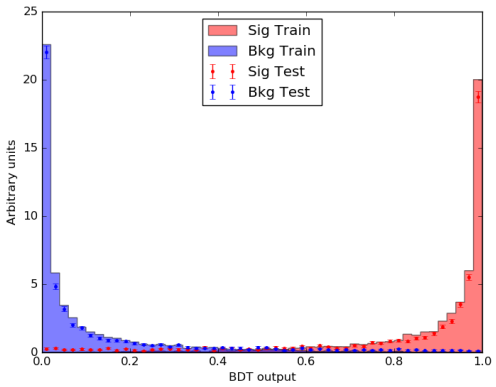

(c)

Figure 5.8: BDT outputs for (a) 2016 (b) 2017 and (c) 2018 of BDT-half B.

A two-fold scheme is used in the training and the application of the BDT's. For each data-taking period, the data and simulated candidates are randomly split into two different samples; A and B. Each one of these samples is used to train its own BDT. As is common in these MVA's the samples are further split into training and testing, in this case with a 2 to 1 ratio (66% and 33% respectively), allowing to check the overtraining. The final result is that two trained BDT's are produced for each data-taking period. Then each BDT's is applied to its counterpart. The performance plots of the training versus the testing samples, Figs. 5.8, show small effects from small overtraining.

Another possible issue with MVA's selections, given their supervised learning, is the production of biases, for example on the Λ_b^0 invariant mass. Notice that the proxy for combinatorial background candidates are data candidates with invariant masses above a particular value, while the signal proxies have invariant masses around the Λ_b^0. Thus the usage of the invariant mass directly or variables correlated with it could induce a very problematic bias. To ensure that this is not the case, the sixteen variables used in the BDT's are chosen so they cannot be directly related to the invariant mass. Moreover, a check on the output is also performed. The efficiency

of a given cut on the output BDT variable is studied in bins of the Λ_b^0 invariant mass, for both simulated candidates, high mass and low mass data candidates. This procedure allows to check if there is any trend (correlation) on the efficiency of the BDT depending on the invariant mass. More details on this cross-check can be found in App. A.4 for the different data-taking periods. No correlation can be established.

Once the training of each BDT has been validated, the end result are two similar BDT's (A,B) for each data-taking period. Therefore, an optimal requirement of the cut value of the output BDT variable is studied as the next step, through the use of figures-of-merit (FoMs). These are constructed to specifically maximize the sensitivity to the photon polarization, and are extracted from pseudo-experiments using a simplified version of the angular fit described in Sec. 5.6.

The sensitivity to the photon polarization is expected to depend on the signal and background yields. Therefore, sets of pseudo-datasets are generated with different number of signal candidates, and signal over background ratios. Then. the sensitivity to the photon polarization is extracted from each pseudo-datasaet. The results of these pseudo-experiments are shown in Fig. 5.9. Pseudo-datasets, with the same number of signal candidates, are grouped in collections and are fit, using two different expressions; $\sigma^{(1)}_{\alpha_\gamma}, \sigma^{(2)}_{\alpha_\gamma}$, defined as:

$$\sigma^{(1)}_{\alpha_\gamma} = \frac{p_0}{\sqrt{S}} + \frac{p_1}{\sqrt{S/B}} \quad \text{and} \quad \sigma^{(2)}_{\alpha_\gamma} = \frac{p_2}{\sqrt{S}} + \frac{p_3}{\sqrt{S/B}} + \frac{p_4}{S\sqrt{S/B}} \tag{5.5}$$

where p_0 and p_1 are averaged out for the different collections, and p_2, p_3 and p_4 are obtained using a simultaneous fit of all the collections. Maximizing the sensitivity to the photon polarization refers to reducing $\sigma^{(1)}_{\alpha_\gamma}$ or $\sigma^{(2)}_{\alpha_\gamma}$ to minimal values. Therefore, inverting Eq. 5.5 directly provides two FoMs to optimize the cut on the BDT output variable. The final expression for the two FoMs are:

$$\text{FoM}^{(1)} = \frac{\sqrt{S}}{1.59 + 0.047\sqrt{B}} \tag{5.6}$$

$$\text{FoM}^{(2)} = \frac{\sqrt{S}}{1.60 + (0.00152 + \frac{6.54}{S})\sqrt{B}} \tag{5.7}$$

where S and B are the number of signal and background candidates in the signal region. To find the optimal cut for the dataset used in the analysis, the computation of the signal yield, S, is performed as a multiplication of various parameters:

$$S = \mathcal{L} \cdot \sigma_{pp} \cdot f_{\Lambda_b^0} \cdot \mathcal{BR}\left(\Lambda_b^0 \to \Lambda\gamma\right) \cdot \epsilon^{MC}_{BDT} \tag{5.8}$$

where $\mathcal{L}$ is the luminosity for each data-taking period, σ_{pp} is the $p-p$ cross-section [98], $f_{\Lambda_b^0}$ is the Λ_b^0 hadronization fraction [99] and $\mathcal{BR}\left(\Lambda_b^0 \to \Lambda\gamma\right)$ is the $\Lambda_b^0 \to \Lambda\gamma$ branching ratio [37], which are constant. While ϵ^{MC}_{BDT} is the efficiency of signal candidates, given a BDT output cut, in the simulation samples. The background yield, B, is computed using a data driven approach; for each value of the

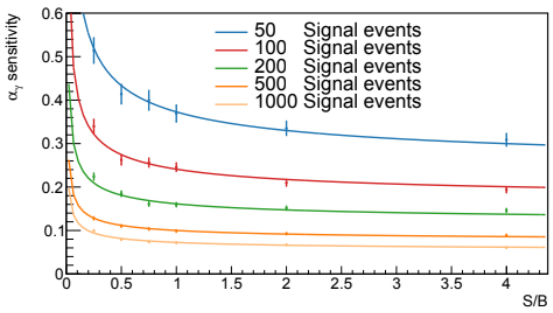

Figure 5.9: Sensitivity to the photon polarization as a function of the signal yield and the signal over background ratio, as extracted from pseudo-experiments (markers) [2]. Collections of pseudo-experiments with the same number of generated signal events are ploted in the same colour. The result of the fit using $\sigma^{(1)}_{\alpha_\gamma}$ from Eq. 5.5 is overlaid.

BDT output cut a fit is performed to the Λ_b^0 invariant mass outside the signal region and the number of background candidates inside the signal region is extrapolated from it.

The usage of a two-fold technique results in two possible optimal BDT output cut values for each data-taking period, from the application of one of the FoMs to the two halves (A,B). The average of the two is taken as the nominal BDT output cut for each data-taking period. The optimization of the two FoMs results in two different selection working-points.

In Fig. 5.10 FoM values depending on the BDT output for 2017 are represented for both FoMs. The maximum corresponds to the optimal value. The large error bars arise mainly from the uncertainty of the constant parameters used to compute the signal yield thus are fully correlated for all points. The results of the optimized BDT output cut values with the corresponding signal efficiency on the simulated samples and background rejection on the high Λ_b^0 invariant mass side band for each data-taking period are presented in Table 5.12. In App. A.3 all the plots for both BDT outputs (overtraining test) and FoMs for each data-taking period are shown.

To ease the notation, the two selection working-points from now on are referred as tight and loose, arising from Eq. 5.6 and Eq. 5.7 respectively. The loose configuration has a higher signal efficiency while the background rejection is lower, thus providing more signal and background candidates, while the tight selection obtains less signal candidates but also less background.

5.3.5 Photon Identification

After the BDT stage, a final requirement is applied to the photon candidates used to reconstruct $\Lambda_b^0 \to \Lambda\gamma$ decays to suppress potential miss-identification of merged π^0. These correspond to two photons from a π^0 decay which end up at the same ECAL cluster, and thus can be miss-identified as a single photon. The neutral tool `IsPhoton` [23] is used to separate the two cases. Through an MVA it uses

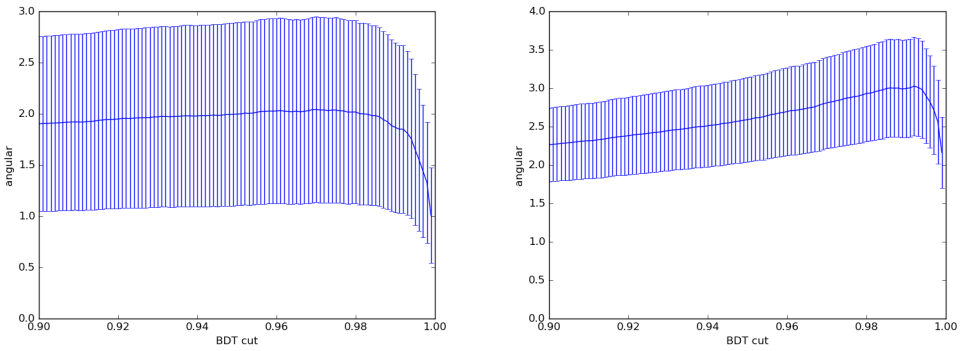

(a) (b)

Figure 5.10: Figure-of-merit values depending on the BDT output cut value, for (a) loose selection of 2017 data (BDT-half A) and (b) tight selection of 2017 data (BDT-half A).

Years		2015+2016	2017	2018
Loose	BDT val.	0.961	0.969	0.9615
	Sig eff. (%)	55.13	50.40	52.07
	Bkg rej. (%)	99.12	99.47	99.38
Tight	BDT val.	0.988	0.991	0.9865
	Sig eff. (%)	37.57	31.82	35.30
	Bkg rej. (%)	99.75	99.86	99.83

Table 5.12: Values for the optimal BDT output cut value, the signal efficiency and the background rejection for each data-taking period and configuration, loose (Eq. 5.7) and tight (Eq. 5.6).

the characteristic that merged π^0 have a different electromagnetic cluster shape, much broader, than single photons. A requirement of $\gamma_{\text{IsPhoton}} > 0.6$ is used. This final stage has a signal efficiency larger than 95% in the simulated samples while suppressing the background contribution from $\Lambda_b^0 \to \Lambda\pi^0$ decays.

5.4 Invariant mass fit

After the selection and reconstruction of the different decay channels of interest, a disentanglement of the signal contribution from the remaining background contributions is needed to extract the attributes of interest of each decay mode. These background contributions are studied in this Section. An unbinned maximum likelihood fit is performed to the candidate Λ_b^0 invariant mass distribution, within a window of 900 MeV/c^2 around the PDG world average Λ_b^0 mass (5619.60 ± 0.17 MeV/c^2) [37]. This is especially relevant to later perform the angular fit of the selected $\Lambda_b^0 \to \Lambda\gamma$ candidates to extract the photon polarization, as the signal and background yields obtained through this method are used in the final angular fit strategy. This is done for both selections, tight and loose. In particular, these yields are extrapolated to an even smaller mass window of 2.5σ around the Λ_b^0 world average, with $\sigma = 93$ MeV/c^2.

5.4.1 Signal mass modeling

After the selection procedure, candidates that are wrongly reconstructed as $\Lambda_b^0 \to \Lambda\gamma$ decays are still present. A part from the signal component, two different background components are found to be relevant to describe and fit the Λ_b^0 invariant mass distribution:

Combinatorial background As previously described, is the combination of real Λ baryons with arbitrary photons, which are able to pass through the different selection steps, including the MVA. It is the dominant background contribution and covers all the invariant mass phase space. Its relevance decreases with the invariant mass.

Physical background A background contribution arising from a partially reconstructed decay. In this case, a photon is not reconstructed from the decaying meson η, $\eta \to \gamma\gamma$ which comes from the $\Lambda_b^0 \to \Lambda\eta$ decay mode. Given the lack of reconstructed energy, due to the missing photon, the contribution is expected to be present at lower Λ_b^0 invariant masses.

Signal model

The invariant mass distribution for the signal contribution is modeled as a double-sided Crystal Ball (dsCB) [100]. Which is built by mixing a Gaussian core with two

power-law tails:

$$\mathrm{dsCB}(m;\mu,\sigma,\alpha_i,n_i) = N\cdot\begin{cases} A_L\cdot\left(B_L-\frac{m-\mu}{\sigma}\right)^{-n_L}, & \text{for } \frac{m-\mu}{\sigma}\leq-\alpha_L \\ \exp\left(-\frac{(m-\mu)^2}{2\,\sigma^2}\right), & \text{for } -\alpha_L<\frac{m-\mu}{\sigma}<\alpha_R \\ A_R\cdot\left(B_R+\frac{m-\mu}{\sigma}\right)^{-n_R}, & \text{for } \frac{m-\mu}{\sigma}\geq\alpha_R \end{cases}, \quad (5.9)$$

where N is the normalization factor and,

$$A_i = \left(\frac{n_i}{|\alpha_i|}\right)^{n_i}\exp\left(-\frac{1}{2}|\alpha_i^2|\right), \quad B_i = \frac{n_i}{|\alpha_i|}-|\alpha_i|, \quad (5.10)$$

with $i=\{L,R\}$ referring to left and right sides. Resulting in a total of six free parameters: μ and σ for the Gaussian-like core and n_L, n_R, α_L and α_R for the power-law tails. The two power-law tails account for different energy effects. The right-handed tail takes into account effects from pile-up at the ECAL, increasing the energy of the photon, while the left-handed tail accounts for the energy loses produced by the interaction with the detector material.

Due to the complexity of the invariant mass fit to the data samples, that also contain background contributions, some of the free parameters are fixed using the simulated samples. For the signal component, a first fit is done to simulated signal candidates, after the full selection, to extract the power-law tail parameters and the width (σ) of the Gaussian core, which are then fixed in the fit to the data. The fully selected simulated candidates from the three $\Lambda_b^0\to\Lambda\gamma$ samples are merged and weighted according to the luminosity of each corresponding periods of data-taking and used for this purpose.

The mean (μ) of the Gaussian core is allowed to be free in the final fit to the data samples. The signal yield, which is one of the focuses of the invariant mass fit, is also allowed to be free in the final invariant mass fit to the data samples. The results of the signal simulated sample invariant mass fits for the tight and loose selection are shown in Fig. 5.11. The values of the parameters show a good statistical agreement between configurations, as expected.

Combinatorial background model

The combinatorial background is modeled by an exponential distribution, with one free parameter (τ):

$$\mathrm{Exp}(m;\tau) = \frac{1}{\tau}\cdot\exp(m\tau), \quad (5.11)$$

The yield of this contribution and the τ parameter are allowed to be free in the full invariant mass fit to the data samples.

Physical background model

The partially reconstructed background arising from the $\Lambda_b^0\to\Lambda\eta$ mode is modeled by an Argus function (Eq. 5.12) convolved with a Gaussian distribution, to modelize

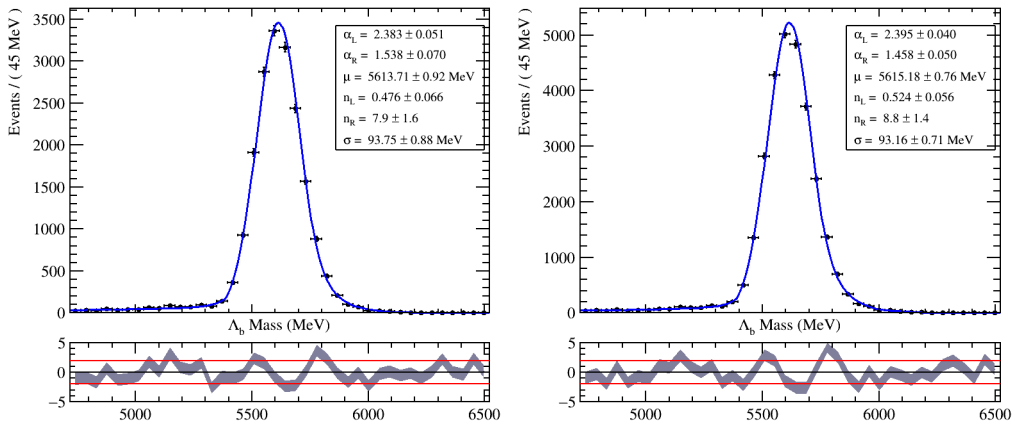

Figure 5.11: Invariant mass distributions of simulated $\Lambda_b^0 \to \Lambda\gamma$ signal candidates for (a) tight selection, (b) loose selection. The fitted parameter values are detailed in the legend

the effects arising from the detector resolution.

$$\mathrm{A}(m; m_0, c, p) = \mathcal{C}(m_0, c, p) \cdot m \cdot \left[1 - \left(\frac{m}{m_0}\right)^2\right]^p \cdot \exp\left[c \cdot \left(1 - \left(\frac{m}{m_0}\right)^2\right)\right] \quad (5.12)$$

The Argus distribution has a total of three free parameters, namely m_0, c, p while $\mathcal{C}(m_0, c, p)$ is simply the normalization term, the distribution is only defined in the range of $0 \leq m \leq m_0$. The Argus distribution is useful to describe partially reconstructed backgrounds given its cut-off-like parameter (m_0), since Λ_b^0 partially reconstructed candidates have a lower invariant mass than real Λ_b^0 candidates, due to the missed particle/energy. While the Gaussian distribution is used so the detector resolution is also taken into account.

Similarly to what is done in the modeling of the signal contribution, simulated samples are used to fix the free parameters and avoid an overly ambiguous final invariant mass fit. Notice that the Gaussian convolution should add two free parameters to the previous three, for a total of five, but the mean is forcefully set to have a null value beforehand, therefore only four remain, these are fit to the simulated samples and fixed thereafter. The partially reconstructed simulated $\Lambda_b^0 \to \Lambda\eta$ candidates are reconstructed and selected using exactly the same strategy of the $\Lambda_b^0 \to \Lambda\gamma$ mode for all stages, including the two BDT selections, and reproducing the absence of a photon coming from the η meson decay. Due to the lack of $\Lambda_b^0 \to \Lambda\eta$ simulated samples for 2017 and 2018 data-taking periods, the fit is produced only using 2016. No major differences are expected to arise from this particularity. Shown in Fig.. 5.12 are the fits to the simulated $\Lambda_b^0 \to \Lambda\eta$ candidates, after the two selection working points along the values of the corresponding fitted parameters, which also show a good agreement between the two configurations.

The yield of $\Lambda_b^0 \to \Lambda\eta$ candidates is Gaussian constrained to the expected contamination of this background over the signal component, i.e. proportional to

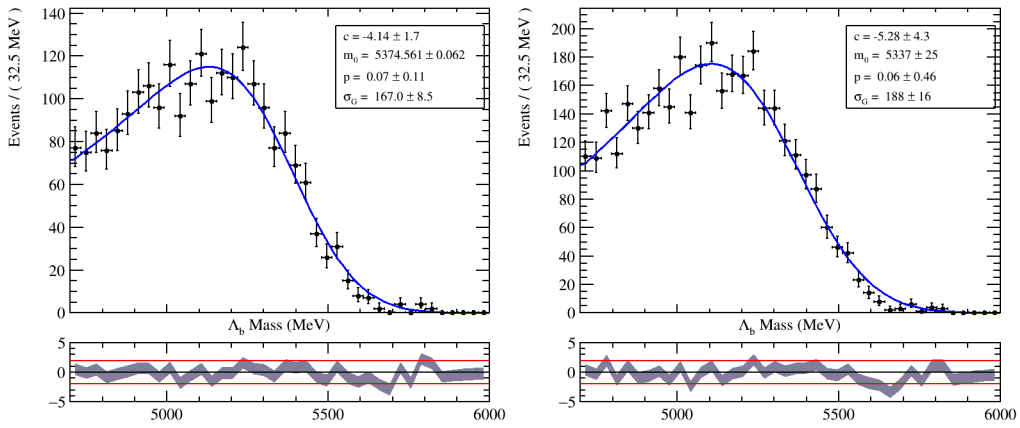

(a) (b)

Figure 5.12: Invariant mass distributions of simulated $\Lambda_b^0 \to \Lambda\eta$ partially reconstructed candidates for (a) tight selection, (b) loose selection. The fitted parameter values are detailed in the legend, the mean of the Gaussian is fix to zero.

the signal yield. The expected contamination (C) and its uncertainty are estimated as the following ratio:

$$C^{sel} = \frac{N^{sel}_{\Lambda_b^0 \to \Lambda\eta}}{N^{sel}_{\Lambda_b^0 \to \Lambda\gamma}} = \frac{\mathcal{B}(\Lambda_b^0 \to \Lambda\eta)\,\mathcal{B}(\eta \to \gamma\gamma)}{\mathcal{B}(\Lambda_b^0 \to \Lambda\gamma)} \times \frac{\epsilon^{sel}_{\Lambda_b^0 \to \Lambda\eta}}{\epsilon^{sel}_{\Lambda_b^0 \to \Lambda\gamma}}, \tag{5.13}$$

where ϵ_i^{sel} are the full selection efficiencies of each channel, which can be found in Table 5.13 along the values of the different branching ratios. Other terms, also present in Eq. 5.8, such as $\mathcal{B}(\Lambda \to p\pi)$, f_{Λ_b}, $\mathcal{L}$ and σ_{pp} cancel out.

The efficiencies for both channels are extracted from the corresponding simulation samples, which are corrected using the re-weighting scheme presented in Sec. 5.3.3. The uncertainties on the branching ratios are propagated to the expected contamination. The major uncertainty contribution arises from the poor knowledge of the branching ratio of $\Lambda_b^0 \to \Lambda\eta$ decays. Thereafter, possible systematic uncertainties arising from the computation of the efficiencies via the use of the simulated samples, particularly when extracting the efficiencies from the online selection, are considered to be very small in comparison.

Even though the yield for $\Lambda_b^0 \to \Lambda\eta$ decays is constrained within its precision, the poor knowledge of the branching ratio of $\Lambda_b^0 \to \Lambda\eta$ decays may still be a source of concern. Causing an effect to the extraction of the signal and background yields and therefore a non-negligible effect in the measurement of the photon polarization. To lessen it, in Sec. 5.7 a systematic uncertainty is proposed to cover possible wrong hypotheses used in the extraction of the yields using this invariant mass fit strategy.

Lastly, other possible sources of physical backgrounds were investigated in Ref. [45] and found to be negligible. Most relevantly, $\Lambda_b^0 \to \Lambda(1520)\gamma$ decays where the exited baryon decays into: $\Lambda(1520) \to \Lambda\pi\pi$ and $\Lambda(1520) \to (\Sigma \to \Lambda\gamma)\pi^0$, are

	Loose	Tight
$\mathcal{B}(\eta \to \gamma\gamma)$	0.394 ± 0.002	
$\mathcal{B}(\Lambda_b^0 \to \Lambda\eta)$	$(9^{+7}_{-5}) \cdot 10^{-6}$ [37]	
$\mathcal{B}(\Lambda_b^0 \to \Lambda\gamma)$	$(7.1 \pm 1.7) \cdot 10^{-6}$ [37]	
$\epsilon^{MC}_{\Lambda_b^0 \to \Lambda\eta}$	$1.83 \cdot 10^{-5}$	$1.16 \cdot 10^{-5}$
$\epsilon^{MC}_{\Lambda_b^0 \to \Lambda\gamma}$	$9.09 \cdot 10^{-5}$	$5.89 \cdot 10^{-5}$
C	0.100 ± 0.082	0.098 ± 0.080

Table 5.13: Values of the different branching ratios, the efficiencies obtained through the simulated samples and the final contamination of $\Lambda_b^0 \to \Lambda\eta$ for the loose and tight selections

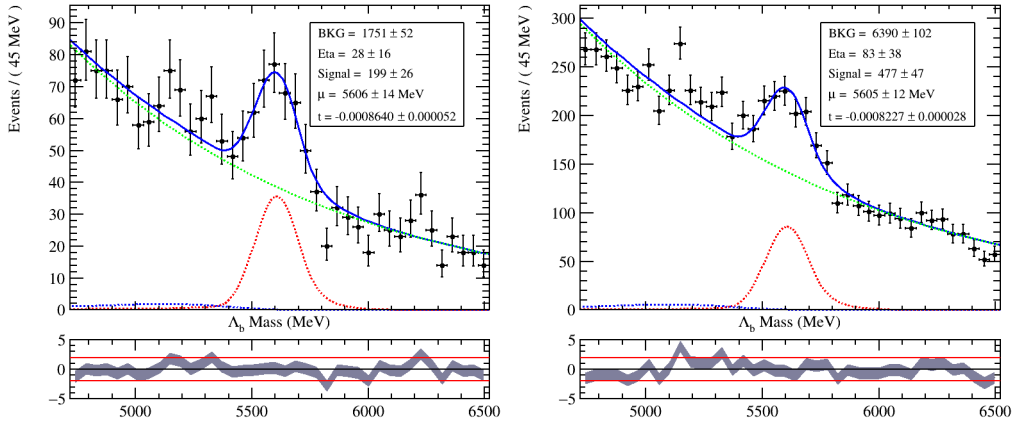

(a) (b)

Figure 5.13: Invariant mass distributions of $\Lambda_b^0 \to \Lambda\gamma$ data candidates (black markers) for (a) tight selection and (b) loose selection. The result of the invariant mass fit is overlaid. The total PDF is represented by the solid blue curve, while the signal, combinatorial and partially reconstructed $\Lambda_b^0 \to \Lambda\eta$ background are displayed by the dashed red, green and blue curves, respectively.

expected smaller than the $\Lambda_b^0 \to \Lambda\eta$ component and with a similar shape, this is covered by the previously mentioned systematic uncertainty.

5.4.2 Yield extraction

The invariant mass models described above are used to fit the selected data candidates for both configurations, tight and loose. The results of the mass fits for full Run 2 data samples are presented in Fig. 5.13 and the values of the yields and fit parameters are quoted in Table 5.14. A peak with good significance around the Λ_b^0 world average mass is observed, along a diminishing combinatorial background toward higher masses. The signal mean is found to be in very good agreement between the two selections and the PDG world average Λ_b^0 invariant mass. Also the combinatorial background parameter is in agreement among selections, supporting the notion of a BDT output uncorrelated with the candidate mass.

	Tight	Loose
μ (MeV/c^2)	5606 ± 14	5605 ± 12
τ	-0.00086 ± 000005	-0.00083 ± 0.00003
N_{sig}	199 ± 26	477 ± 47
N_{comb}	1751 ± 52	6390 ± 102
$N_{\Lambda_b^0 \to \Lambda\eta}$	28 ± 16	83 ± 38
χ^2/ndof	40.7/35	63.1/35

Table 5.14: Parameters of the unbinned maximum likelihood invariant mass fit to Run 2 data for the tight (a) and loose (b) selections. The χ^2 parameter is computed for the shown binning scheme.

	Tight	Loose
$N_{sig}^{2.5\sigma}$	186 ± 24	444 ± 44
$N_{comb}^{2.5\sigma}$	396 ± 12	1460 ± 23
$N_{\Lambda_b^0 \to \Lambda\eta}^{2.5\sigma}$	4 ± 2	10 ± 4

Table 5.15: Signal and background yields of a reduced invariant mass region (2.5σ) numerically computed using the fitted PDFs.

Following the strategy presented previously, the goal is to extract the yields in a smaller invariant mass window of 2.5σ around the Λ_b^0 world average, explicitly: $[5387.1, 5852.1]$ MeV/c^2. Therefore, the fitted PDFs are numerically integrated in this window. The results for the three components are shown in Table 5.15. Most noticeable is the small contribution to the total yield that the partially reconstructed background has in this reduced mass window. As discussed, the sensitivity to the photon polarization depends on both the signal yield and the signal over background ratio, which for the tight and loose selections is $s/b = 0.46 \pm 0.04$ and 0.30 ± 0.02, respectively. The tight configuration provides higher purity but lower signal yield, while the loose has the opposite behaviour.

5.4.3 Control modes mass modeling

$\Lambda_b^0 \to \Lambda J/\psi$ mode

The selected $\Lambda_b^0 \to \Lambda J/\psi$ candidates are used to control the acceptance of the proton helicity angle via the use of the sFit technique, therefore a good disentanglement of signal and background components is needed. Similarly to the signal mode, the signal component for this channel is modeled by a double-sided Crystal Ball with its tail parameters promptly fixed via a fit to the simulated samples. Also, the combinatorial background contribution is modeled as an exponential. Given the high purity and yield of this mode in the data samples, herein the reason to use it as a control mode, both the width and the mean of the Gaussian core are allowed to be free in the fit to data, along the exponential parameter and the two yields. No other background sources are considered. The invariant mass fit is displayed in App. A.5 and its usage is further explained in Sec. 5.5.

$\Lambda_b^0 \to pK^- J/\psi$ mode

The invariant mass model for the selected $\Lambda_b^0 \to pK^- J/\psi$ candidates has already been described in Sec. 5.3.3. The results of the fit are used to correct the simulated samples via the sFit technique. It uses a double-sided Crystal Ball to model the signal contribution and a first order polynomial to model the background component. The invariant mass fits for the different data-taking periods are presented in Fig. 5.5, showing a good description of the data.

5.5 Proton helicity angle

The proton helicity angle, θ_p, is the distribution used to measure the photon polarization of $\Lambda_b^0 \to \Lambda\gamma$ decays, following Eq. 5.3. A careful study of effects arising from the limited precision of the LHCb detector (resolution) and effects coming from the detector geometry, the reconstruction and selection (acceptance), that may affect the proton helicity distribution, is of utmost importance to extract the photon polarization via an angular fit. In this section, both are considered and studied via the use of the simulated samples presented in Sec. 5.2 and angular pseudo-experiments, used to measure the sensitivity to the photon polarization. The $\Lambda_b^0 \to \Lambda J/\psi$ channel is used to validate the usage of the simulated samples.

5.5.1 Resolution

The information present in the simulation samples is used to extract the detector resolution for the $\Lambda_b^0 \to \Lambda\gamma$ candidates. No differences for this effect are expected for the different data-taking periods, as no major changes have occurred in the detector performance. Therefore only simulated samples of 2016 are used to study the resolution. Since the simulation chain also simulates the detector response, the resolution can be extracted by subtracting the measured proton helicity angle value of the generated one for each candidate. For a better accuracy, the resolution is computed as the difference of measured and generated values in four equispaced bins of the cosine of the proton helicity angle, from 1 to -1. To model the resolution, the resulting distribution in each bin is fit using a double-Gaussian, the results are shown in Fig. 5.14. The values of the means and the standard deviations are presented in each corresponding legend. Means compatible with zero are observed while the widths of the different Gaussians are at the percent level. Therefore the resolution is expected to have a small effect on the computation of the photon polarization via the proton helicity angle.

Once the resolution has been modeled, the study of its effect on the photon polarization measurement is performed. For that purpose, different sets of pseudo-experiments using a simplified version of the angular fit strategy are generated. In particular, pseudo-datasets of the angular distribution ($\cos\theta_p$) are generated following the PDF:

$$\Gamma(\theta_p; \alpha_\gamma) = (\Gamma_{\text{theo}}(\theta_p) \cdot \text{Acc}(\theta_p)) \otimes \text{Res}, \tag{5.14}$$

were Γ_{theo} is the theoretical distribution presented in Eq. 5.3, Acc is the acceptance,

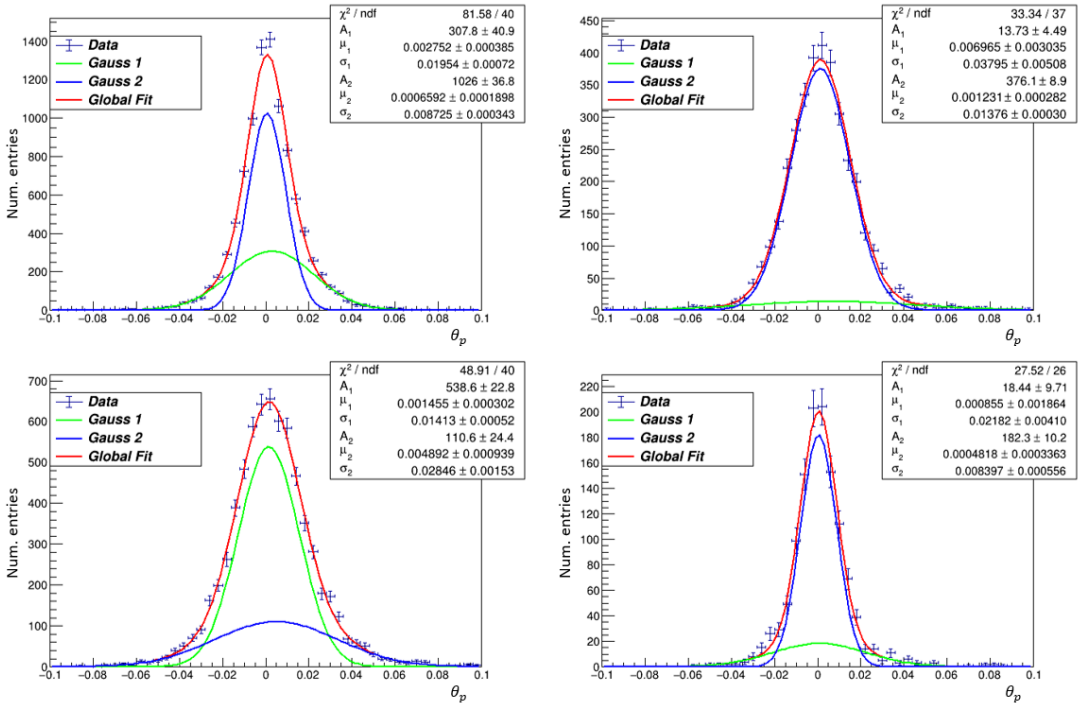

Figure 5.14: Angular resolution of simulated $\Lambda_b^0 \to \Lambda\gamma$ candidates in four equispaced bins of the proton helicity angle from -1 to 1. A fit of a double-Gaussian distribution is overlaid, the results of the fit are presented on the legend.

which is detailed later in this section, and Res is the double-Gaussian that characterizes the resolution. The values of the double-Gaussian parameters used are the maximal of the four different equispaced bins, therefore any effect should be considered an upper limit.

The pseudo-experiments generated with the PDF (Eq. 5.14) are fit using a reduced PDF that removes the resolution, to check for biases of not including it. It is worth mentioning that the acceptance used for the pseudo-experiments is extracted from the loose selection, due to the higher yield it presents. A value of $\alpha_\gamma = 1$, as predicted in the SM, is used for this approach. A total of 5000 pseudo-datasets are generated and fit, with 250 signal events each. The fit and pull distributions for the photon polarization parameter resulting from the pseudo-experiments are shown in Fig. 5.15. An in-depth commentary regarding the peculiarities found in these distributions is presented later in Sec. 5.6.3. Throughout this document, the photon polarization pull distributions are defined as the difference between the measured photon polarization value and the generated one divided by the uncertainty of each measurement (provided by the fitting algorithm).

If no bias is present, the measured photon polarization distribution is expected to follow a Gaussian distribution in which the mean is centered around the generated photon polarization value. The standard deviation corresponds to the sensitivity to the photon polarization. The pull distribution is expected, by definition, to also follow a Gaussian distribution, centered at zero and with a standard deviation of

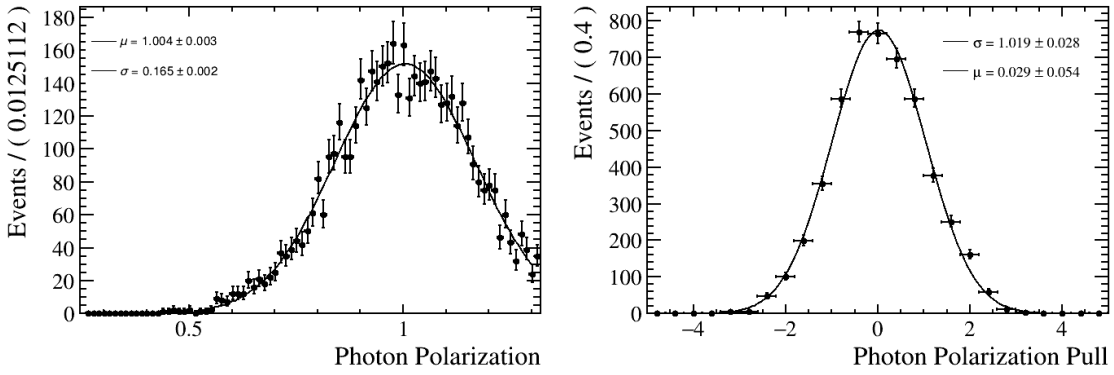

(a) (b)

Figure 5.15: Distributions of the photon polarization parameter (a) and pull distribution (b) obtained from pseudo-experiments generated with acceptance (loose) and resolution, and fit only with acceptance.

one. The Gaussian fits are preformed and no bias is found when the resolution is not included in the angular fit model, proving that it has a negligible effect on the angular fit. As a result, the angular resolution is not considered as a relevant effect towards the measurement of the photon polarization in subsequent sections and is not included in the fit to data.

5.5.2 Acceptance

The dependency of the reconstruction and selection efficiency with the proton helicity angle produces the acceptance. The shape of this effect is extracted by dividing the measured proton helicity distribution after the full selection in the simulated samples by the theoretical distribution used at the generation level, previously presented in Fig. 5.2.

The acceptance distribution is obtained by combining the simulated samples of the three data-taking periods. A comparison of the three samples for the tight selection is shown in Fig. 5.16. A good agreement between samples of different periods is observed, thus implying that the different trigger conditions and separate BDT selections among samples do not have a significant impact on the acceptance shape.

The combined acceptance distribution for both the loose and tight selections is shown in Fig. 5.17. Fits using different orders of Polynomial and Legendre functions were performed to fit the acceptance shape, and the one with the better description, using a χ^2 method, it selected as the nominal model. Therefore, a fourth order Polynomial function is used to model the angular acceptance. The values of the parameters for each configuration are shown in Table 5.16. The resulting shape of using Polynomials of the third and fifth order are used to compute a systematic uncertainty, as is detailed in Sec. 5.7.

To study the effect that the acceptance has on to the photon polarization mea-

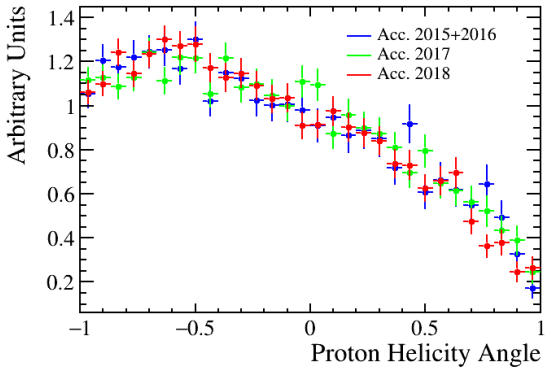

Figure 5.16: Proton helicity acceptance for $\Lambda_b^0 \to \Lambda\gamma$ candidates accepted by the tight selection using corrected simulated samples corresponding to 2016 (blue), 2017 (green) and 2018 (red) data-taking periods.

Selection	pol1	pol2	pol3	pol4
Loose	-0.48 ± 0.03	-0.17 ± 0.07	0.06 ± 0.04	-0.27 ± 0.08
Tight	-0.51 ± 0.03	-0.03 ± 0.09	0.08 ± 0.05	-0.36 ± 0.10

Table 5.16: Parameters of the fourth order polynomial modeling the helicity angular acceptance for the $\Lambda_b^0 \to \Lambda\gamma$ decay channel for the loose and tight selections.

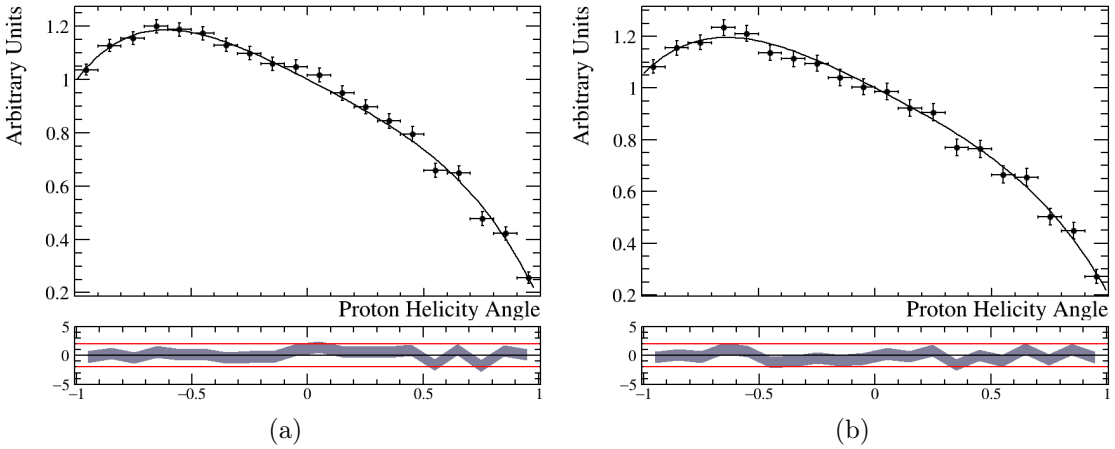

(a) (b)

Figure 5.17: Proton helicity acceptance for $\Lambda_b^0 \to \Lambda\gamma$ candidates using corrected MC samples fulfilling the (a) loose and (b) tight selection criteria. The fit using a fourth order polynomial is overlaid.

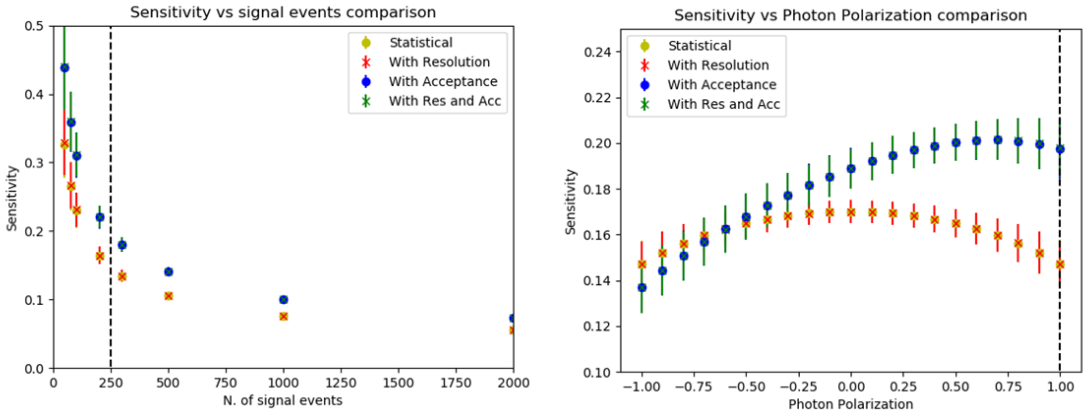

(a) (b)

Figure 5.18: Photon polarization sensitivity pseudo-experiments including different experimental effects for (a) different number of signal events and photon polarization set to one, (b) different hypothesis of the photon polarization and 250 signal events.

surement, equivalently to what is done for the resolution, pseudo-experiments are used. For completeness the resolution is also taken into account in some of these sets. Four different pseudo-experiment configurations are used to cover the possible combinations. In all four cases the PDF used to generate and fit each pseudo-experiment is the same. The first configuration considers no effects, therefore it only uses the simple theoretical signal distribution (Eq. 5.3), the second configuration takes into account the resolution, the third takes into account the acceptance, and the last one uses both the resolution and the acceptance.

The pseudo-datasets are generated using two different approaches. The first one is to compute the sensitivity to the photon polarization for different number of signal events, fixing the photon polarization to the SM prediction of one. In the second approach the sensitivity to the photon polarization is extracted with a fixed number of signal events (250) but the value of the photon polarization is varied from -1 to 1, therefore allowing for values not expected by the SM. The results of these studies can be seen in Fig. 5.18. The four pseudo-experiment configurations are shown but only two species are clearly distinguishable. The effect of including or excluding the resolution has no consequences on the sensitivity, confirming yet again the negligibility of the resolution effect. The acceptance, on the contrary, worsens the sensitivity in both approaches. It is worth pointing out that the acceptance worsens the sensitivity for most of the photon polarization values, including the SM one, but for small values of the photon polarization the acceptance effect enhances the sensitivity. This is due to the combined shape of the theoretical distribution and the acceptance along the small number of signal events used to generate the pseudo-datasets.

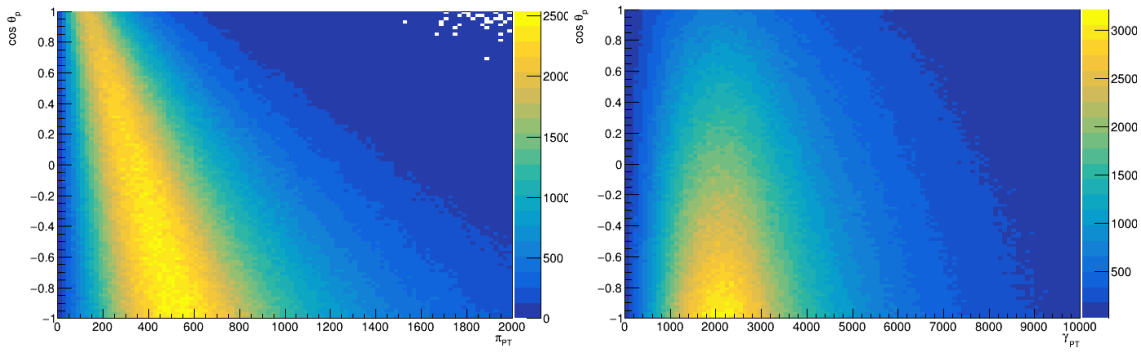

(a) (b)

Figure 5.19: Two dimensional histograms of the simulated samples at generation level of the cosine of the proton helicity angle versus the pion transverse momenta (a) and the photon transverse momenta (b). The correlation factors are 0.35 and 0.00067, respectively.

5.5.3 Acceptance characterization

The simulated samples have been used to study the different effects that affect the proton helicity angle, most relevantly the acceptance. Even though corrections have been applied to these samples to better simulate the data, as presented in Sec. 5.3.3, a deeper level of detail is required to have control over it. The $\Lambda_b^0 \to \Lambda J/\psi$ decay mode is used for this purpose.

The $\Lambda_b^0 \to \Lambda J/\psi$ channel is considered a good proxy to study the data and simulation agreement of the angular acceptance, because the acceptance is largely dominated by the requirements imposed on the hadronic part of the decay, which both control and signal modes share. This can be understood by studying the effects that the different selection steps have on the acceptance shape, using the simulated samples. In particular, Fig. 5.19 shows two-dimensional histograms of the cosine of the proton helicity angle versus the pion transverse momenta and the photon transverse momenta. Correlation with θ_p is observed for the pion transverse momenta while none is present for the photon.

Although the theoretical angular distributions for the signal decay and the control decay channels are different, the selection of the hadronic part of the decays is aligned. Thus, a good agreement of the acceptance in simulated and data $\Lambda_b^0 \to \Lambda J/\psi$ candidates would also ensure a good modeling for the $\Lambda_b^0 \to \Lambda\gamma$ simulated candidates.

The effect of different selection steps, namely; stripping, preselection and loose configuration (BDT), on the angular acceptance shape (multiplied by the theoretical distribution) can be observed in Fig. 5.20, along with the effects that different requirements on two of the most dominant variables; the pion transverse momenta and the proton IP χ^2, have. These are able to explain most of the actual acceptance shape. Most clearly, the requirement of $\pi^- p_{\mathrm{T}} > 300\,\mathrm{MeV}$ at the stripping level (Ta-

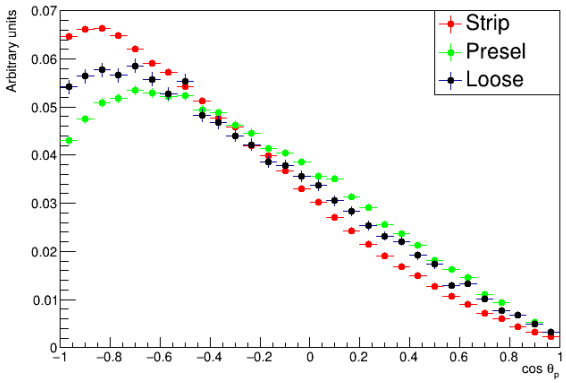

(a)

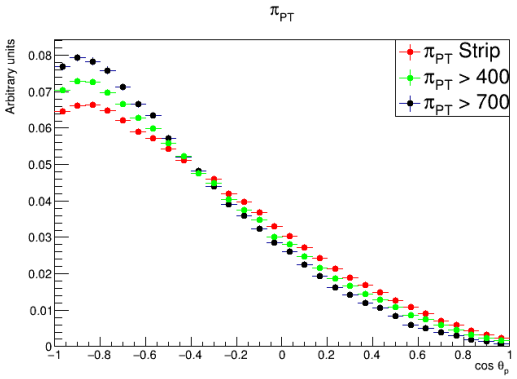

(b)

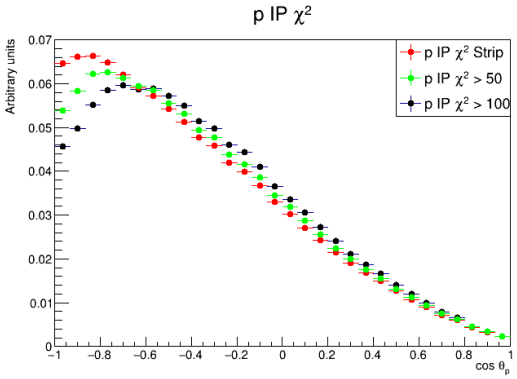

(c)

Figure 5.20: Distributions of the angular acceptance using simulated samples in (a) different selection steps. And after the stripping selection with different requiriments on (b) pion transverse momenta and (c) proton IP χ^2.

ble 5.4) has a very dominant effect. This can be understood taking a look at the $\pi^- p_{\mathrm{T}}$ generation level distribution in Fig. 5.19 (a), where a cut at 300 MeV would have a large impact.

The acceptance shape for $\Lambda_b^0 \to \Lambda J/\psi$ candidates in data is extracted using the sFit proccedure. Similarly to the process used in Sec. 5.3.3, for the $\Lambda_b^0 \to pK^- J/\psi$ mode, a maximum likelihood invariant mass fit of $\Lambda_b^0 \to \Lambda J/\psi$ candidates (App. A.5) is used to extract per-event sWeights, which are applied to the proton helicity distribution.

The sWeighted proton helicity distribution in the data samples is a mix of both the acceptance and the theoretical angular distribution of $\Lambda_b^0 \to \Lambda J/\psi$ candidates, therefore a disentanglement is needed. Knowledge of the theoretical distribution is thus required in order to do so. An integrated version of the theoretical $\Lambda_b^0 \to \Lambda J/\psi$ angular distribution, depending only on θ_p, is obtained from Ref. [101], which is experimentally extracted by the LHCb experiment.

The sWeighted proton helicity distribution is divided by the theoretical distribution to extract the angular acceptance for this mode. A comparison of the

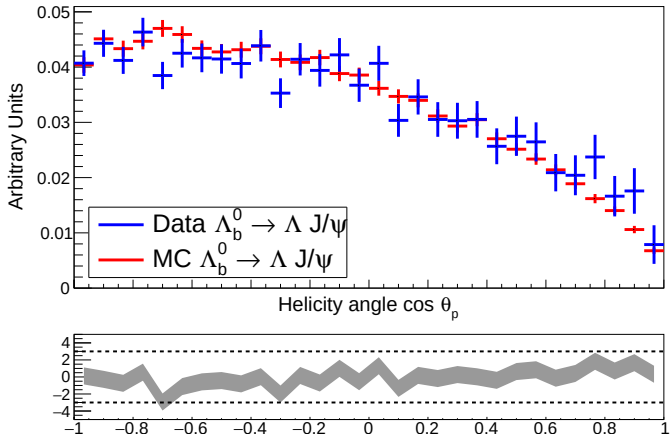

Figure 5.21: Angular acceptance from $\Lambda_b^0 \to \Lambda J/\psi$ sWeighted data (blue) and corrected MC (red), using all data-taking periods.

angular acceptance from sWeighted data and corrected simulated samples for the $\Lambda_b^0 \to \Lambda J/\psi$ mode is shown in Fig. 5.21 from Ref. [2]. A good statistical agreement is observed. Following this conclusion, the corrected simulated $\Lambda_b^0 \to \Lambda\gamma$ candidates are expected to reproduce, in a good measure, the signal acceptance shape of data candidates.

5.6 Angular fit strategy

The photon polarization is extracted from the proton helicity angle distribution by means of a maximum likelihood fit to data candidates in the reduced invariant mass window. The distribution in data includes; the shape of the signal candidates, the effect of the acceptance and the contribution from the background candidates. The PDF describing the proton helicity distribution is defined as follows

$$\Gamma(\alpha_\gamma;\theta_p) = \frac{S}{S+B}\left[\Gamma_{sig}(\alpha_\gamma;\theta_p)\cdot \mathrm{A}(\theta_p)\right] + \frac{B}{S+B}\Gamma_{bkg}(\theta_p) \tag{5.15}$$

where S and B are the signal and background yields in the reduced mass window, extracted from Table 5.15, $\Gamma_{sig}(\alpha_\gamma;\theta_p)$ is the theoretical distribution for $\Lambda_b^0 \to \Lambda\gamma$ candidates presented in Eq. 5.3, $\mathrm{A}(\theta_p)$ is the acceptance distribution and $\Gamma_{bkg}(\theta_p)$ is the angular distribution of combinatorial background candidates. No particular contribution arising from the $\Lambda_b^0 \to \Lambda\eta$ background candidates is included in the angular PDF, as discussed in 5.6.2.

5.6.1 Signal contribution

The proton helicity shape for the signal candidates is expressed as the multiplication of the theoretical distribution, presented in Eq. 5.3, and the acceptance shape. The parameters that comprise this shape are fixed, with the exception of the photon polarization. The fraction of candidates, $f = \frac{S}{S+B}$, is Gaussian constrained using

the results in Table 5.15. The parameters of the fourth order polynomial describing the acceptance are extracted from Table 5.16, for each selection. The Λ weak decay parameter is taken from the measurement performed by BESIII [84], which reports the measurements of the decay parameters of Λ and $\overline{\Lambda}$ baryons

$$\alpha_- = 0.750 \pm 0.009 \pm 0.004 \quad (5.16)$$

$$\alpha_+ = -0.758 \pm 0.010 \pm 0.007 \quad (5.17)$$

where the uncertainties are statistical and systematic, correspondingly. The average value, computed taking into account the correlation between the two parameters, $\rho(\text{stat}) = 0.82$ and $\rho(\text{syst}) = 0.835$, is found to be

$$\alpha_\Lambda = 0.754 \pm 0.004, \quad (5.18)$$

where the uncertainty includes both statistic and systematic effects.

5.6.2 Background contribution

The presence of background candidates in the reduced mass window needs to be considered to accurately measure the photon polarization of $\Lambda_b^0 \to \Lambda\gamma$ candidates. Two methods are considered, the first one is the nominal approach, which takes into account the background candidates as an additional term in the data distribution. The second approach uses the sFit technique to first remove the background candidate contribution. The latter strategy is finally not used, nevertheless is also presented in App. A.6.

The shape of the background candidates, which is majoritarily comprised of combinatorial background, is extracted by performing a fit to the proton helicity distribution of candidates present in the data side bands. These candidates are taken as the ones with a Λ_b^0 invariant mass higher (HMSB) or lower (LMSB) than 2.5σ around the world average Λ_b^0 mass, with $\sigma = 95\ \text{MeV/c}^2$. A comparison between the distribution of HMSB and LMSB candidates is shown in Fig. 5.22. A good agreement, given the available statistics, is observed.

Unfortunately, no theoretical prediction is available for the angular distribution of $\Lambda_b^0 \to \Lambda\eta$ events. To solve the impasse, the shape of the $\Lambda_b^0 \to \Lambda\eta$ is assumed to be the same as the combinatorial background distribution. This assumption is motivated by two considerations: the small amount of partially reconstructed candidates in the reduced mass window, compared to the other contributions, and the effect that the selection (acceptance) has on the angular distribution. The $\Lambda_b^0 \to \Lambda\eta$ candidates are only present in the LMSB but not in the HMSB, as presented in Sec. 5.4. Therefore, the good agreement that the LMSB and HMSB present in Fig. 5.22 reaffirms this assumption. Hence a single angular distribution is used to model the background in the fit to the data, including both combinatorial and $\Lambda_b^0 \to \Lambda\eta$ background candidates.

Similarly to the procedure presented in Section 5.5, the angular shape of the background is chosen after performing several fits using polynomial functions of different orders. A fourth order polynomial is selected, as it is found to provide the

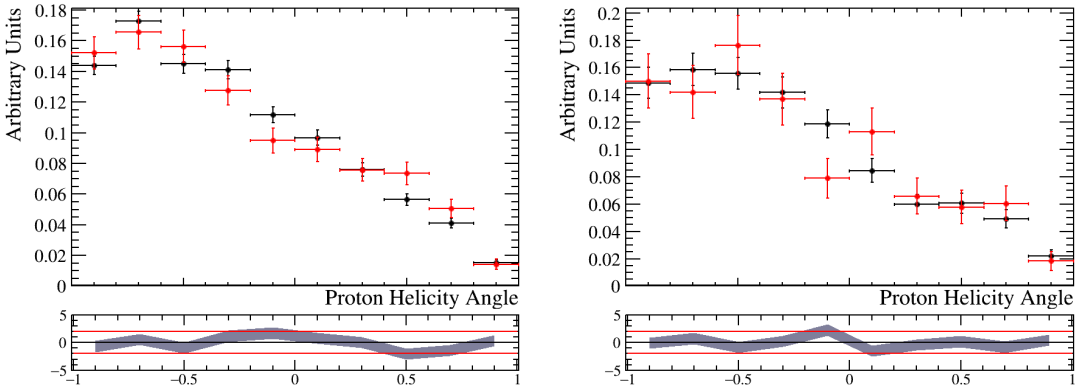

(a) (b)

Figure 5.22: Helicity distribution for $\Lambda_b^0 \to \Lambda\gamma$ candidates in the HMSB (red) and LMSH (black) from the full Run 2 data sample fulfilling the (a) loose and (b) tight selections.

Selection	pol1	pol2	pol3	pol4
Loose	-0.96 ± 0.06	0.20 ± 0.11	0.28 ± 0.08	-0.502 ± 0.12
Tight	-1.05 ± 0.12	0.54 ± 0.25	0.38 ± 0.16	-0.81 ± 0.27

Table 5.17: Parameters of the fourth order polynomial modeling the background helicity contribution of $\Lambda_b^0 \to \Lambda\gamma$ candidates present in the HMSB and LMSB for the loose and tight selections.

best description of the distribution, using χ^2 as a figure of merit. In Fig 5.23 the result of the fit to the side bands is shown for each selection. Also, the third and fifth order polynomials are studied as alternative models to compute a systematic uncertainty, arising from the choice of the modeling, in Sec. 5.7. The resulting parameters of the fits to the background distributions for both selections are shown in Table 5.17.

5.6.3 Angular fit validation

Various sets of pseudo-datasets are generated and fit in order to validate and asses the performance of the angular fit strategy for each selection. A total of 20000 pseudo-datasets are produced for each set. For each pseudo-dataset, the signal and background candidates are generated using their corresponding angular distributions. The candidate fraction is taken from the invariant mass fits of each selection, presented in Table 5.15. The photon polarization is generated using different values to have a larger coverage of the validity of the strategy. The generated pseudo-datasets are fit using Eq. 5.15, where the photon polarization is free and the candidate fraction is Gaussian constrained. The remaining parameters are fixed to the values obtained in previous sections. The angular fit mimics the same set up that is used when performing the fit to the data candidates.

The distribution of the fitted value of the photon polarization, α_γ, and the

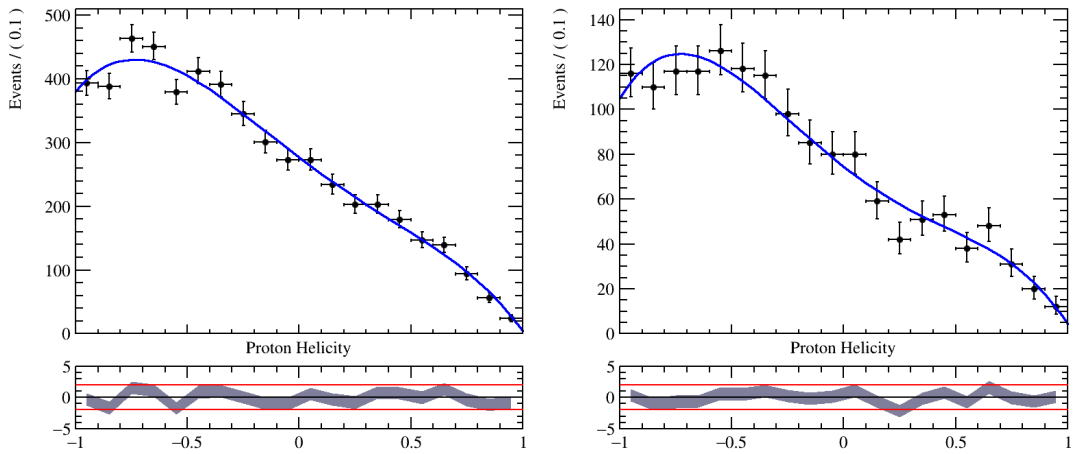

(a) (b)

Figure 5.23: Helicity distribution for $\Lambda_b^0 \to \Lambda\gamma$ candidates in both HMSB and LMSH from the full Run 2 data sample fulfilling the (a) loose and (b) tight selections. The fit using a fourth order polynomial is overlaid.

	Dispersion distribution		Pull distribution	
	μ	σ	μ	σ
$\alpha_\gamma = 1$	0.974 ± 0.005	0.351 ± 0.003	0.081 ± 0.020	1.071 ± 0.012
$\alpha_\gamma = 0.5$	0.509 ± 0.003	0.350 ± 0.002	0.020 ± 0.010	1.032 ± 0.008
$\alpha_\gamma = 0$	0.006 ± 0.002	0.326 ± 0.002	-0.017 ± 0.007	0.988 ± 0.005

Table 5.18: Fitted mean and standard deviation of the α_γ dispersion and pull distribution of the sets of pseudo-datasets generated with a tight configuration.

corresponding pull distribution are shown in Fig. 5.24 and Fig. 5.25, for loose and tight selections, and for three different generation values of the photon polarization. The pull distribution is defined as difference of the measured and generated photon polarization divided by the uncertainty provided by the fit, and therefore, for unbiased psuedo-experiments is expected to follow a Normal-like behaviour. A Gaussian distribution is fit and overlaid for each set. The means and standard deviations of the fitted Gaussian distributions are detailed in Table 5.18 and Table 5.19, for tight and loose configurations respectively.

The angular PDF presented in Eq. 5.15 has a limited valid range given by

	Dispersion distribution		Pull distribution	
	μ	σ	μ	σ
$\alpha_\gamma = 1$	0.991 ± 0.003	0.270 ± 0.003	0.065 ± 0.020	1.054 ± 0.011
$\alpha_\gamma = 0.5$	0.505 ± 0.002	0.260 ± 0.001	-0.019 ± 0.007	0.988 ± 0.005
$\alpha_\gamma = 0$	0.005 ± 0.002	0.242 ± 0.001	0.003 ± 0.007	0.993 ± 0.005

Table 5.19: Fitted mean and standard deviation of the α_γ dispersion and pull distribution of the sets of pseudo-datasets generated with a tight configuration.

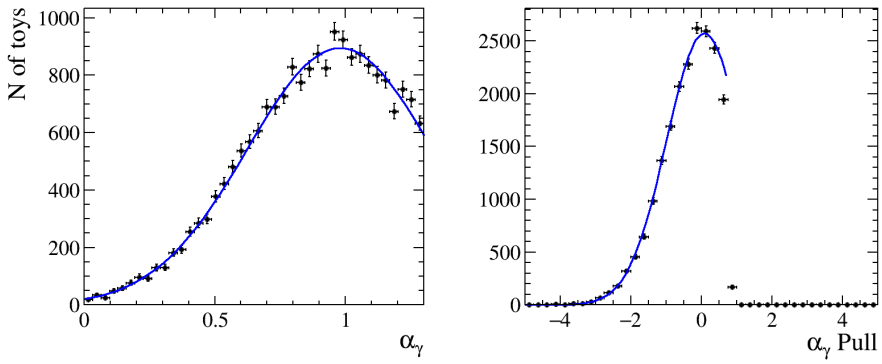

(a)

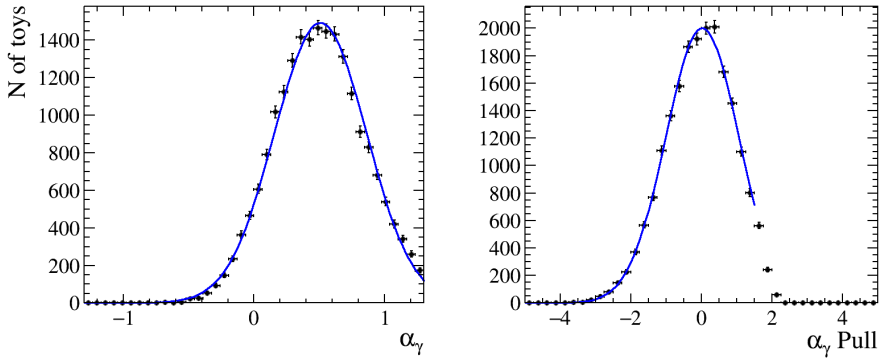

(b)

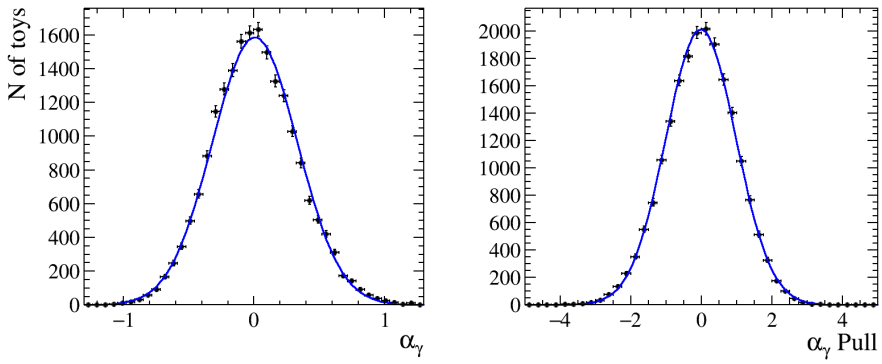

(c)

Figure 5.24: Dispersion distribution(left) and pull distribution (right) for α_γ fitted values for each set of pseudo-datasets. The pseudo-datasets are generated with the signal and background yields and the acceptance and background shapes of the tight configuration with (a) $\alpha_\gamma = 1$, (b) $\alpha_\gamma = 0.5$ and (c) $\alpha_\gamma = 0$. A Gaussian fit is overlaid.

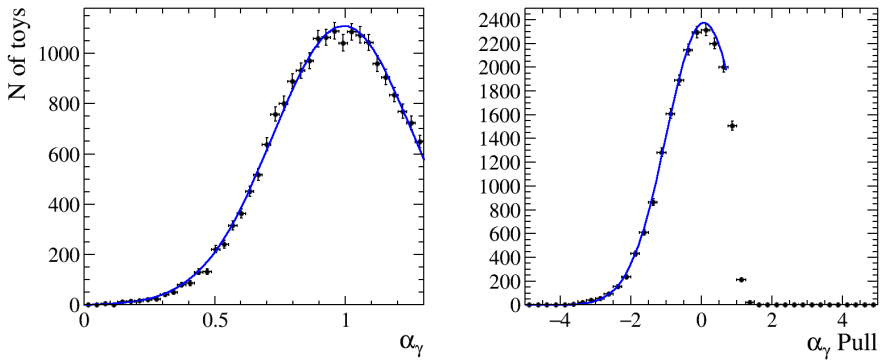

(a)

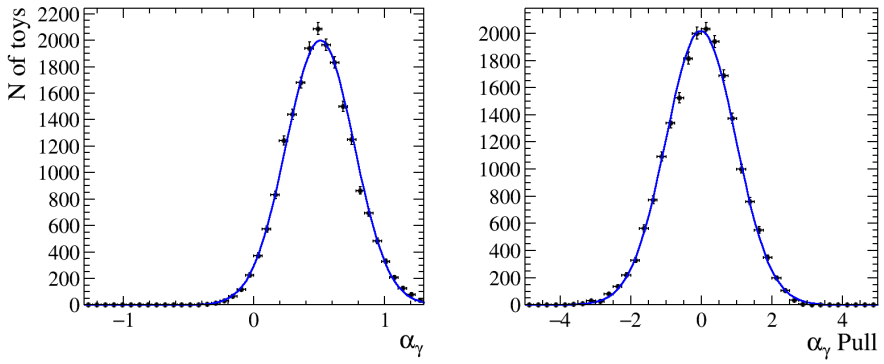

(b)

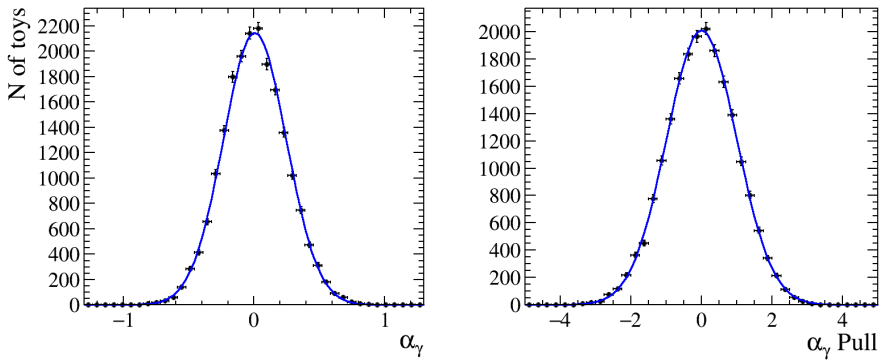

(c)

Figure 5.25: Dispersion distribution(left) and pull distribution (right) for α_γ fitted values for each set of pseudo-datasets. The pseudo-datasets are generated with the signal and background yields and the acceptance and background shapes of the loose configuration with (a) $\alpha_\gamma = 1$, (b) $\alpha_\gamma = 0.5$ and (c) $\alpha_\gamma = 0$. A Gaussian fit is overlaid.

$\alpha_\gamma = \pm\frac{1}{\alpha_\Lambda} = \pm 1.326$, out of which the PDF becomes negative. As a direct consequence, it is not possible to obtain fitted α_γ values greater than this value. This feature has small to no effect on the sets of pseudo-datasets generated with $\alpha_\gamma = 0$, as the valid range is far from the generated value of the photon polarization. But it has increasing consequences at $\alpha_\gamma = 0.5$ and $\alpha_\gamma = 1$, clearly observable in the corresponding figures. For these sets, the photon polarization dispersion is truncated and the right tail of the pull distribution does not have a Gaussian-like behaviour. This is further aggravated in the case of the tight selection, given the wider photon polarization dispersion, due to the lower statistics it presents with respect to the loose configuration. To tackle the issue, a veto is imposed in the fit range of the pull distribution.

The result of the fits to the pull distributions show compatibility, taking into consideration both the difficulties arising from the close PDF limit and the artificial veto imposed in the fit range, with a Normal distribution with null mean and a standard deviation of one ($\mu = 0, \sigma = 1$). The α_γ pull distributions of sets of pseudo-datasets far from the valid range (i.e. $\alpha_\gamma = 0, 0.5$) are able to cross-check possible concerns on the subject, as these are consistent with a Normal distribution. These indicate the presence of no biases and a good error coverage in the angular strategy.

On top of validating the angular fit strategy, the study using pseudo-experiments allows to extract the sensitivity to the photon polarization for different given values. In particular, for a SM-like value, i.e. $\alpha_\gamma = 1$, the expected sensitivity is 35% and 27% for the tight and loose selections, respectively. For both selections, this angular strategy has a substantially better performance than the sFit strategy. Furthermore, it also favours the loose configuration over the tight one, prior to computing the systematic uncertainties of each configuration.

5.6.4 Tagged measurements

Up until this point, the $\Lambda_b^0 \to \Lambda\gamma$ mode is used as a general notation to include both $\Lambda_b^0 \to \Lambda\gamma$ and $\overline{\Lambda}_b^0 \to \overline{\Lambda}\gamma$ decay modes. Nevertheless, these decays are self-tagged processes, meaning that the charge of the final state particles, the proton-pion pair, directly provide with the knowledge to separate both decay modes. Therefore, as a complementary measurement, a potential effect of CPV in α_γ is studied by splitting the samples into tagged $\Lambda_b^0 \to \Lambda\gamma$ and $\overline{\Lambda}_b^0 \to \overline{\Lambda}\gamma$ decays. Due to splitting the statistics into approximately half for each decay mode, only the data samples with the loose selection are used for this study.

An analogous strategy to the one presented for the nominal photon polarization measurement is used to measure the photon polarization separately for $\Lambda_b^0 \to \Lambda\gamma$ and $\overline{\Lambda}_b^0 \to \overline{\Lambda}\gamma$ candidates, denoted as α_γ^- and α_γ^+ respectively. Due to the limited statistics, the invariant mass distributions, the acceptance shape and the angular background distribution are modeled using the loose sample. Possible differences of these shapes for $\Lambda_b^0 \to \Lambda\gamma$ and $\overline{\Lambda}_b^0 \to \overline{\Lambda}\gamma$ decays are considered as sources of systematic uncertainties, in Sec. 5.7

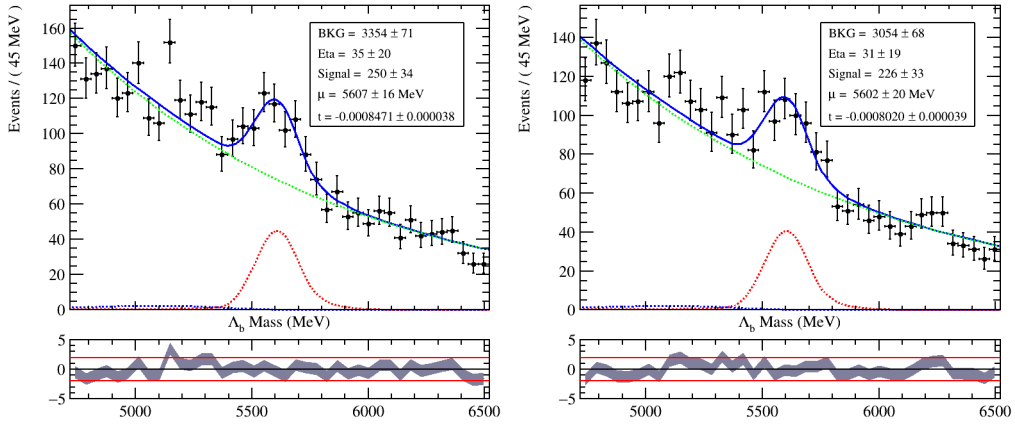

(a) (b)

Figure 5.26: Invariant mass distributions of (a) $\Lambda_b^0 \to \Lambda\gamma$ and (b) $\overline{\Lambda}_b^0 \to \overline{\Lambda}\gamma$ data candidates after the loose selection (black markers). The result of the invariant mass fit is overlaid. The total PDF is represented by the solid blue curve, while the signal, combinatorial and partially reconstructed $\Lambda_b^0 \to \Lambda\eta$ background are displayed by the dashed red, green and blue curves, respectively.

An invariant mass fit is performed in each sample to extract the yields in the reduced invariant mass window. The yields are then used as Gaussian constrains for the angular fit. The invariant mass distributions are shown in Fig. 5.26, where the results of independent maximum likelihood fits are overlaid. The signal is modeled with a double-sided Crystal-Ball with the width and tail parameters fixed to the values obtained from simulation (loose selection), while the mean is free. The slope and yield of the combinatorial background are also free. The shape of the partially reconstructed $\Lambda_b^0 \to \Lambda\eta$ background is fixed from simulation while the yield is constrained using the expected contamination. The results of the fit are provided in Tab. 5.20 and the yields obtained in the 2.5σ signal region used for the angular fit are reported in Tab. 5.21 for the different samples. A good agreement of the different free parameters is shown between $\Lambda_b^0 \to \Lambda\gamma$ and $\overline{\Lambda}_b^0 \to \overline{\Lambda}\gamma$ candidates. It is worth pointing out that by no means the difference of signal yield for the two decay modes is directly indicative of any potential CPV effect. It can only be understood as a raw asymmetry, as the performance of the LHCb experiment for particle and anti-particles, given the nature of both the detector and the proton-proton collisions, is not taken into account.

The signal and background yields in the reduced invariant mass window are used to generate pseudo-datasets (20000) in order to validate and extract the sensitivity to the photon polarization for each decay mode. The angular signal shape is described by the theoretical angular distribution (Eq. 5.3) multiplied by the acceptance shape. Most relevantly for $\Lambda_b^0 \to \Lambda\gamma$ decays $\alpha_\gamma = \alpha_\gamma^- = 1$ and $\alpha_\Lambda = \alpha_\Lambda^-$ (Eq. 5.16) and for $\overline{\Lambda}_b^0 \to \overline{\Lambda}\gamma$,$\alpha_\gamma = \alpha_\gamma^+ = -1$ and $\alpha_\Lambda = \alpha_\Lambda^+$ (Eq. 5.17). Notice that the statistics these two samples present are similar to the ones used in the tight selection, for which the angular fit strategy has already been validated. The angular background

	$\Lambda_b^0 \to \Lambda\gamma$	$\overline{\Lambda}_b^0 \to \overline{\Lambda}\gamma$
μ (MeV/c^2)	5607 ± 16	5602 ± 20
τ	-0.00085 ± 0.00004	-0.00081 ± 0.00004
N_{sig}	252 ± 34	227 ± 33
N_{comb}	3363 ± 69	3062 ± 66
$N_{\Lambda_b^0 \to \Lambda\eta}$	35 ± 20	31 ± 19
χ^2/ndof	46.87/34	43.87/34

Table 5.20: Parameters of the invariant mass fit to data candidates for $\Lambda_b^0 \to \Lambda\gamma$ and $\overline{\Lambda}_b^0 \to \overline{\Lambda}\gamma$.

	$\Lambda_b^0 \to \Lambda\gamma$	$\overline{\Lambda}_b^0 \to \overline{\Lambda}\gamma$
$N_{sig}^{2.5\sigma}$	233 ± 32	210 ± 30
$N_{comb}^{2.5\sigma}$	763 ± 16	701 ± 16
$N_{\Lambda_b^0 \to \Lambda\eta}^{2.5\sigma}$	4 ± 2	4 ± 2

Table 5.21: Signal and background yields of a reduced invariant mass region (2.5σ) numerically computed using the fitted PDFs, for $\Lambda_b^0 \to \Lambda\gamma$ and $\overline{\Lambda}_b^0 \to \overline{\Lambda}\gamma$ candidates.

shape is extracted from the data invariant mass side bands. The same acceptance and background distributions are used for both Λ_b^0 and $\overline{\Lambda}_b^0$ decays, and are obtained from the combined sample. In any case, Fig. 5.27 shows the good agreement between the acceptance and background shapes obtained using the Λ_b^0, $\overline{\Lambda}_b^0$ and the combined samples.

The same model is used to fit the generated pseudo-datasets, with free α_γ^- and α_γ^+. The results of the dispersion and pull distributions for α_γ^- and α_γ^+ are shown in Fig. 5.28, and the results of the Gaussian fits in Table 5.22. Similar aspects to the ones observed in the combined pseudo-experiments are observed. The pull distribution having a mean and a standard deviation compatible with $\mu = 0$ and $\sigma = 1$, indicate no clear bias and a good error coverage is found for both decay channels.

	Dispersion distribution		Pull distribution	
	μ	σ	μ	σ
$\alpha_\gamma^- = 1$	0.972 ± 0.006	0.362 ± 0.007	0.026 ± 0.020	1.046 ± 0.011
$\alpha_\gamma^+ =$ -1	0.971 ± 0.005	0.378 ± 0.004	-0.016 ± 0.020	1.020 ± 0.011

Table 5.22: Fitted mean and standard deviation of the α_γ^- and α_γ^+ dispersion and pull distribution. The α_γ^+ parameter is taken as -α_γ^+, to have the same sign as α_γ^-.

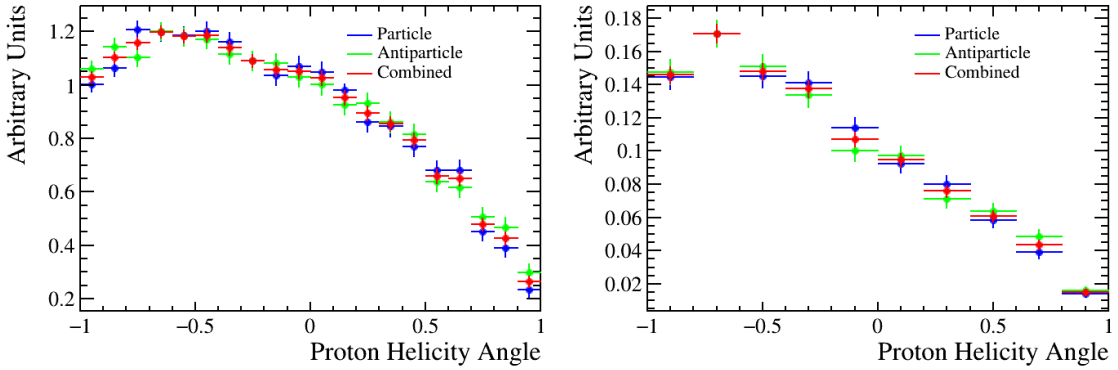

(a) (b)

Figure 5.27: (a) Acceptance and (b) angular background shapes obtained from the (blue) $\Lambda_b^0 \to \Lambda\gamma$, (red) $\overline{\Lambda}_b^0 \to \overline{\Lambda}\gamma$ and (green) combined samples (loose configuration).

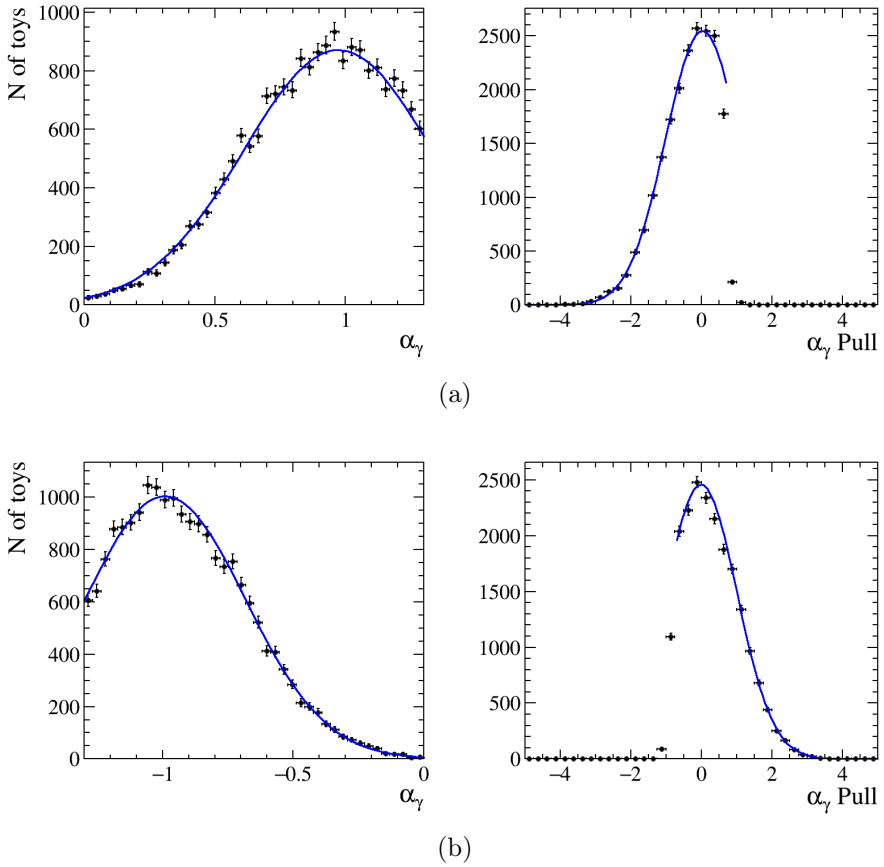

(a)

(b)

Figure 5.28: Dispersion (left) and pull distribution (right) for α_γ fitted values of the pseudo-experiment study. The pseudo-datasets have been generated with signal and background yields matching those of (a) $\Lambda_b^0 \to \Lambda\gamma$ and (b) $\overline{\Lambda}_b^0 \to \overline{\Lambda}\gamma$ decays. A Gaussian fit is superimposed.

5.7 Uncertainties

Two types of uncertainties are considered in the measurement of the photon polarization in $\Lambda_b^0 \to \Lambda\gamma$ decays. Statistical uncertainties are extracted from the angular fit to data candidates, and are presented in Sec. 5.8. A good proxy for their magnitude, is obtained through the sensitivity studies presented in Sec. 5.6. Systematic uncertainties, in opposition, can be estimated before performing the angular fit to the data samples.

In this Section, systematic uncertainties arising from different sources are studied and estimated via the usage of pseudo-datasets (20000). Differences on the α_γ dispersion distributions between the nominal pseudo-datasets, generated and fit with the nominal model, and alternative pseudo-datasets, generated with an alternative model and fit with the nominal model are used to evaluate these systematic effects. The dispersion and pull distributions for the alternative models can be found in App. A.7. The nominal pseudo-datasets distributions are shown in Sec. 5.6.

Two different methods to compute the value of the systematic uncertainties are used depending on the source of the systematic. Systematic uncertainties that alter the model itself, such as using different order polynomials to fit the acceptance shape, are computed as the difference between mean values of the photon polarization dispersion, presented in Eq. 5.19.

$$\sigma_{\text{syst.}}^{\text{alt}} = |\mu_{\text{alt}} - \mu_{\text{nominal}}| \tag{5.19}$$

While systematic uncertainties arising from variating the values of the parameters of the given model within the statistical precision, such as variating the acceptance shape parameters using the covariance matrix of the fit performed to extract them, are computed as the squared difference of the width of the parameter dispersion, shown in Eq. 5.20.

$$\sigma_{\text{syst.}}^{\text{var}} = \sqrt{|\sigma_{\text{alt}}^2 - \sigma_{\text{nominal}}^2|} \tag{5.20}$$

5.7.1 Acceptance and background

The nominal acceptance and angular background shapes are characterized using a fourth order polynomial, chosen by studying different polynomials and selecting the one that best describes the distribution, with χ^2 as basis. Therefore, the systematic uncertainty derived from this choice is extracted using third and fifth order polynomials as alternative models, using Eq. 5.19. An additional systematic is assigned given that both shapes are extracted using a fit to statistically limited samples. A variating model is generated by fluctuating each parameter according to the covariance matrix. This systematic computation uses Eq. 5.20. Lastly, a final systematic is assessed for the acceptance shape, taking into account the possible miss-estimation of the kinematic weights used to correct the simulated samples. Conservatively an alternative model, extracted by not applying the kinematic weights, is used for this purpose. The values of the fitted dispersion distribution parameters, μ and σ, are

	Loose		Tight	
	μ	σ	μ	σ
Nominal	0.991	0.270	0.974	0.351
Fluctuation	0.991	0.273	0.981	0.353
$\sigma_{\rm acc}^{\rm var}$	**0.040**		**0.038**	
Alternative Pol(3)	0.996	0.274	0.968	0.344
$\sigma_{\rm acc}^{\rm alt}$	**0.005**		**0.006**	
Alternative Pol(5)	0.992	0.271	0.985	0.360
$\sigma_{\rm acc}^{\rm alt}$	**0.001**		**0.011**	
W/o Kin. weights	0.954	0.258	0.939	0.346
$\sigma_{\rm acc}^{\rm alt}$	**0.037**		**0.035**	

Table 5.23: Mean and width of the α_γ dispersion obtained in the pseudo-experiment studies, and the systematic uncertainties associated to the modeling of the acceptance.

	Loose		Tight	
	μ	σ	μ	σ
Nominal	0.991	0.270	0.974	0.351
Fluctuation	0.983	0.293	0.967	0.381
$\sigma_{\rm bkg}^{\rm var}$	**0.114**		**0.148**	
Alternative Pol(3)	1.005	0.271	0.956	0.351
$\sigma_{\rm bkg}^{\rm alt}$	**0.014**		**0.018**	
Alternative Pol(5)	0.994	0.272	0.951	0.351
$\sigma_{\rm bkg}^{\rm alt}$	**0.003**		**0.023**	

Table 5.24: Mean and width of the α_γ dispersion obtained in the pseudo-experiment studies, and the systematic uncertainties associated to the modeling of the background distribution.

shown in Table 5.23 and Table 5.24 along the corresponding systematic uncertainties for the acceptance and angular background shape, respectively.

5.7.2 Extraction of the yields

The signal and background yields extracted in Sec. 5.4 are used to construct the faction of signal candidates, f, which is Gaussian constrained in the angular fit. Therefore, the possible miss-estimation of these yields has a direct impact in the value of the photon polarization.

In particular, a possible miss-estimation of the fraction of candidates may arise from fixing the width of the Gaussian core of the double-sided Crystal Ball. An alternative mass fit, without fixing the σ to the simulated samples is performed (the other parameters except μ remain fixed). This provides $\sigma = 121 \pm 19$ (80 ± 12) MeV/c^2 for the loose (tight) selection and a signal yield in the reduced mass window of $N_{sig}^{2.5\sigma} = 488$ (174), compared to the nominal yield of $N_{sig}^{2.5\sigma} = 444$ (186), i.e. a 10% variation of the signal yield.

	Loose		Tight	
	μ	σ	μ	σ
Nominal	0.991	0.270	0.974	0.351
Increased signal	1.026	0.270	1.028	0.352
$\sigma^{\text{alt}}_{\text{bias +}}$	**0.035**		**0.054**	
Decreased signal	0.960	0.274	0.930	0.349
$\sigma^{\text{alt}}_{\text{bias -}}$	**0.031**		**0.044**	

Table 5.25: Mean and width of the α_γ dispersion obtained in the pseudo-experiment studies, and the systematic uncertainties associated to the alternative signal and background yields models.

	Loose		Tight	
	μ	σ	μ	σ
Nominal	0.991	0.270	0.974	0.351
Fluctuation	0.995	0.269	0.981	0.354
$\sigma^{\text{var}}_{\alpha_\Lambda}$	**0.023**		**0.046**	

Table 5.26: Mean and width of the α_γ dispersion obtained in the pseudo-experiment studies, and the systematic uncertainty associated to the fluctuation of the α_Λ decay parameter.

In order to also account for other residual effects arising from small contributions of other partially reconstructed backgrounds, including $\Lambda_b^0 \to \Lambda\eta$ candidates, two alternative models are considered. In the first model the signal yield is reduced by a 10%, and these candidates are assigned to the background, while in the second model the signal yield is increased by a 10%, and these candidates are extracted from the background. This systematic effect is computed using Eq. 5.19, as the effects arise from the difference in the fraction of candidates Gaussian constrained used in the generating and fitting processes but also in the decrease (increase) of sensitivity due to the lower (higher) amount of signal yield. The results of these systematic studies are presented in Table. 5.25. The final systematic uncertainty is taken as the higher of both alternative models.

5.7.3 Λ weak decay parameter

The value of the parameter $\alpha_\Lambda = 0.754 \pm 004$, averaged for $\Lambda_b^0 \to \Lambda\gamma$ and $\overline{\Lambda}_b^0 \to \overline{\Lambda}\gamma$, is known with high precision. In the angular fit, the value of this parameter is fixed. To compute an associated systematic uncertainty, pseudo-datasets are generated using an alternative model on which the α_Λ is fluctuated using its uncertainty. The results are shown in Table 5.26 and Eq. 5.20 is used to derive the corresponding systematic.

5.7.4 Tagged measurements

Similarly to what is presented for tight and loose configurations, systematic uncertainties from the same sources are estimated for $\Lambda_b^0 \to \Lambda\gamma$ and $\overline{\Lambda}_b^0 \to \overline{\Lambda}\gamma$ decays

	α_γ^-		$-\alpha_\gamma^+$	
	μ	σ	μ	σ
Nominal	0.972	0.362	0.971	0.378
Fluctuation	0.972	0.360	0.968	0.381
$\sigma^{\text{var}}_{\text{syst.}}$	**0.038**		**0.047**	
Alternative Pol(3)	0.949	0.356	0.947	0.370
$\sigma^{\text{alt}}_{\text{syst.}}$	**0.023**		**0.024**	
Alternative Pol(5)	0.981	0.367	0.967	0.378
$\sigma^{\text{alt}}_{\text{syst.}}$	**0.009**		**0.004**	
$\Lambda_b^0/\overline{\Lambda}_b^0$ model	0.974	0.356	0.969	0.383
$\sigma^{\text{alt}}_{\text{syst.}}$	**0.002**		**0.002**	

Table 5.27: Mean and width of the α_γ^+ and α_γ^- dispersion obtained in the pseudo-experiment studies, and the systematic uncertainty associated to the choice of the acceptance model. The α_γ^+ parameter is taken as $-\alpha_\gamma^+$, to have the same sign as α_γ^-.

	α_γ^-		$-\alpha_\gamma^+$	
	μ	σ	μ	σ
Nominal	0.972	0.362	0.971	0.378
Fluctuation	0.973	0.384	0.962	0.393
$\sigma^{\text{var}}_{\text{syst.}}$	**0.128**		**0.107**	
Alternative Pol(3)	0.990	0.363	0.986	0.382
$\sigma^{\text{alt}}_{\text{syst.}}$	**0.018**		**0.015**	
Alternative Pol(5)	0.974	0.362	0.965	0.377
$\sigma^{\text{alt}}_{\text{syst.}}$	**0.002**		**0.006**	
$\Lambda_b^0/\overline{\Lambda}_b^0$ model	1.097	0.367	0.866	0.379
$\sigma^{\text{alt}}_{\text{syst.}}$	**0.125**		**0.105**	

Table 5.28: Mean and width of the α_γ^+ and α_γ^- dispersion obtained in the pseudo-experiment studies, and the systematic uncertainty associated to the choice of the background model. The α_γ^+ parameter is taken as $-\alpha_\gamma^+$, to have the same sign as α_γ^-.

via the usage of pseudo-experiments. An additional alternative systematic for the acceptance and background angular shapes is considered due to the usage of the combined sample as nominal to model these distributions in the angular fit. To account for possible effects arising from this choice, the acceptance and background angular distributions are obtained from the $\Lambda_b^0 \to \Lambda\gamma$ and $\overline{\Lambda}_b^0 \to \overline{\Lambda}\gamma$ samples separately and used as alternative models. The value of the fitted dispersion distributions used to compute systematic uncertainties are presented in Table 5.27 for the acceptance, Table 5.28 for the background shape, Table 5.29 for the increase and decrease of the signal and background yields and Table 5.30 for the Λ weak decay parameter.

5.7.5 Results

A summary of the systematic uncertainties for each configuration, loose and tight, is presented in Table. 5.31. Individual contributions are added in quadrature to obtain

	α_γ^-		$-\alpha_\gamma^+$	
	μ	σ	μ	σ
Nominal	0.972	0.362	0.971	0.378
Increased signal	1.007	0.364	1.006	0.374
$\sigma^{\text{alt}}_{\text{bias +}}$	**0.035**		**0.035**	
Decreased signal	0.938	0.360	0.936	0.378
$\sigma^{\text{alt}}_{\text{bias -}}$	**0.034**		**0.035**	

Table 5.29: Mean and width of the α_γ^+ and α_γ^- dispersion obtained in the pseudo-experiment studies, and the systematic uncertainties associated to the alternative signal and background yields models.

	α_γ^-		$-\alpha_\gamma^+$	
	μ	σ	μ	σ
Nominal	0.972	0.362	0.971	0.378
Fluctuation	0.985	0.370	0.976	0.383
$\sigma^{\text{var}}_{\alpha_\Lambda}$	**0.076**		**0.062**	

Table 5.30: Mean and width of the α_γ^+ and α_γ^- dispersion obtained in the pseudo-experiment studies, and the systematic uncertainty associated to the fluctuation of the α_Λ decay parameter.

the total uncertainty.

In Table 5.32 the summary of the systematic uncertainties for $\Lambda_b^0 \to \Lambda\gamma$ and $\overline{\Lambda}_b^0 \to \overline{\Lambda}\gamma$ decays is presented. As the same nominal model is used for describing the acceptance and background shapes for α_γ^- and α_γ^+, the systematic uncertainties derived for the limited size of the samples is considered to be 100% correlated. The rest of the studied systematic effects are assumed to be uncorrelated and their associated uncertainty is added in quadrature.

Systematic source		$\sigma(\alpha_\gamma)$	
		Loose	Tight
Acceptance	MC limited size	0.040	0.038
	Model	0.005	0.011
	Kin. weights	0.037	0.035
Background	Data limited size	0.114	0.148
	Model	0.014	0.023
Yields		0.035	0.054
α_Λ		0.023	0.046
Total		0.134	0.174

Table 5.31: Summary of the systematic uncertainties in the measurement of the photon polarization for $\Lambda_b^0 \to \Lambda\gamma$ decays with Run 2 data.

Systematic source		α_γ^- (part)	α_γ^+ (anti)
Acceptance	MC limited size	0.038	0.047
	Model	0.023	0.024
Background	Data limited size	0.128	0.107
	Model	0.125	0.105
Yields		0.035	0.035
α_Λ		0.076	0.062
Total correlated		0.133	0.117
Total uncorrelated		0.152	0.129
Total		0.202	0.174

Table 5.32: Summary of the systematic uncertainties in the measurement of the photon polarization for $\Lambda_b^0 \to \Lambda\gamma$ and $\overline{\Lambda}_b^0 \to \overline{\Lambda}\gamma$ (α_γ^- and α_γ^+) decays with Run 2 data.

5.8 Results

The results of the photon polarization in $\Lambda_b^0 \to \Lambda\gamma$ decays, for both configurations and for the tagged measurements, are presented in this Section. The photon polarization, α_γ, is obtained from a fit to the proton helicity distribution of selected data candidates, using the angular PDF described and validated in detail in Sec. 5.6. The acceptance shape is fixed to the parametrization obtained from the simulated samples, presented in Sec. 5.5. The background shape is extracted from the data candidates present in the side bands, described in Sec. 5.6.2. The signal and background yields are Gaussian constrained to the values extracted from the invariant mass fit, in the reduced mass window, presented in Sec. 5.4. Only α_γ is allowed to vary in the fit to the data, while the α_Λ parameter is fixed to its corresponding value, Eq. 5.18 for the combined case and Eq. 5.16 and Eq. 5.17 for the tagged cases.

It is worth noting that due to statistical fluctuations, the measured value of the α_γ parameter, or part of its confidence interval, may fall into a non-physical range, defined by $|\alpha_\gamma| > 1$, arising from its definition (Eq. 3.8). The Feldman-Cousins (FC) approach [102] is used to provide a measurement within the α_γ physical range considering different confidence intervals. Lastly, to avoid any potential analyst biases, the extraction of the results for the tight and loose configurations are examined after the full strategy has been reviewed and validated. The photon polarization measurements for the tagged cases are done as the final step.

Blinded fit

An unbinned maximum likelihood fit to the proton helicity distribution of data candidates is performed. The value of the photon polarization extracted from the angular fit to $\Lambda_b^0 \to \Lambda\gamma$ data candidates is blinded, whereas the value of its uncertainty and the fraction of candidates, f, are obtained. This enables to obtain the final statistical uncertainty, without unblinding the central value.

The proton helicity distribution for fully selected data candidates is shown in

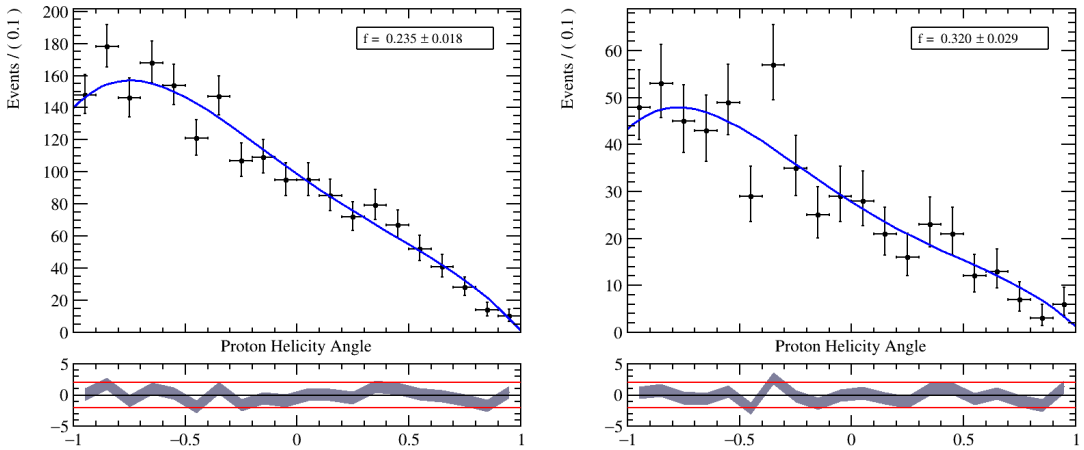

(a) (b)

Figure 5.29: Blinded fit of the cosine of the proton helicity angle for (a) loose and (b) tight selections. The candidate fraction is detailed in the legend and the blinded α_γ values in Eq. 5.21 and Eq. 5.22

Fig. 5.29, for both configurations. The fitted angular PDF is overlaid, showing a good description of the data, to further avoid possible analyst biases at this stage, the separate PDF contributions from the signal and background distributions are not represented. The photon polarization is found to be

$$\alpha_\gamma^{loose} = XXX(\text{blinded}) \pm 0.23 \tag{5.21}$$

$$\alpha_\gamma^{tight} = XXX(\text{blinded}) \pm 0.36 \tag{5.22}$$

where the central value of α_γ is blinded and the uncertainty is statistical only. The signal fraction obtained from the angular fit, shown in Fig. 5.29, is in good agreement with that obtained from the mass fit in Sec. 5.4. The loose configuration has better statistical sensitivity, as expected. Given that its associated systematical uncertainty is also lower, the the result of the loose samples is taken as the nominal measurement of this study.

Cross-check

A cross-check is performed before unblinding, by comparing the compatibility between the photon polarization value obtained with the loose and tight configurations. The procedure takes into account the correlations between both configurations and does not unblind the values themselves. The compatibility is evaluated as the difference between the two values, namely $\Delta = \alpha_\gamma^{Loose} - \alpha_\gamma^{Tight}$ in units of the expected uncertainty on this quantity. The statistical uncertainties for both configurations are taken into account along the overlap of signal candidates, 42%, used as the correlation between the two results. An uncertainty in Δ of $\delta\Delta = 0.35$ is obtained for their difference. The criteria used to validate the cross-check considers whether or not the Δ value is compatible with 0 at a maximum of 3σ. The value of Δ is found to be $\Delta = 0.23$, showing a good compatibility between the loose and tight configurations, and therefore validating the extraction of α_γ.

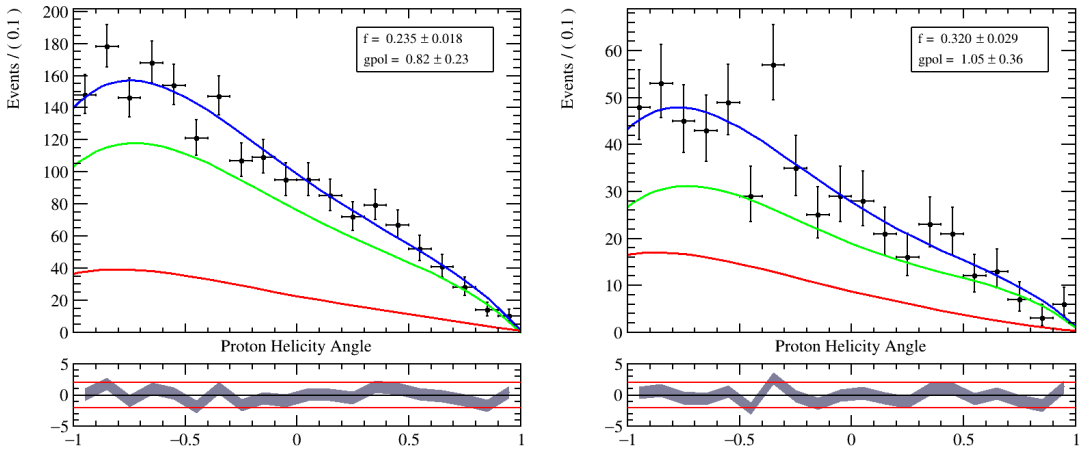

(a) (b)

Figure 5.30: Unblinded fit of the cosine of the proton helicity angle for (a) loose and (b) tight selections. The total angular PDF, and the signal and combinatorial background contributions are shown blue, red and green lines, respectively.

Unblinded fit

The photon polarization in $\Lambda_b^0 \to \Lambda\gamma$ events for both configurations is found to be

$$\alpha_\gamma^{loose} = 0.82 \pm 0.23, \tag{5.23}$$
$$\alpha_\gamma^{tight} = 1.05 \pm 0.36, \tag{5.24}$$

where the uncertainty is statistical only as given by the unbinned maximum likelihood fit shown in Fig. 5.30.

The fitted $\cos\theta_p$ distribution for $\Lambda_b^0 \to \Lambda\gamma$ and $\overline{\Lambda}_b^0 \to \overline{\Lambda}\gamma$ data candidates is shown in Fig. 5.31 and the photon polarization in the specific *CP* modes is found to be

$$\alpha_\gamma^{\Lambda_b^0 \to \Lambda\gamma} = \alpha_\gamma^- = 1.26 \pm 0.42 \tag{5.25}$$
$$\alpha_\gamma^{\overline{\Lambda}_b^0 \to \overline{\Lambda}\gamma} = \alpha_\gamma^+ = -0.55 \pm 0.32, \tag{5.26}$$

where the uncertainty is statistical only as given by the unbinned maximum likelihood fit.

For completeness, the log-likelihood profiles of each maximum likelihood fit are presented in App. A.8. Studies using pseudo-experiments show that the measured value of α_γ^- is affected by a 5% bias and a 13% over-coverage given by the close proximity of the observed value to the mathematical limit given by the PDF.

5.8.1 Feldman-Cousins

The Feldman-Cousins approach [102] is used to extract the measurement of the photon polarization within physical limits $[-1, 1]$. For each measurement, the fit

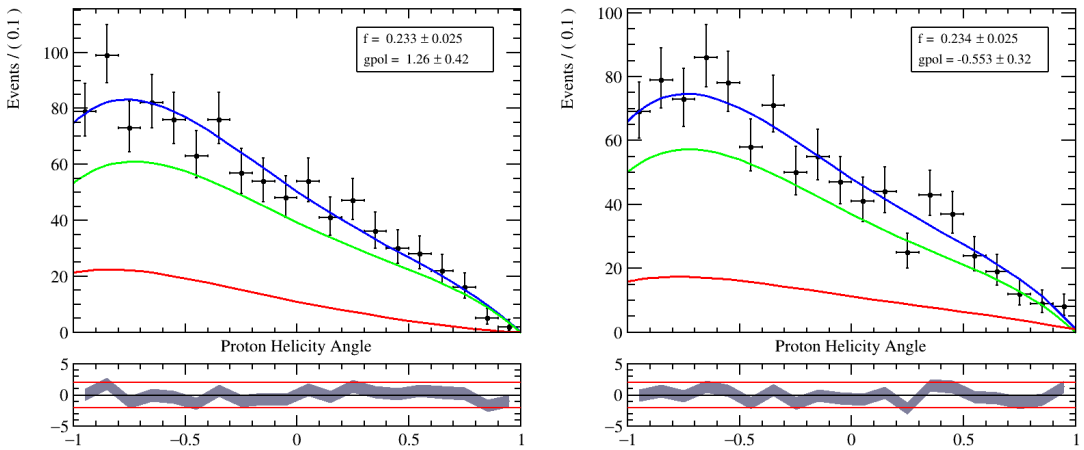

(a) (b)

Figure 5.31: Unblinded fit of the cosine of the proton helicity angle distribution for (a) $\Lambda_b^0 \to \Lambda\gamma$ and (b) $\overline{\Lambda}_b^0 \to \overline{\Lambda}\gamma$ candidates. The total angular PDF, and the signal and combinatorial background contributions are shown blue, red and green lines, respectively.

value and the relation between true and measured values (extracted using pseudo-experiments) are used to create the Neyman confidence belts. These are produced taking into account the statistical and systematical uncertainties, for a given confidence interval (e.g. 1σ) and are shown in App. A.8.

The nominal measurement using the loose configuration, is presented in Eq. 5.27 and Fig. A.35.

$$\alpha_\gamma = 0.82^{+0.17}_{-0.26}\ (\text{stat.})\ ^{+0.04}_{-0.13}\ (\text{syst.}) \tag{5.27}$$

The photon polarization measurements for tagged $\Lambda_b^0 \to \Lambda\gamma$ and $\overline{\Lambda}_b^0 \to \overline{\Lambda}\gamma$ decays are presented in Eqs. 5.28, 5.29 and Fig. A.36.

$$\alpha_\gamma^- > 0.56(0.44) \text{ at } 90\% \ (95\%) \text{ C.L.}, \tag{5.28}$$

$$\alpha_\gamma^+ = -0.56^{+0.36}_{-0.33}\ (\text{stat.})\ ^{+0.16}_{-0.09}\ (\text{syst.}) \tag{5.29}$$

The photon polarization measurement for the combined and $\overline{\Lambda}_b^0 \to \overline{\Lambda}\gamma$ samples are double-sided confidence intervals (1σ) where the statistical and systematic uncertainties are shown separately. The tagged $\Lambda_b^0 \to \Lambda\gamma$ measurement is a one-sided confidence interval, commonly provided for 90% and 95% confidence levels (C.L.), shown in Fig. A.37.

The α_γ measurement in the combined sample is used to constrain the real and imaginary parts of the electromagnetic dipole WCs, namely $\mathcal{C}_7^{(\text{eff})}$ and $\mathcal{C}_{7,}^{\prime(\text{eff})}$ using the effective Hamiltonian description in $b \to s\gamma$ transitions, presented in Chapter 3. The leading order expression of α_γ in terms of Wilson coefficients, presented in Eq. 3.8, is used within the `flavio` package [103] to this end. The result of the measurement (green) enables the experimental exclusion of two solutions with large real values of

$\mathcal{C}_7^{(\mathrm{eff})}$ and $\mathcal{C}_{7,}^{\prime(\mathrm{eff})}$ which, although phenomenologically unfavored, were experimentally allowed by all previous measurements, as shown in Fig. 5.32 (top). In Fig. 5.32 (bottom), the measurement of the photon polarization causes a circular constraint, albeit not dominant, compatible with previous measurements.

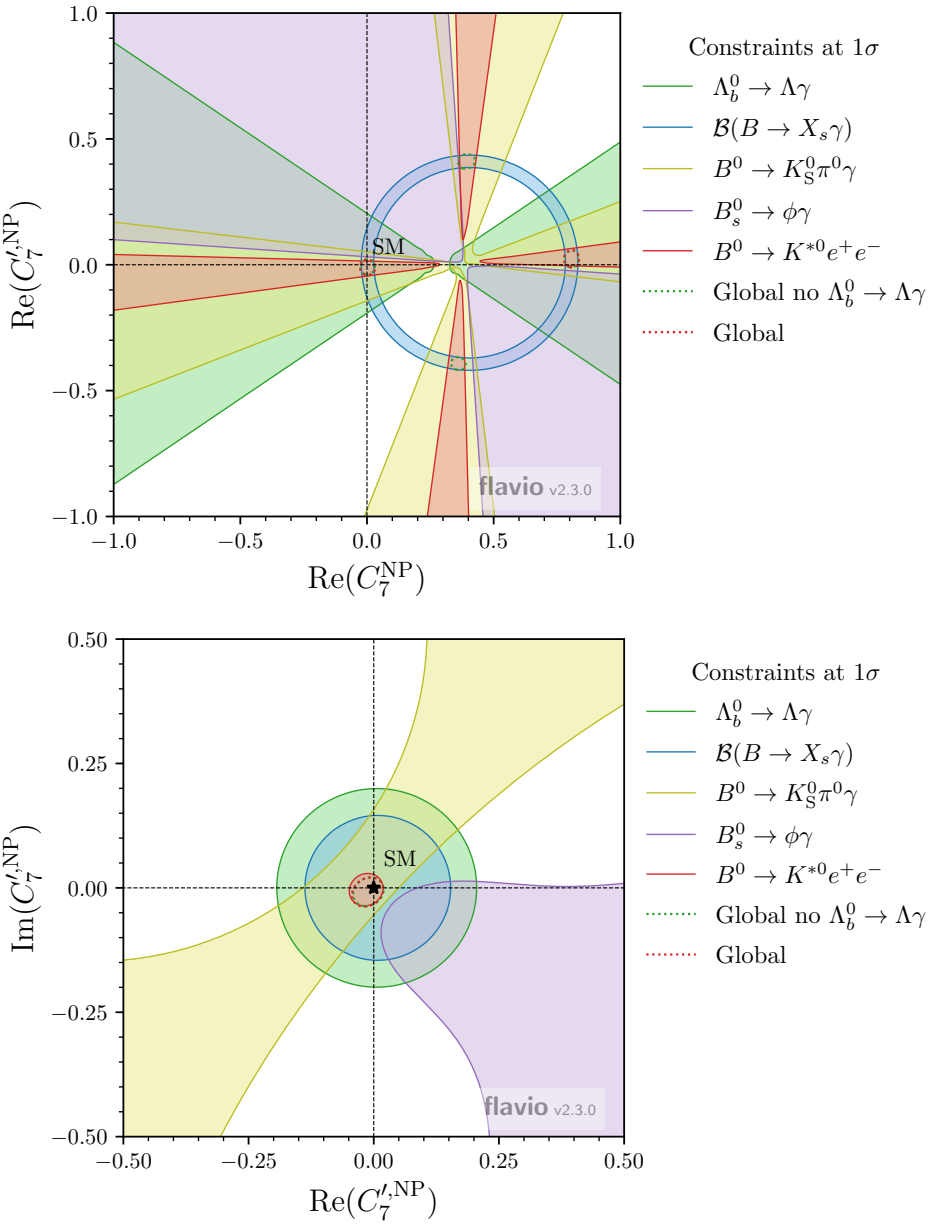

Figure 5.32: Constraints at the 1σ level on the new physics contributions to the (top) left- and right-handed Wilson coefficients, $\mathcal{C}_7^{(\mathrm{eff})}$ and $\mathcal{C}_{7,}^{\prime(\mathrm{eff})}$ and on the (bottom) real and imaginary parts of $\mathcal{C}_{7.}^{\prime(\mathrm{eff})}$ In the latter, the $\mathcal{C}_7^{(\mathrm{eff})}$ coefficient is fixed to its SM value. The measurements of the inclusive branching fraction, $\mathcal{B}(B \to X_s\gamma)$, and the $B^0 \to K_S^0\pi^0\gamma$ mixing-induced CP asymmetry by the Belle and BaBar experiments [50, 75] are shown in blue and yellow, respectively, the $B_s^0 \to \phi\gamma$ and $B^0 \to K^{*0}e^+e^-$ measurements by the LHCb experiment [53, 54] in purple and red, respectively, and the α_γ measurement presented in green. The global fit is shown in dashed red (green) lines including (excluding) this measurement.

5.9 Conclusions

In this Chapter the photon polarization of a radiative b-baryon transition has been measured for the first time. The photon polarization for $\Lambda_b^0 \to \Lambda\gamma$ decays has been measured by exploiting the angular structure of the weak Λ decay to a proton and a pion, enabling the direct extraction of the observable via a fit to the proton helicity angular distribution. Two selection configurations are used throughout, while only the better performant is ultimately used for the measurement.

The measurement is found to be compatible with the SM prediction at the level of one standard deviation (1σ). The result is in agreement with previous measurements using b-meson decays [50, 53, 54, 75], nevertheless it can be used to place new constraints to contributions from right-handed current arising from NP models. In addition, differences in α_γ of Λ_b^0 and $\overline{\Lambda}_b^0$ decays are studied and found to be compatible at the level of one standard deviation to CP symmetry.

The current measurements are dominated by the statistical uncertainty. Significant improvements are thus expected with the data that will be recorded by LHCb during Run 3 of the LHC and beyond. The dominant systematic effect arises from the limited number of candidates in the Λ_b^0 invariant mass side bands after the selection, from which the angular shape of the background is extracted. This sample will also scale with the addition of more data such that the systematic will be reduced and is not expected to be a limiting factor. Other systematic uncertainties can be reduced with the generation of larger simulation samples and more detailed studies of the data and simulation agreement. Consequently, these measurements are not expected to be limited by systematic uncertainties in the near future. However, an improvement on the measurement of the branching ratio of the main physical background, namely $\Lambda_b^0 \to \Lambda\eta$, would be beneficial to have a better control over its contamination.

6 Conclusions and future prospects

This document presents my work done in the scope of beauty and strange rare decays in the LHCb experiment. Primarily, by preforming an initial study of the $K^0_S \to \pi^+\pi^-e^+e^-$ decay mode inside the LHCb experiment to further experimentally understand the K^0_S to four lepton decays. And secondarily, in the form of the first measurement of the photon polarization in radiative baryon b-decays using the $\Lambda^0_b \to \Lambda\gamma$ decay mode. Both studies are of relevance since Flavor Changing Neutral Currents are forbidden at tree level in the SM. Therefore requiring the presence of loop diagrams, making both these transition very sensitive to possible New Physics particles entering the loops.

Rare strange decays are FCNC suppressed by the Standard Model, in particular $K^0_S \to \ell^+\ell^-\ell^+\ell^-$ decays have never been observed and are of particular interest. In the scope of this thesis a much more abundant decay, $K^0_S \to \pi^+\pi^-e^+e^-$, with a similar topology is studied using 2016 and 2017 data from the LHCb experiment as a first step towards these much rarer decay modes. The presence of K^0_S mesons, mostly decaying outside the most precise LHCb sub-detector, and very low transverse momentum electrons, losing energy in the form of Bremsstrahlung photons, makes this decay very challenging to reconstruct and select by the detector. A selection of $K^0_S \to \pi^+\pi^-e^+e^-$ candidates along an maximum likelihood invariant mass fit are performed to extract the yield of this decay mode, obtaining

$$N_{sig} = 170 \pm 20$$

data candidates, being the first indication of this decay mode by the LHCb detector. An expected signal yield is computed using Monte Carlo simulated samples and several efficiency corrections are applied to correct for possible discrepancies between the data and simulation samples. Nevertheless, an expected yield of

$$N^{exp}_{K^0_S \to \pi^+\pi^-e^+e^-} \sim 1000 \pm 225$$

is found to be incompatible with the experimental one. Several aspects may factor in this discrepancy, a different strategy, using a normalization channel, may be worth considering for future studies along with the increase of statistics present in the simulation samples. A more profound selection strategy, using a multivariate classifier, along using the full Run 2 data sample may also be worth considering to increase the signal yield.

The radiative mode, $\Lambda^0_b \to \Lambda\gamma$, only observed recently by the LHCb experiment, and the consequent Λ weak decay, $\Lambda \to p\pi^-$, are used to measure the photon

polarization using the data obtained by the LHCb experiment during Run 2. The proton angular distribution is exploited to directly extract the photon polarization of this $b \to s\gamma$ transition. A strategy is utilized for this purpose, $\Lambda_b^0 \to \Lambda\gamma$ candidates are selected, by expanding the work performed in the observation of the mode. Then, the yield of signal and background candidates is extracted using a maximum likelihood fit to the invariant mass of the Λ_b^0 candidates. The proton angular distributions of the signal and the background contributions are studied and controlled. A maximum likelihood invariant fit to the proton angular distribution, taking into account both the yields and shape of the different contributions, is performed to extract a value of the photon polarization. The Feldman-Cousins approach is then used to extract the value of the photon polarization within physical limits. Systematic uncertainties are studied to account for any potential effects of the assumptions made in the analysis. The same strategy is also applied to measure the photon polarization in tagged $\Lambda_b^0 \to \Lambda\gamma$ and $\overline{\Lambda}_b^0 \to \overline{\Lambda}\gamma$ decays. The photon polarization measurements for the combined sample of $\Lambda_b^0 \to \Lambda\gamma$ decays is found to be

$$\alpha_\gamma = 0.82^{+0.17}_{-0.26}\ (\text{stat.})\ ^{+0.04}_{-0.13}\ (\text{syst.})$$

and the measurements for tagged $\Lambda_b^0 \to \Lambda\gamma$ and $\overline{\Lambda}_b^0 \to \overline{\Lambda}\gamma$ samples are

$$\begin{aligned} \alpha_\gamma^- &> 0.56(0.44) \text{ at } 90\% \ (95\%) \text{ C.L.}, \\ \alpha_\gamma^+ &= -0.56^{+0.36}_{-0.33}\ (\text{stat.})\ ^{+0.16}_{-0.09}\ (\text{syst.}) \end{aligned}$$

The results of this analysis are compatible with the SM and statistically dominated, for both the combined and the tagged samples, but nevertheless allow to derive additional constrains to $\mathcal{C}_7^{(\text{eff})}$ and $\mathcal{C}_{7.}^{\prime(\text{eff})}$ The main systematic uncertainty arises from the shape of the proton angle distribution of the background candidates. Thus, both statistic and systematic uncertainties are expected to decrease with the addition of data from Run 3. This analysis also conforms the first steps towards the improvement of the branching fraction measurement of the $\Lambda_b^0 \to \Lambda\gamma$ decay mode, with the inclusion of Run 2 data from 2017 and 2018.

Both decays studied in this thesis are quite challenging, as they both include neutral and long lived particles. The results obtained expand the rare decays program at LHCb, but could also be further improved. In the case of the $K_S^0 \to \pi^+\pi^- e^+ e^-$ decay, further work is needed to understand this mode inside the LHCb, a more in-depth approach should be employed. The addition of more data and simulation samples, enabling for more validations, would also help solidify the overall analysis. The result of the photon polarization in $\Lambda_b^0 \to \Lambda\gamma$ could also be further improved by the addition of more data. While the constraint obtained by the measurement is not dominant in the literature, it is able to remove values previously allowed, showing the that measurements with b-baryon decays are complementary to those of b-meson decays. Finally, improving the measurements obtained from the tagged samples could open the door to perform tighter CPV tests to the photon polarization.

With the start of the Run 3 of the LHC and the corresponding Upgrade performed by the LHCb experiment high hopes can be set in the update of these two

studies. The LHCb detector increases its readout rate, to the 40 MHz LHC nominal one, along a luminosity increase of a factor five. The addition of a fully software trigger system, providing with a lot of flexibility at the low level selections, will also increase the raw signal yield for these channels by the end of Run 3. Together with the additional luminosity, to be recorded during this new period, the statistical sensitivity for the photon polarization measurement is expected to reach 14% during the first part of Run 3 and down to 4% at its end. The inclusion of downstream tracks to the current "long-tracks-only" analyses for these two modes is expected to happen during Run 3. This last addition would result in an increase of a factor five in the number of candidates, taken as an upper limit considering efficiencies similar to the current ones, as most Λ_b^0 and K_S^0 decay outside the VELO sub-detector. The increase in statistics would also enable the usage of the angular distributions of the $\Lambda_b^0 \to \Lambda\gamma$ decay mode to extract the polarization of Λ_b^0 baryons in the LHC, estimated to be very close to zero.

In particular for $\Lambda_b^0 \to \Lambda\gamma$ decays, work has also been done on developing a new set of HLT2 trigger selections, to be added to the Run 3 trigger system, using both long and downstream tracks. These new trigger lines are based on the strategy this thesis presents.

To summarize, this thesis presents the first ever measurement of the photon polarization in $b \to s\gamma$ transitions using a b-baryon decay, the $\Lambda_b^0 \to \Lambda\gamma$ mode. And also achieves the first observation of the $K_S^0 \to \pi^+\pi^- e^+ e^-$ inside the LHCb experiment and hints towards possible improvements to use this mode.

A Appendix

A.1 Redecay

The main basis the ReDecay technique is the re-use of the underlying event for different simulated candidates, meaning that the signal decay chain is generated anew for each simulated event, but the underlying process is not. This method generates possible correlations between simulated events. Thus possible effects need to be studied for each analysis and decay mode. Comparison plots between ReDecay [92] and full simulation $\Lambda_b^0 \to \Lambda\gamma$ samples, both generated for the 2017 year with the same conditions. Different variables used throughout the whole selection are displayed.

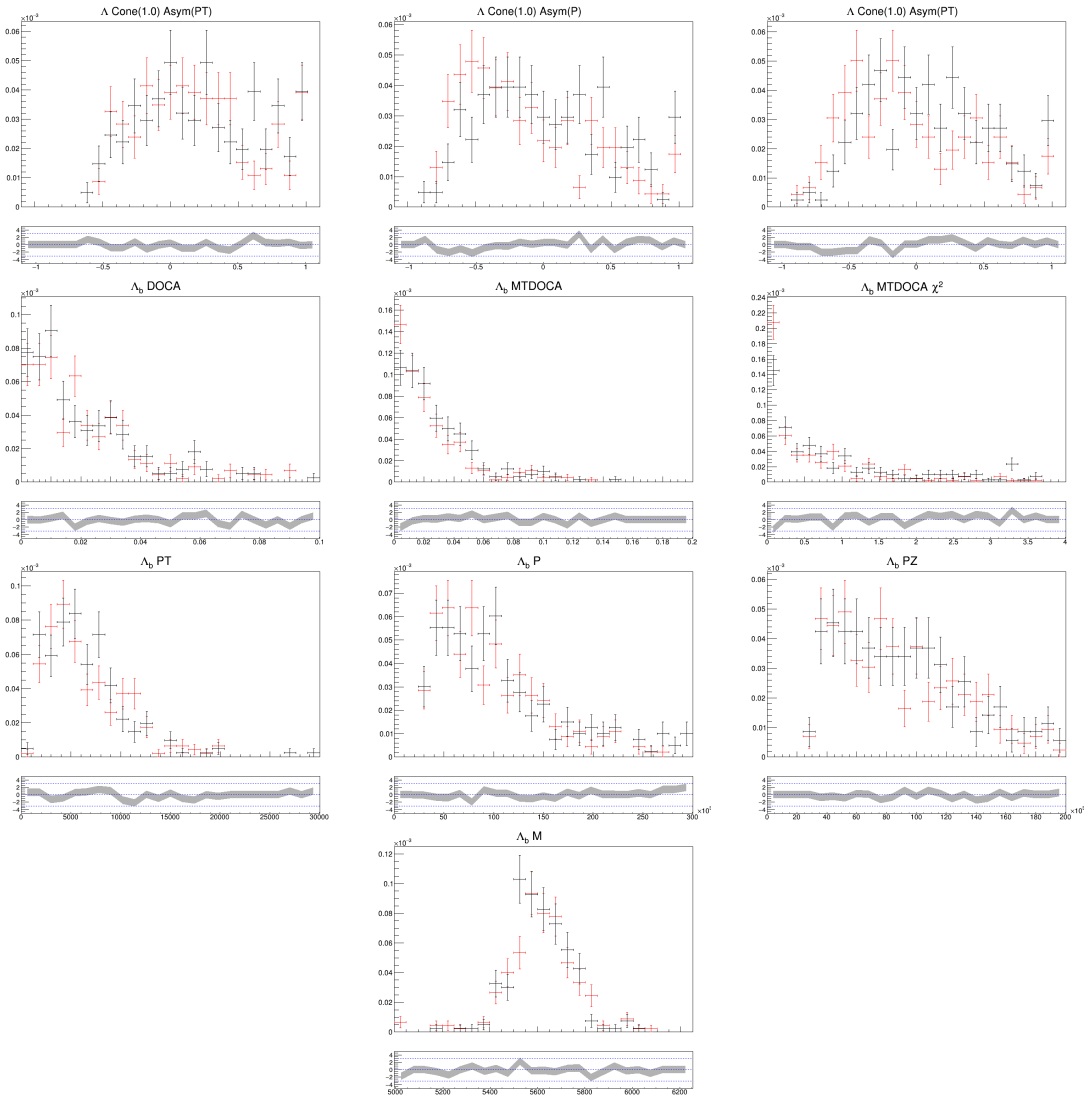

Figure A.1: Λ_b^0 baryon distributions comparison between redecay (red) and full simulation (black).

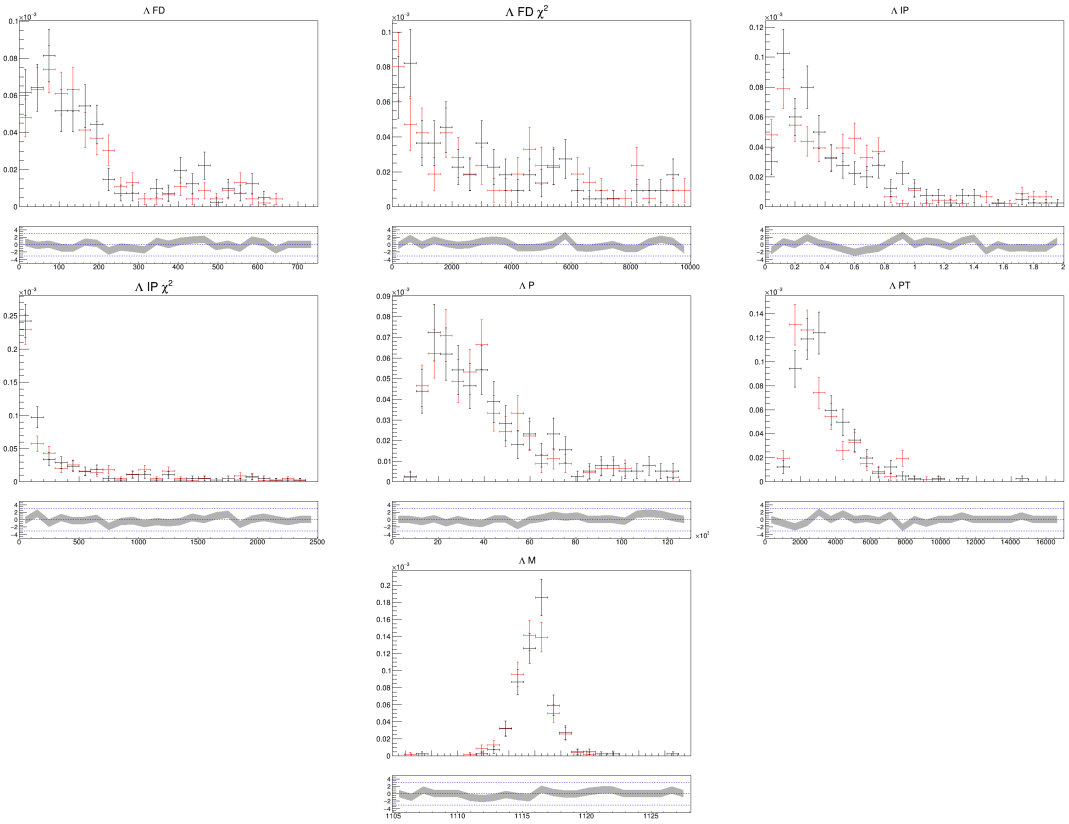

Figure A.2: Λ baryon distributions comparison between Redecay (red) and full simulation (black).

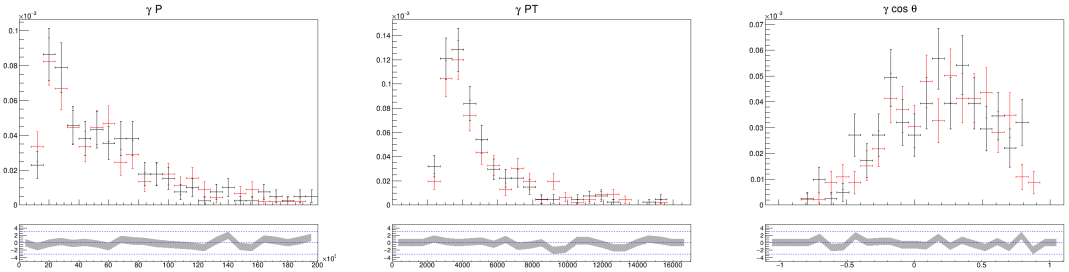

Figure A.3: Photon distributions comparison between Redecay (red) and full simulation (black).

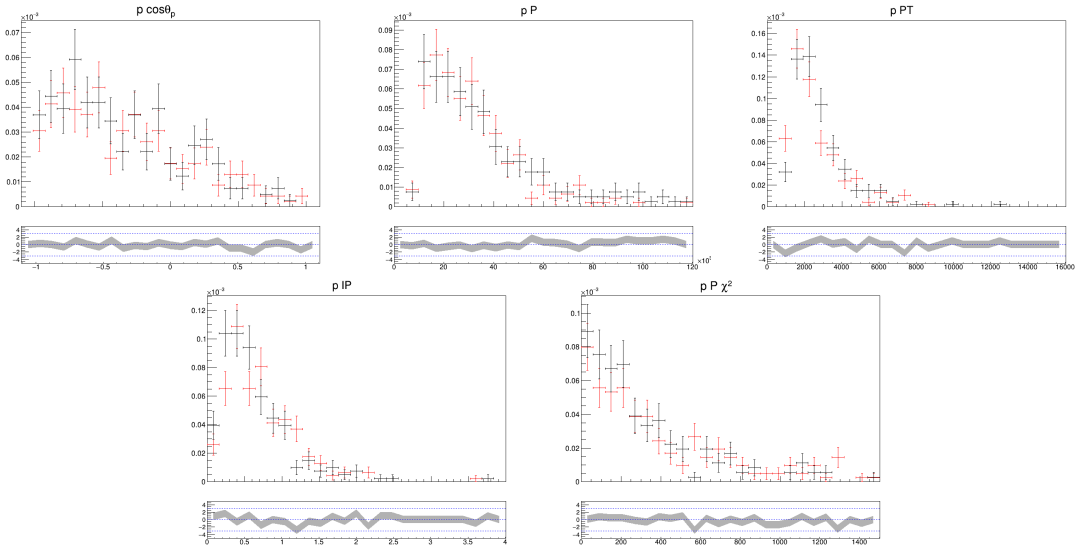

Figure A.4: Proton distributions comparison between Redecay (red) and full simulation (black).

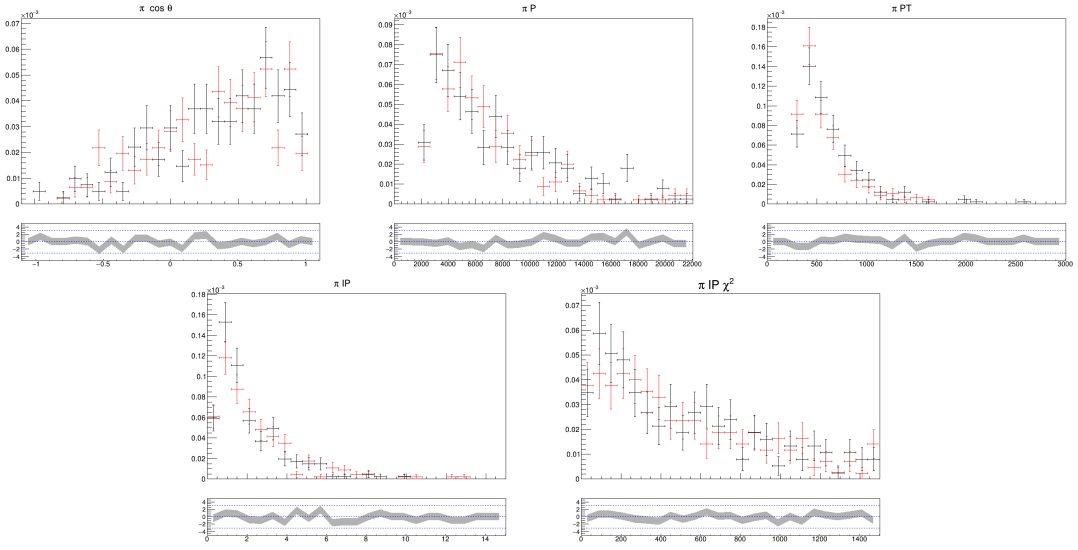

Figure A.5: Pion distributions comparison between Redecay (red) and full simulation (black).

A.2 Agreement between data and simulation

Comparison plots of $\Lambda_b^0 \to \Lambda J/\psi$ events, for sWeighted data, simulation and re-weighted simulation candidates (see Sec. 5.3). Specifically, for the Λ_b^0, Λ, proton and π particles the total momentum, the transverse momentum and the pseudo-rapidity distributions are shown. Other distributions are also plotted and correspond to variables contained in the $\Lambda_b^0 \to \Lambda\gamma$ BDT (Table 5.10) for 2016, 2017 and 2018 years of data taking.

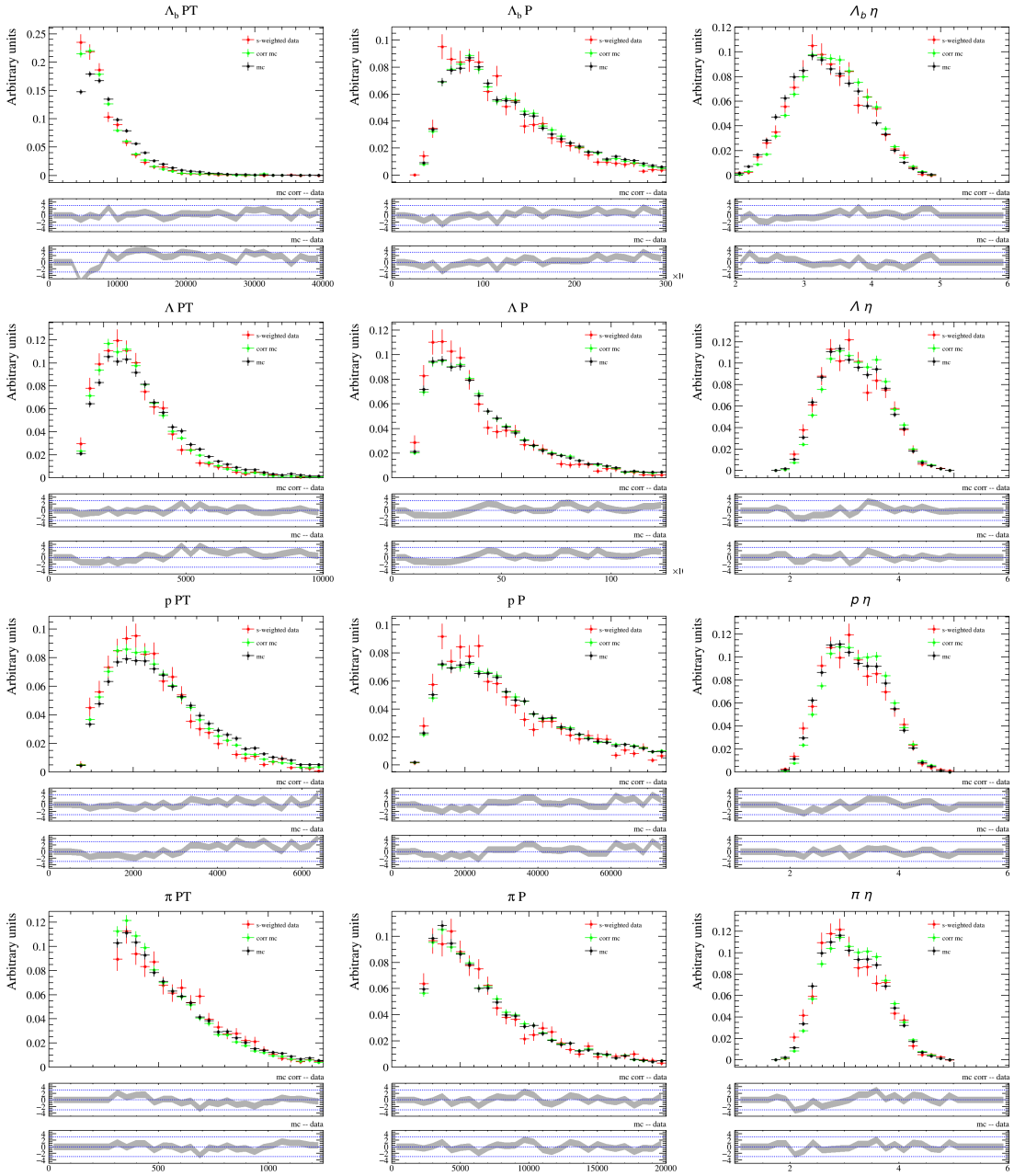

Figure A.6: Distributions of Λ_b^0, Λ, π and proton momenta and transverse momenta for sweighted data, simulation and corrected simulation candidates for 2016.

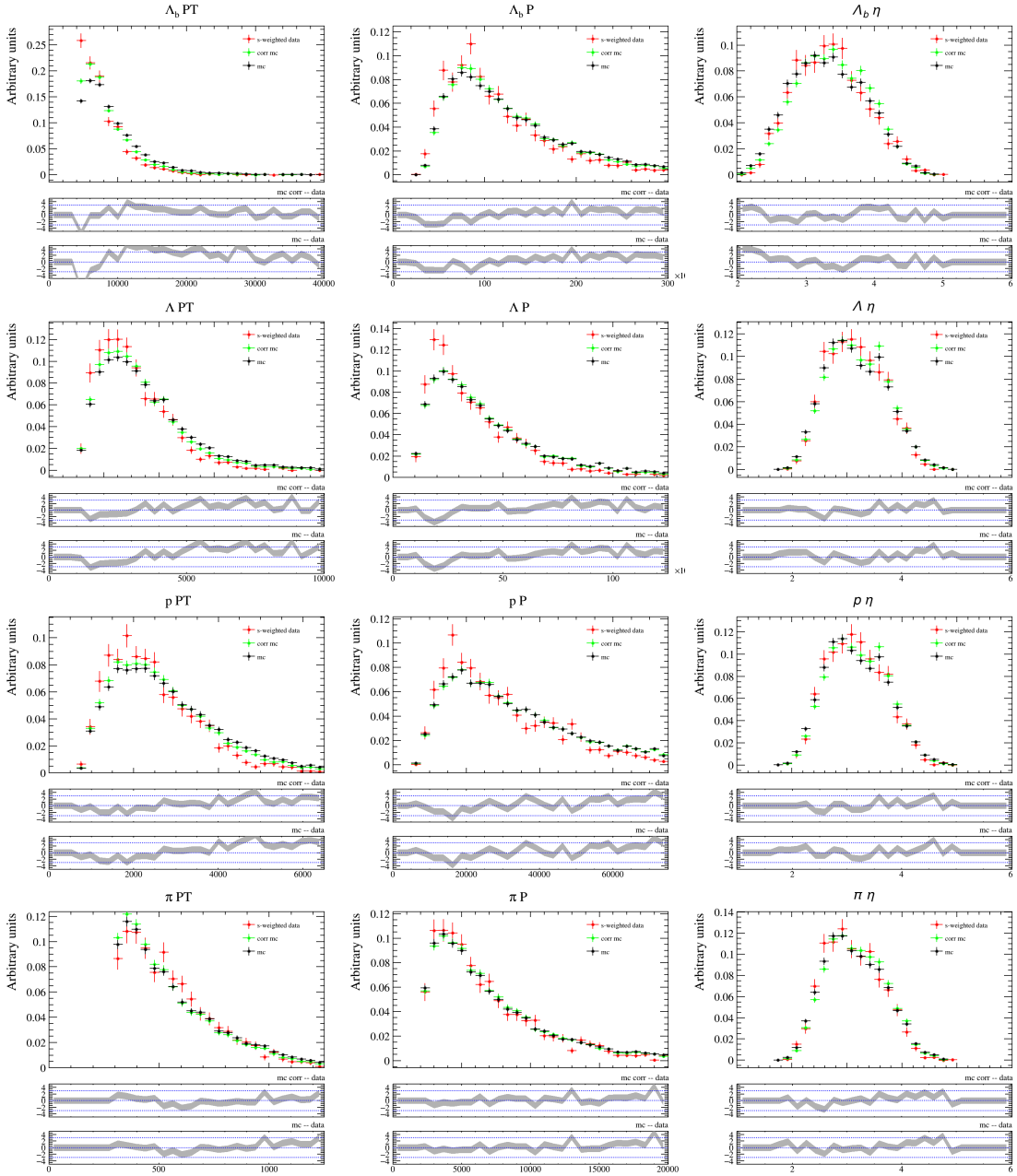

Figure A.7: Distributions of Λ_b^0 Λ, π and proton momenta and transverse momenta for sweighted data, simulation and corrected simulation candidates for 2017.

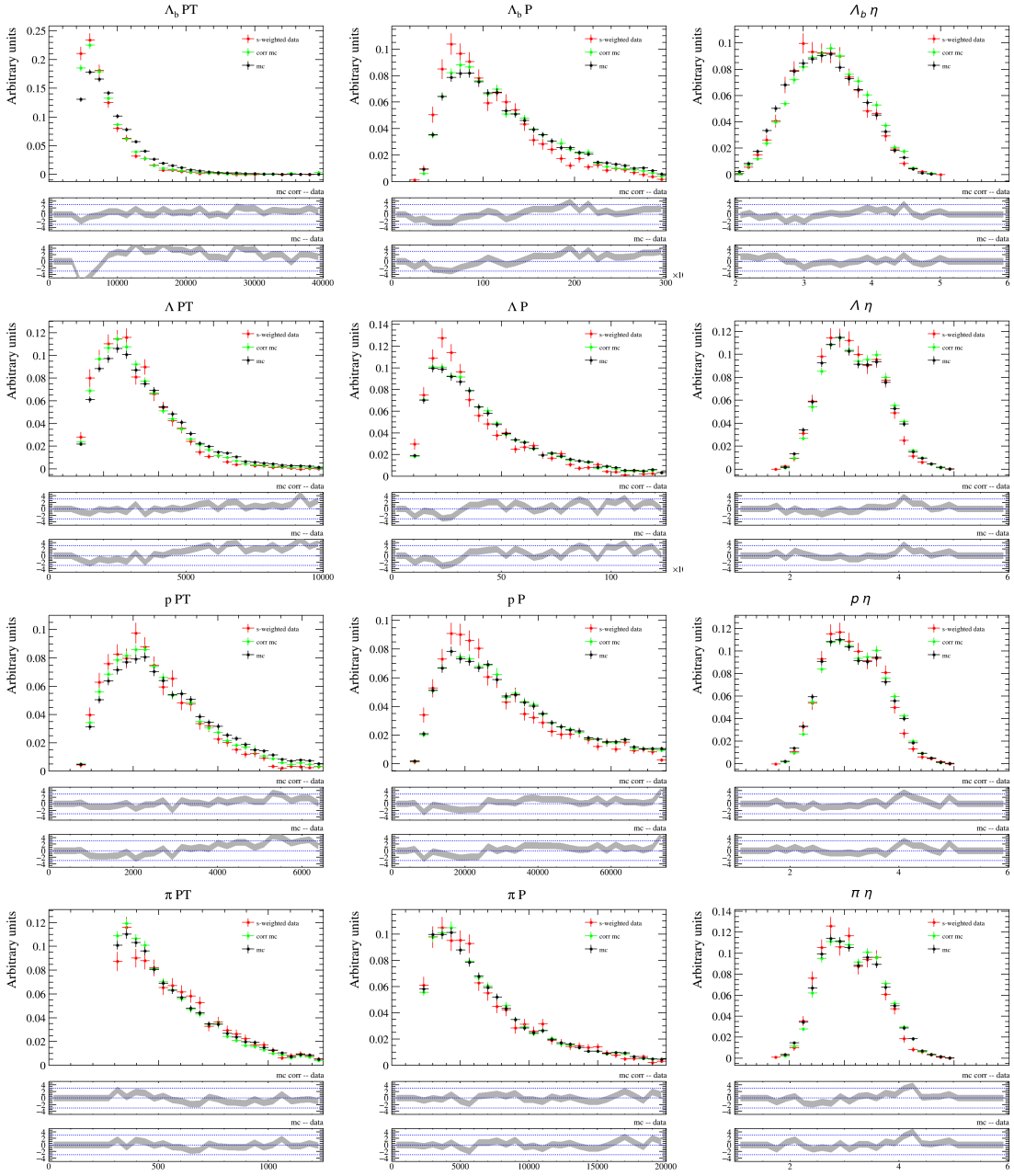

Figure A.8: Distributions of Λ, π and proton momenta and transverse momenta for sweighted data, simulation and corrected simulation candidates for 2018.

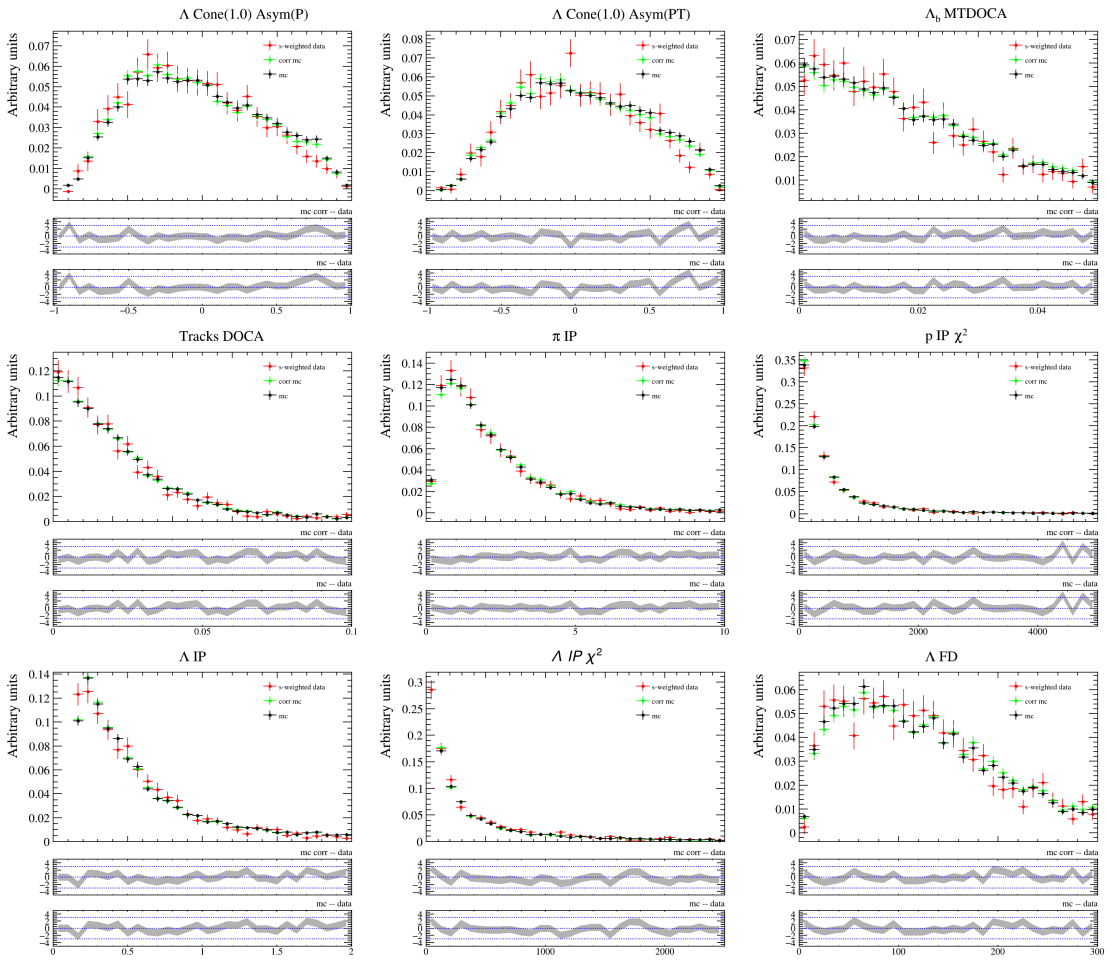

Figure A.9: Distributions of the variables contained in Table 5.10 for sweighted data, simulation and corrected simulation candidates for 2016.

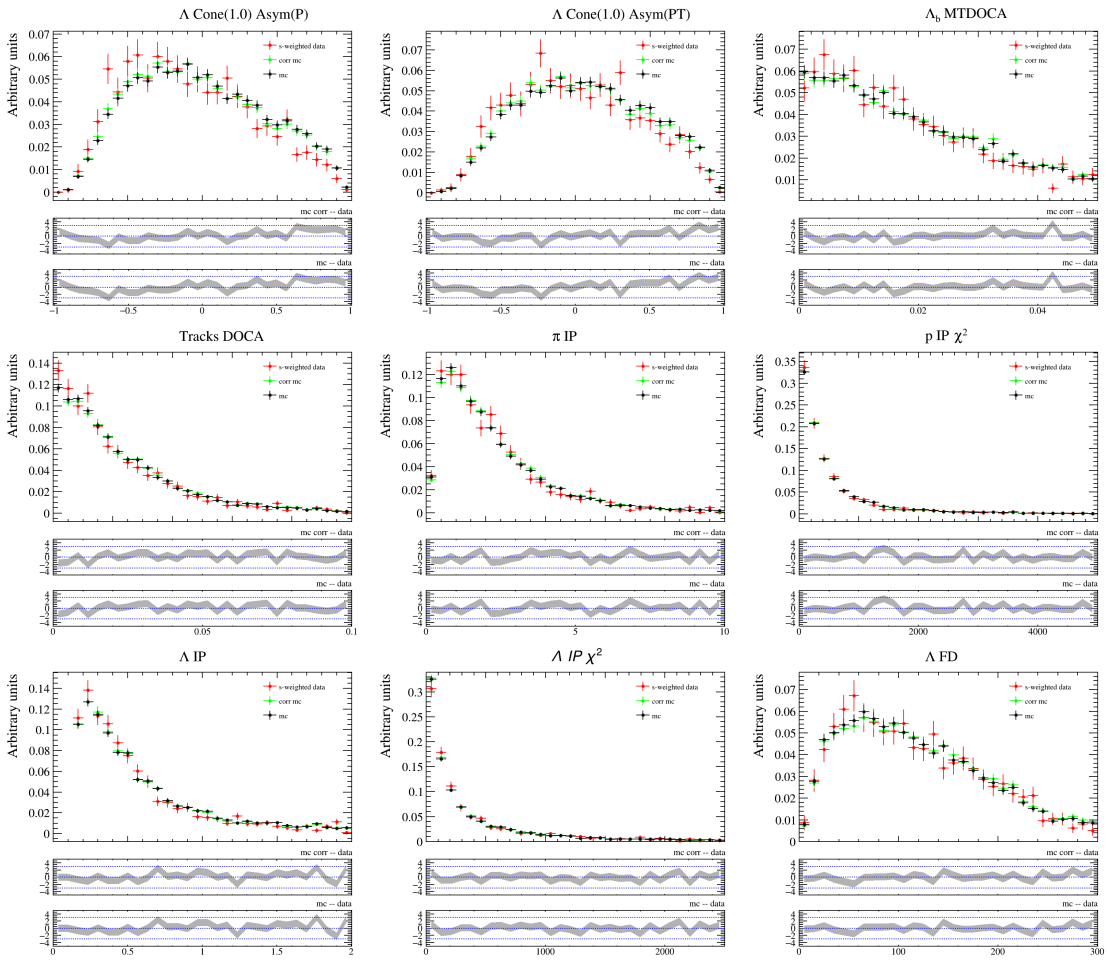

Figure A.10: Distributions of the variables contained in Table 5.10 for sweighted data, simulation and corrected simulation candidates for 2017.

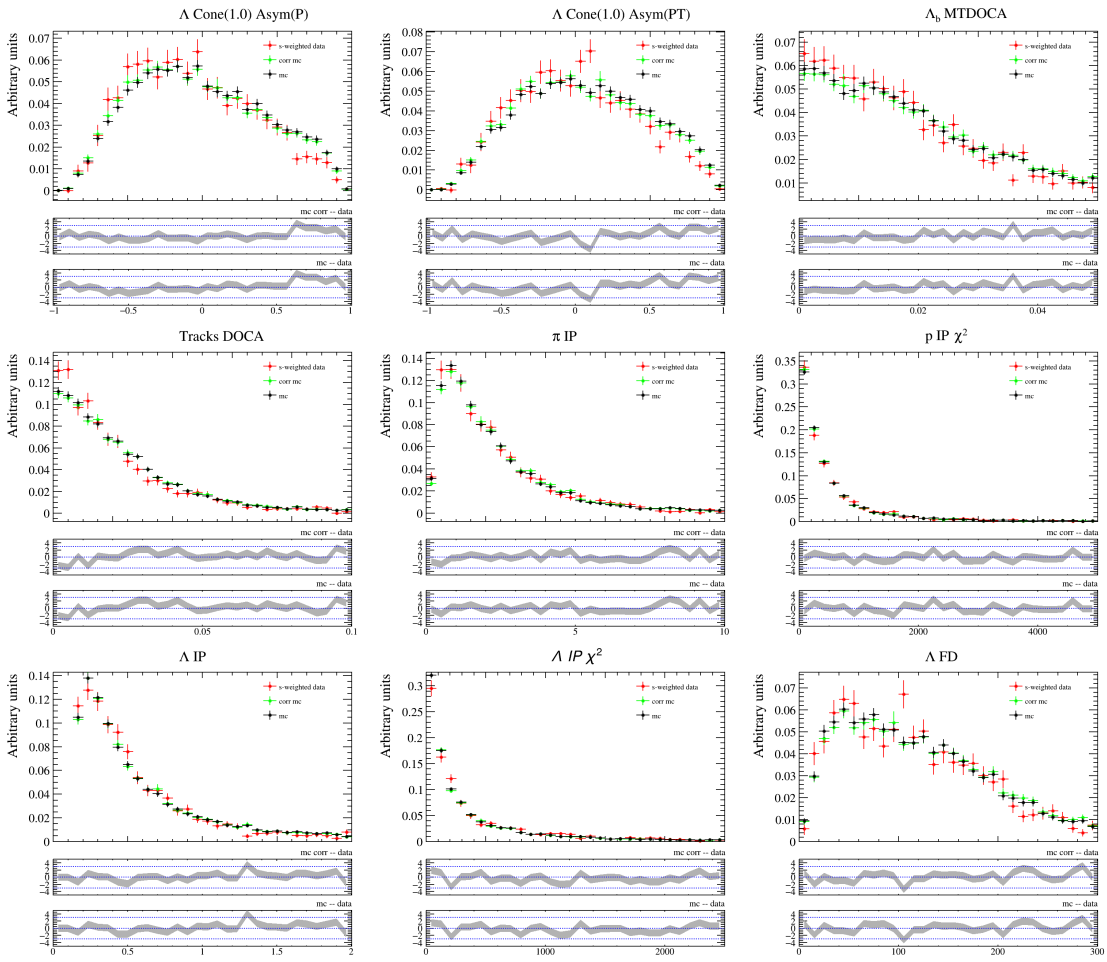

Figure A.11: Distributions of the variables contained in Table 5.10 for sweighted data, simulation and corrected simulation candidates for 2018.

A.3 BDT performance plots

Plots of the BDT output for the different periods of data-taking and both BDT-halves corresponding to the two-folding technique. Values of the figures of merit depending on the BDT cut applied for the different data-taking periods, BDT-halves and the two possible configurations, tight and loose configurations.

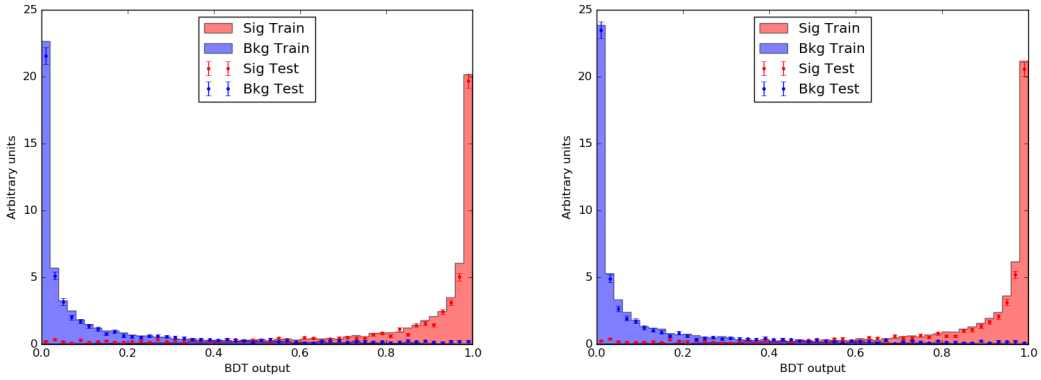

(a) (b)

Figure A.12: BDT output distributions for (a) BDT-half A and (b) BDT-half B for 2015 and 2016 period of data-taking.

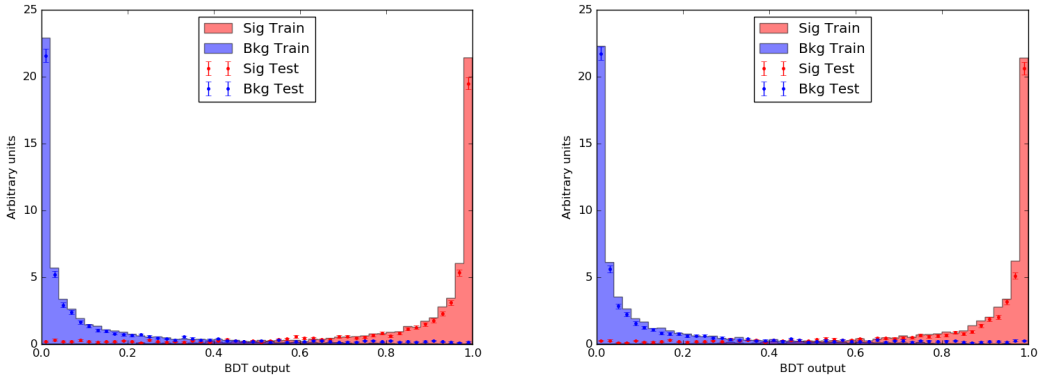

(a) (b)

Figure A.13: BDT output distributions for (a) BDT-half A and (b) BDT-half B for 2017 period of data-taking.

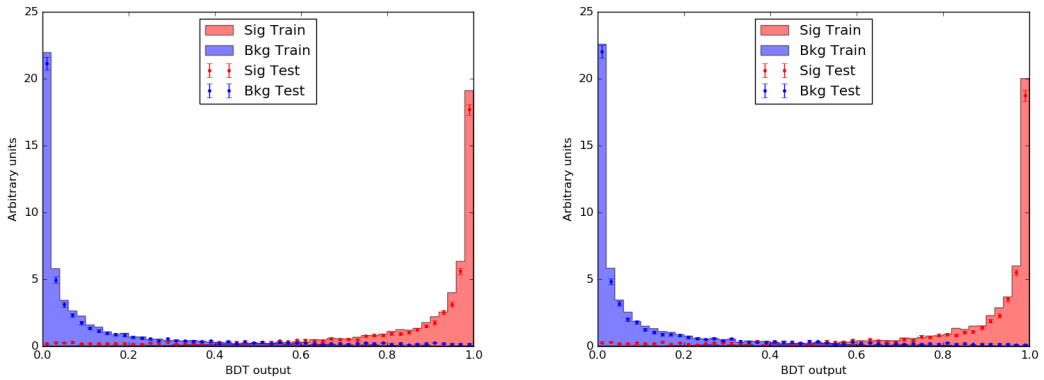

(a) (b)

Figure A.14: BDT output distributions for (a) BDT-half A and (b) BDT-half B for 2018 period of data-taking.

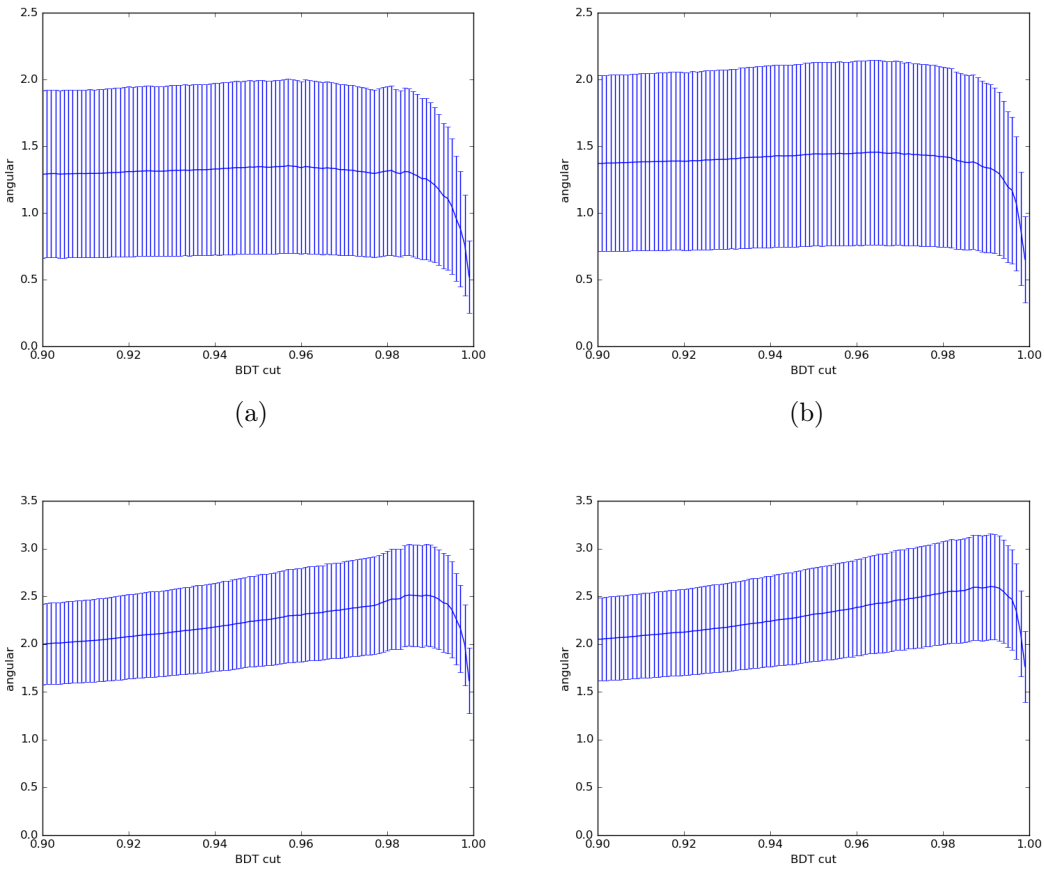

(a) (b)

(c) (d)

Figure A.15: Values of the figure of merit for 2015 and 2016 data-taking period for tight and loose configurations and both BDT-halves (A/B) (a) loose A (b) loose B (c) tight A (d) tight B.

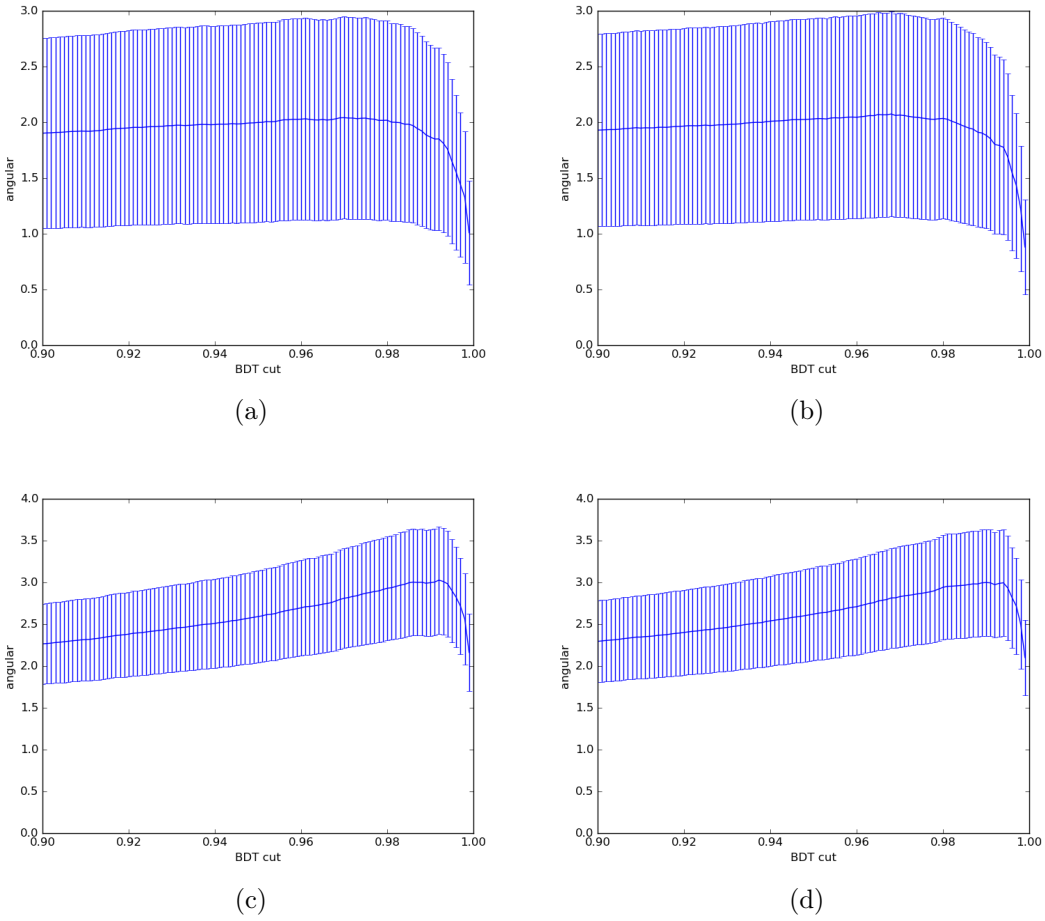

(a) (b)

(c) (d)

Figure A.16: Values of the figure of merit for 2017 data-taking period for tight and loose configurations and both BDT-halves (A/B) (a) loose A (b) loose B (c) tight A (d) tight B.

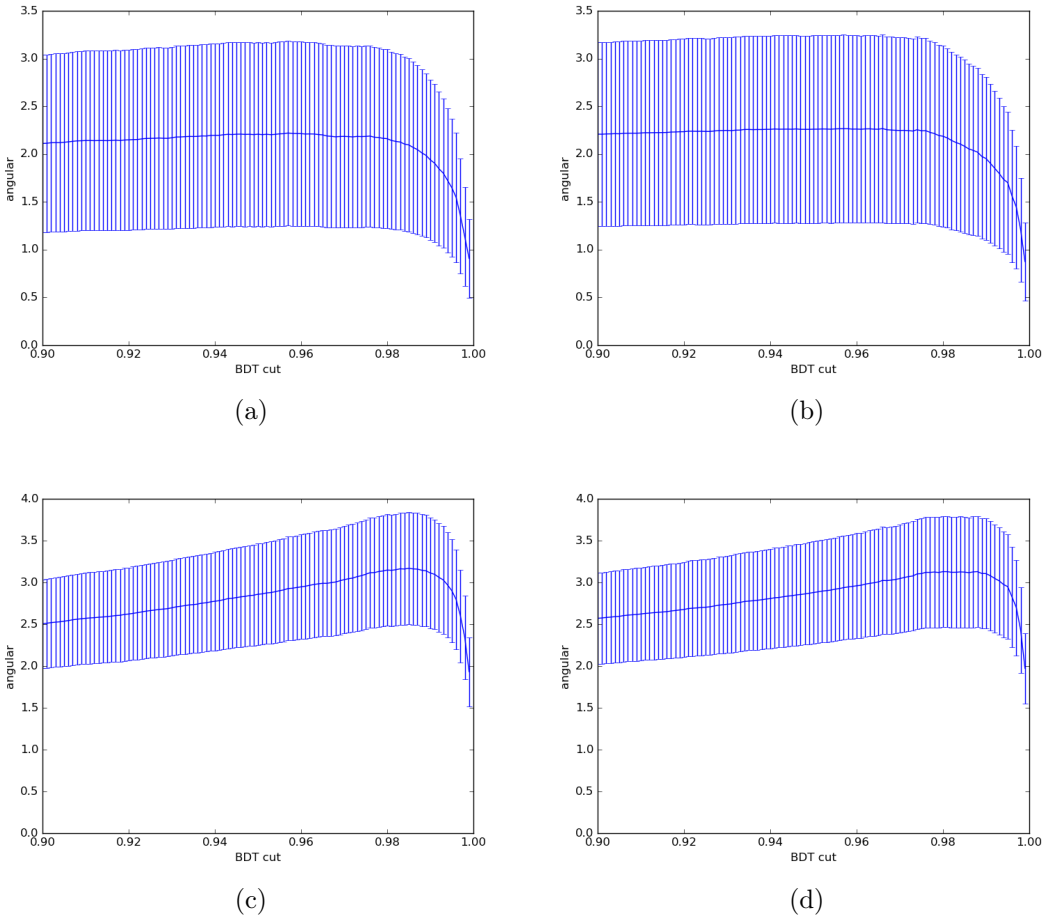

Figure A.17: Values of the figure of merit for 2018 data-taking period for tight and loose configurations and both BDT-halves (A/B) (a) loose A (b) loose B (c) tight A (d) tight B.

A.4 BDT efficiency vs invariant mass

Plots of the efficiency of a given cut of the BDT output variable in bins of Λ_b^0 mass. For the simulation samples the BDT cut used is 0.9, and for the data samples the BDT cut used is 0.05, for the low mass side band (LMSB) and high mass side band (HMSB).

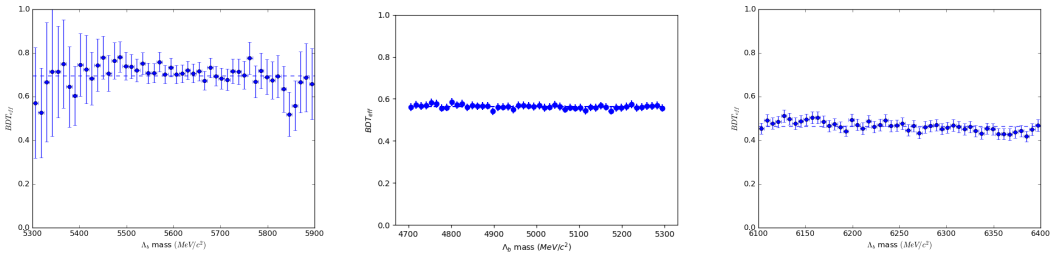

(a) (b) (c)

Figure A.18: BDT efficiency per Λ_b^0 mass bin on (a) simulation samples and (b,c) LMSB and HMSB data samples of the 2015 and 2016 period, respectively.

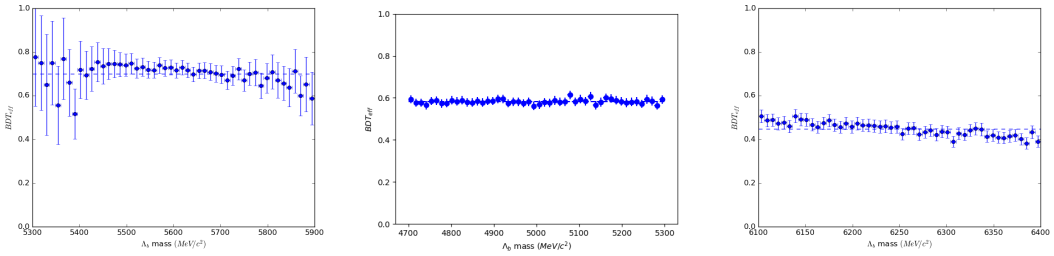

(a) (b) (c)

Figure A.19: BDT efficiency per Λ_b^0 mass bin on (a) simulation samples and (b, c) LMSB and HMSB data samples of the 2017 period, respectively.

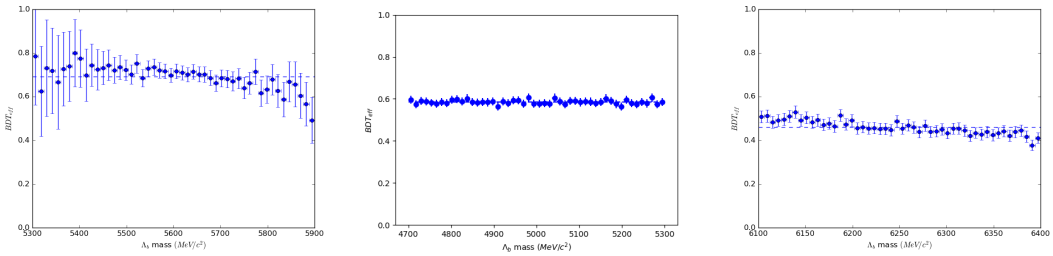

(a) (b) (c)

Figure A.20: BDT efficiency per Λ_b^0 mass bin of (a) simulation samples and (b,c) LMSB and HMSB data samples of the 2018 period, respectively.

A.5 Invariant mass fit of the control mode

A maximum likelihood invariant mass fit to $\Lambda_b^0 \to \Lambda J/\psi$ candidates of 2016, 2017 and 2018 data-taking periods is performed to extract the per-event sWeights, used to produce Fig. 5.21. Extracted from Ref. [2].

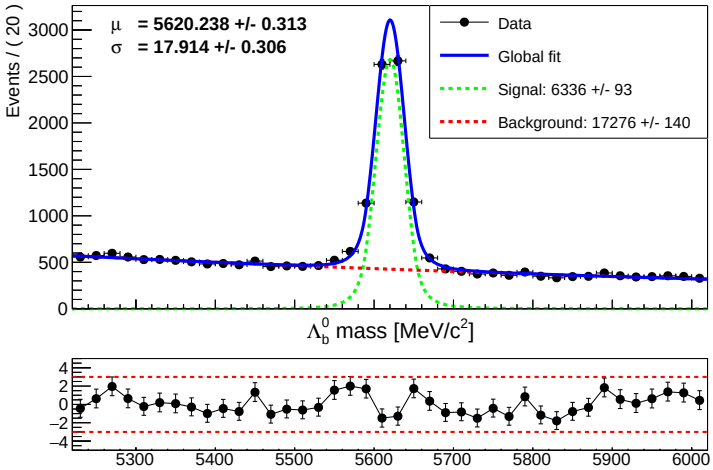

Figure A.21: Invariant mass fit to $\Lambda_b^0 \to \Lambda J/\psi$ candidates of 2016, 2017 and 2018 data-taking periods used to extract per-event sWeights. The result of the invariant mass fit is overlaid, along the fitted signal and background distributions.

A.6 sFit strategy

A second strategy is detailed to extract the photon polarization by disentangling the signal from the background contribution. It makes use of the sFit technique to extract per-event sWeights of signal and background candidates using the Λ_b^0 invariant mass as a control distribution. Allowing for a weighted unbinned fit to be performed to the proton helicity distribution, only considering the signal component:

$$\Gamma_{sW}(\alpha_\gamma;\theta_p) = \Gamma_{sig}(\alpha_\gamma;\theta_p)\cdot \mathrm{A}(\theta_p) \tag{A.1}$$

where $\Gamma_{sig}(\alpha_\gamma;\theta_p)$ is the theoretical distribution for $\Lambda_b^0 \to \Lambda\gamma$ candidates and $\mathrm{A}(\theta_p)$ is the acceptance distribution, modeled by a fourth order polynomial.

To study the performance of this strategy compared to the nominal one, the sensitivity to the photon polarization is studied for several sets of pseudo-datasets (5000), generated for different number of signal and background yields. For each pseudo-experiment, the Λ_b^0 invariant mass distribution and the proton helicity angle are generated for signal and combinatorial background, the presence of partially reconstructed candidates from $\Lambda_b^0 \to \Lambda\eta$ is not considered, given its small contribution.

The Λ_b^0 invariant mass shape of each of contribution is extracted from the mass fit presented in Sec. 5.4. The proton helicity distribution for signal candidates is extracted from the theoretical distribution multiplied by the acceptance. The proton helicity distribution of the background component is sampled from the data sidebands, defined previously.

The invariant mass distributions are generated in a window of 900 MeV/c^2 around the world-average Λ_b^0 mass. The angular distributions are generated within the physical limits (-1 to 1). In Fig. A.22, examples of generated invariant mass distributions for the (a) signal and (b) background contributions and the angular distribution for the signal (c) are shown.

A first invariant mass fit is performed following the same strategy presented in Sec. 5.4, extracting the values of μ, σ, τ and the signal and background yields. To be able to extract the per-event sWeights, a second invariant mass fit is performed in the reduced mass window of 2.5σ around the Λ_b^0 mass, an example is shown in Fig. A.23. In the latter fit all parameters are fixed except from the signal and background yields.

Lastly a fit is performed to the sWeighted proton helicity distribution to directly extract the photon polarization values (Fig. A.24). A SM-like value of the photon polarization is considered for all sets of pseudo-datasets. The result of the sensitivity to the photon polarization for each set is shown in Table A.1.

The sensitivity results for this strategy are significantly worse than the ones obtained using the nominal angular strategy. The result is understood given the signal and background yields, as it is acknowledged that the sFit technique is not be a good method with low signal yields and signal over background ratios. For completeness, sets Nº 4 and Nº 5 are generated to check the validity of this study

since both the sFit method and the nominal angular fit are expected to provide similar sensitivity to the photon polarization given high enough signal yields and signal over background ratios.

Set Nº	N_{sig}	N_{bkg}	S/B (2.5σ)	sFit Sens.	Ang. Sens.
1	122	606	0.79	0.50	0.38
2	212	1835	0.48	0.45	0.33
3	379	6115	0.23	0.44	0.33
4	2000	2000	~ 4	0.09	0.07
5	5250	2000	~ 10	0.05	0.04

Table A.1: Values of the generated signal and background yields in the full range, the approximate signal over background ratio in the reduced mass window, the sensitivity to the photon polarization using the sFit approach and the sensitivity to the photon polarization using the angular fit model for each set of pseudo-datasets.

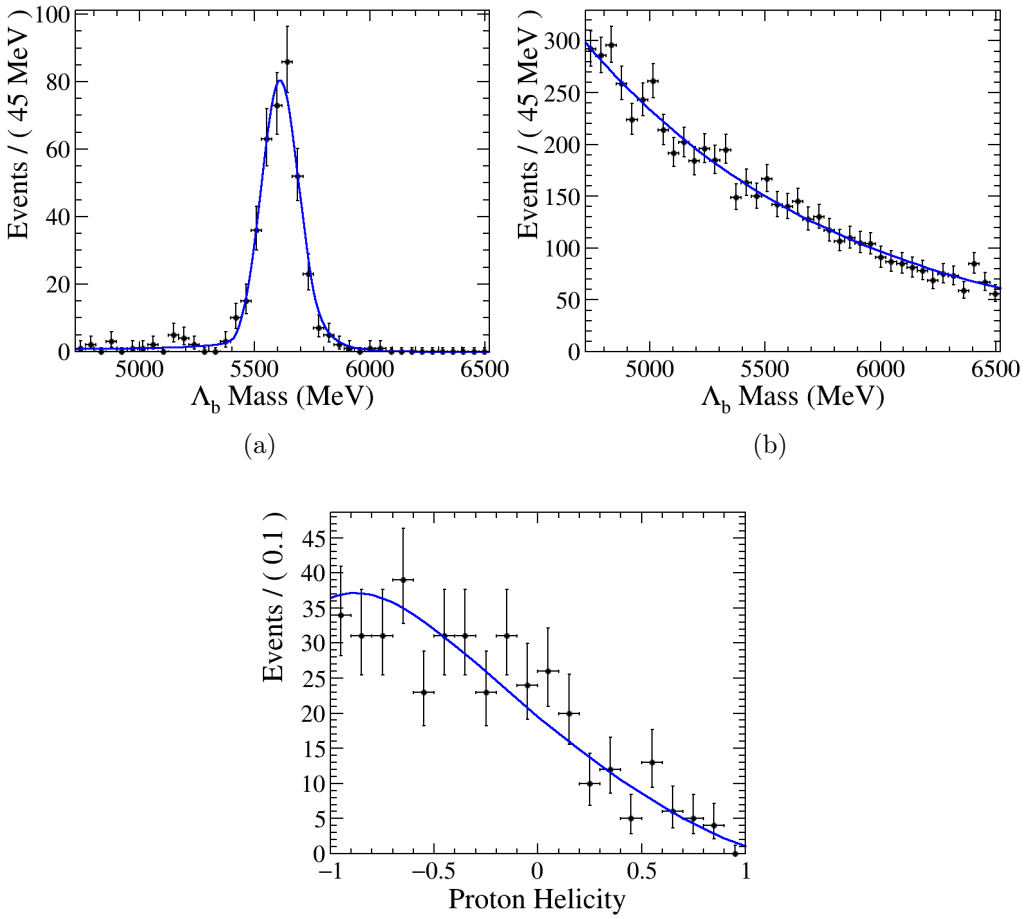

Figure A.22: Generated distributions for the invariant mass of (a) signal and (b) background contributions and for the (c) helicity angle of the signal component. pseudo-experiment of set Nº 3, the generation PDF is overlaid.

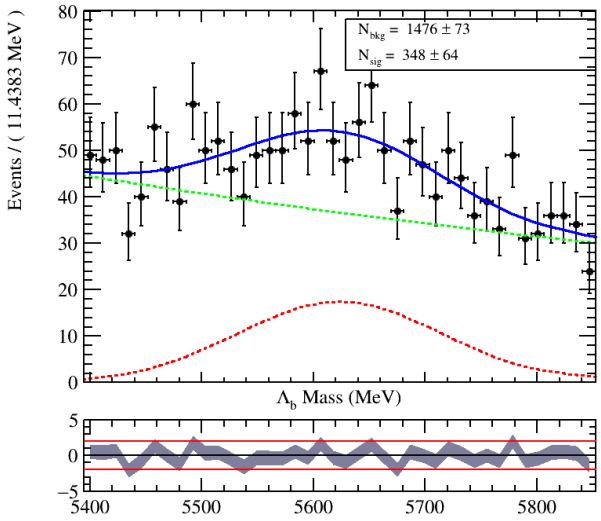

Figure A.23: Invariant mass distribution in the reduced mass region, used to extract per-event sWeights. pseudo-experiment of set Nº 3. The result of the invariant mass fit is overlaid, along the fitted signal and background yields.

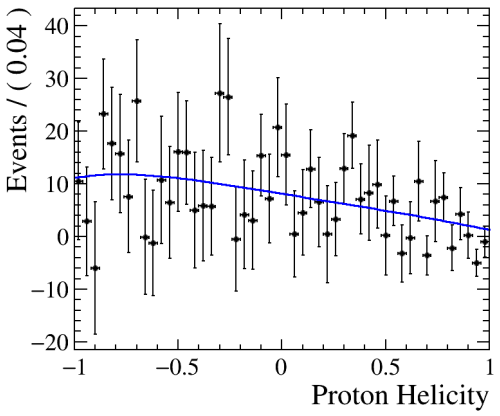

Figure A.24: Weighted unbinned fit to proton helicity distribution from a pseudo-experiment of set Nº 3, the fitted PDF is overlaid.

A.7 Systematic uncertainties pseudo-experiments

Plots of the α_γ dispersion and pull distributions for each of the systematic effects considered, from Ref. [2].

A.7.1 Acceptance

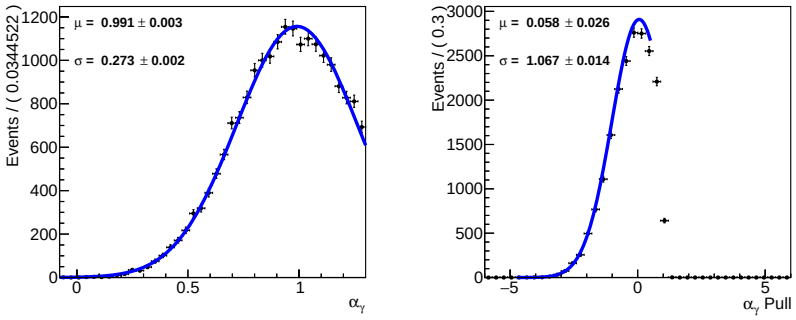

(a)

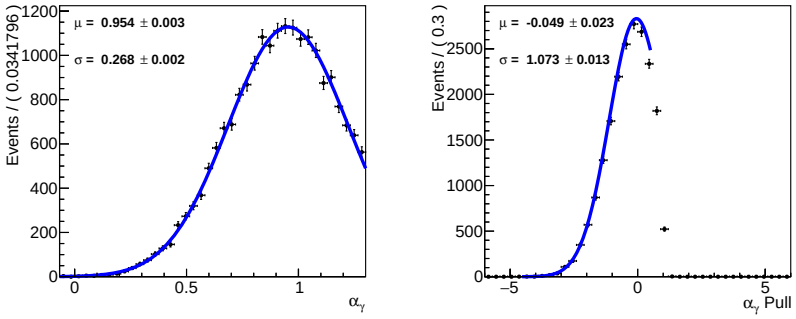

(b)

Figure A.25: Dispersion (left) and pull distribution (right) for α_γ fitted values for the $\Lambda_b^0 \to \Lambda\gamma$ pseudo-experiment study, considering the effects of (a) fluctuating the acceptance parameters and of (b) extracting the acceptance without the correction weights. The pseudo-experiments correspond to the loose configuration and they have been generated with $\alpha_\gamma = 1$. A Gaussian fit is superimposed.

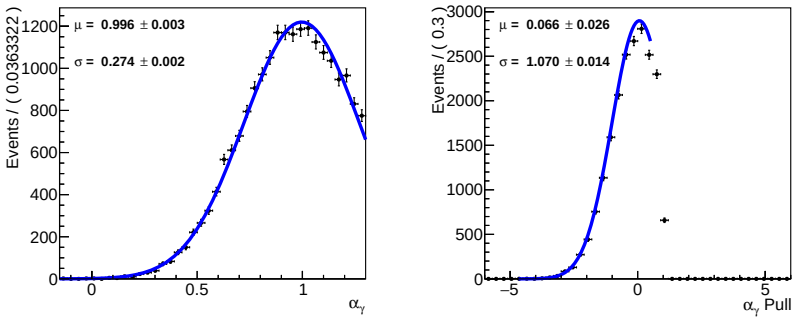

(a)

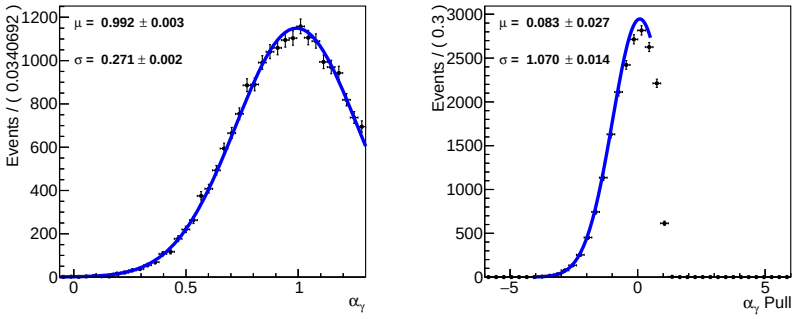

(b)

Figure A.26: Dispersion (left) and pull distribution (right) for α_γ fitted values for the $\Lambda_b^0 \to \Lambda\gamma$ pseudo-experiment study, considering the effects of using a (a) third and a (b) fifth order polynomial as alternative model for the acceptance. The pseudo-experiments correspond to the loose configuration and they have been generated with $\alpha_\gamma = 1$. A Gaussian fit is superimposed.

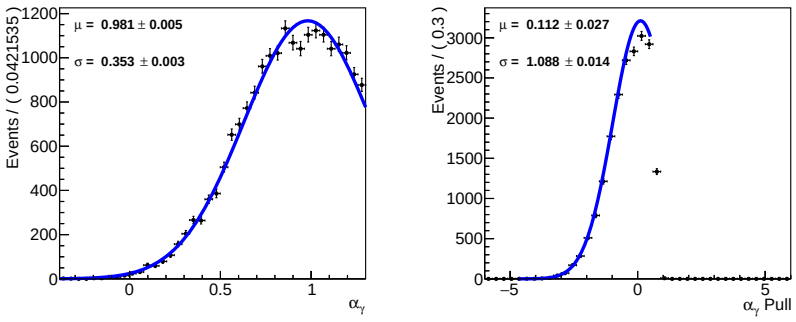

(a)

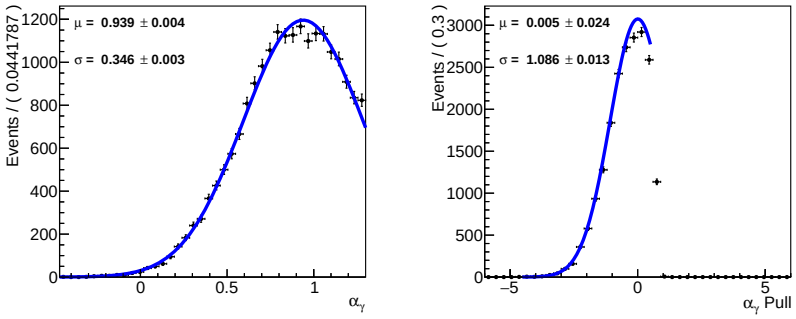

(b)

Figure A.27: Dispersion (left) and pull distribution (right) for α_γ fitted values for the $\Lambda_b^0 \to \Lambda\gamma$ pseudo-experiment study, considering the effects of (a) fluctuating the acceptance parameters and of (b) extracting the acceptance without the correction weights. The pseudo-experiments correspond to the tight configuration and they have been generated with $\alpha_\gamma = 1$. A Gaussian fit is superimposed.

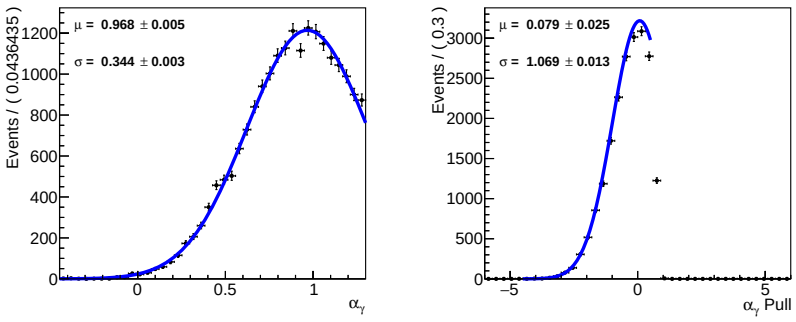

(a)

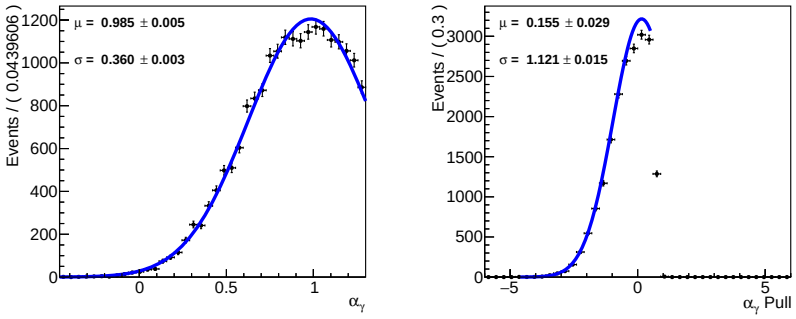

(b)

Figure A.28: Dispersion (left) and pull distribution (right) for α_γ fitted values for the $\Lambda_b^0 \to \Lambda\gamma$ pseudo-experiment study, considering the effects of using a (a) third and a (b) fifth order polynomial as alternative model for the acceptance. The pseudo-experiments correspond to the tight configuration and they have been generated with $\alpha_\gamma = 1$. A Gaussian fit is superimposed.

A.7.2 Background

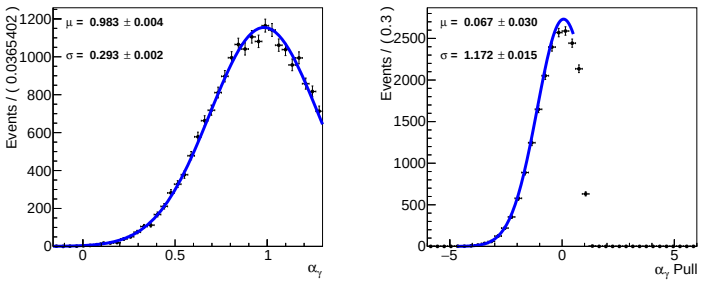

(a)

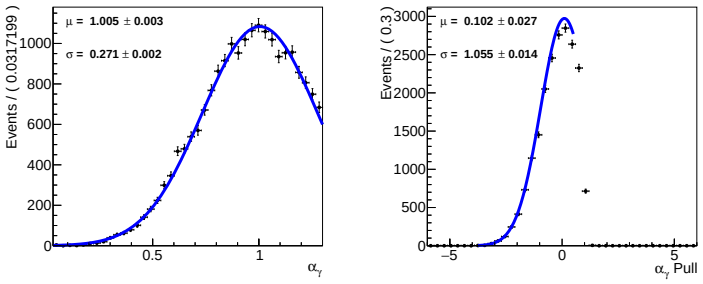

(b)

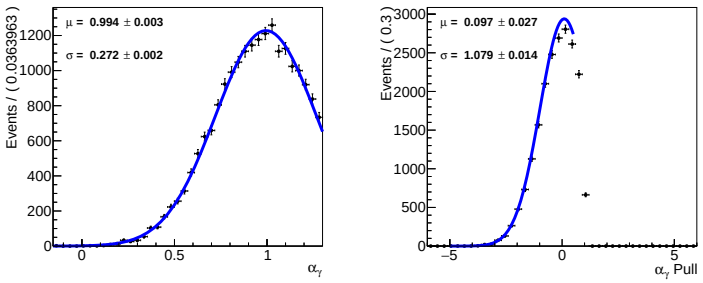

(c)

Figure A.29: Dispersion (left) and pull distribution (right) for α_γ fitted values for the $\Lambda_b^0 \to \Lambda\gamma$ pseudo-experiment study, considering the effects of (a) fluctuating the background parameters, and using a (b) third and a (c) fifth order polynomial as alternative model for the background. The pseudo-experiments correspond to the loose configuration and they have been generated with $\alpha_\gamma = 1$. A Gaussian fit is superimposed.

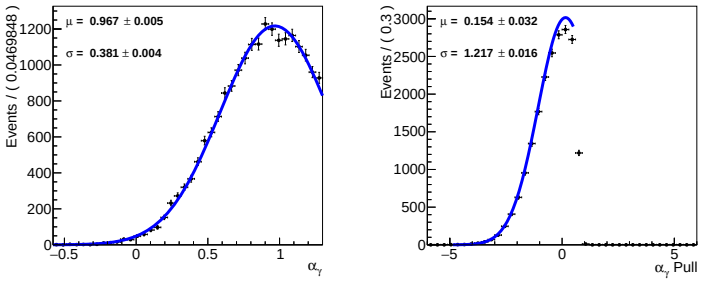

(a)

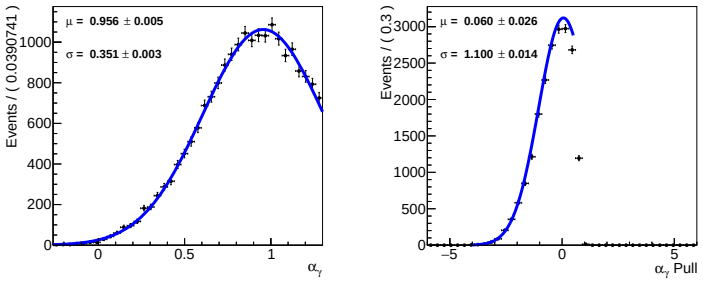

(b)

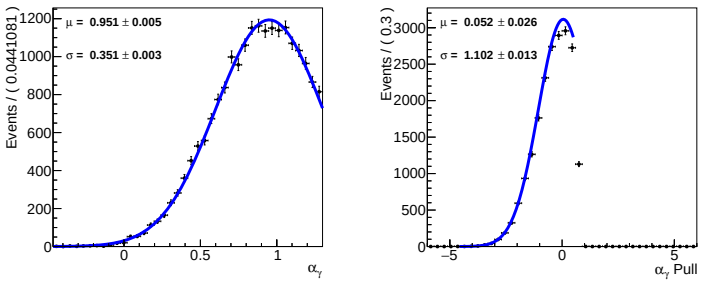

(c)

Figure A.30: Dispersion (left) and pull distribution (right) for α_γ fitted values for the $\Lambda_b^0 \to \Lambda\gamma$ pseudo-experiment study, considering the effects of (a) fluctuating the background parameters, and using a (b) third and a (c) fifth order polynomial as alternative model for the background. The pseudo-experiments correspond to the tight configuration and they have been generated with $\alpha_\gamma = 1$. A Gaussian fit is superimposed.

A.7.3 Signal and background yields

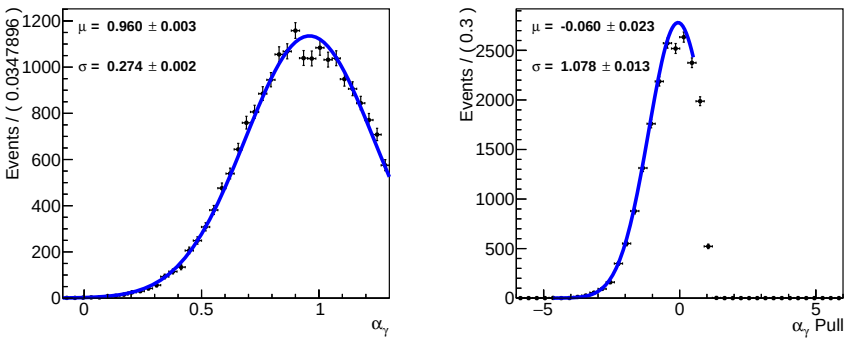

(a)

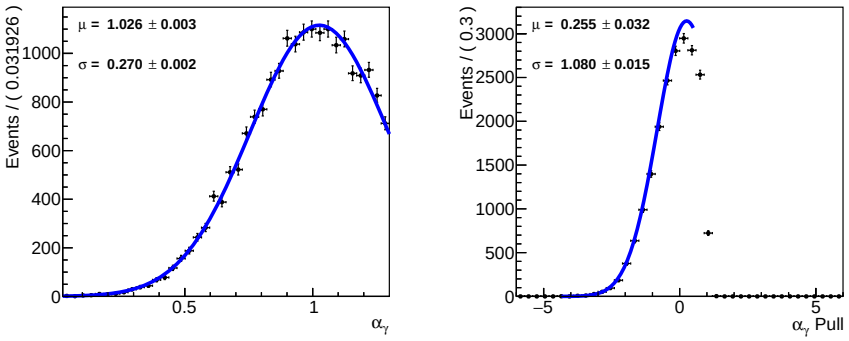

(b)

Figure A.31: Dispersion (left) and pull distribution (right) for α_γ fitted values for the $\Lambda_b^0 \to \Lambda\gamma$ pseudo-experiment study, generated a signal yield (a) reduced and (b) increased by a 10%. The nominal yield values are used for the signal fraction constraint in the angular fit. The pseudo-experiments correspond to the loose configuration and they have been generated with $\alpha_\gamma = 1$. A Gaussian fit is superimposed.

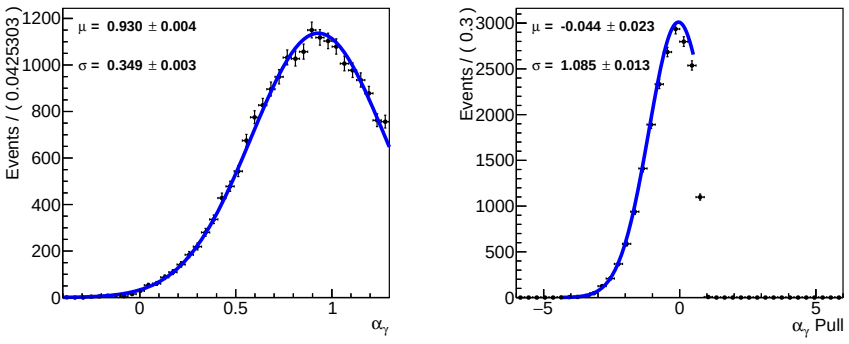

(a)

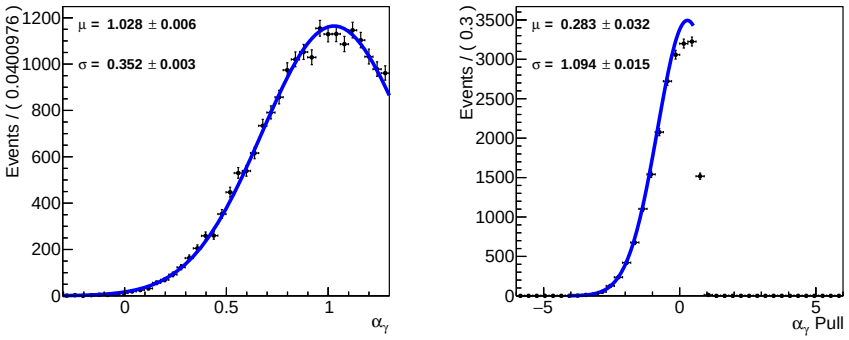

(b)

Figure A.32: Dispersion (left) and pull distribution (right) for α_γ fitted values for the $\Lambda_b^0 \to \Lambda\gamma$ pseudo-experiment study, generating a signal yield (a) reduced and (b) increased by a 10%. The nominal yield values are used for the signal fraction constraint in the angular fit. The pseudo-experiments correspond to the tight configuration and they have been generated with $\alpha_\gamma = 1$. A Gaussian fit is superimposed.

A.7.4 Uncertainty of the α_Λ parameter

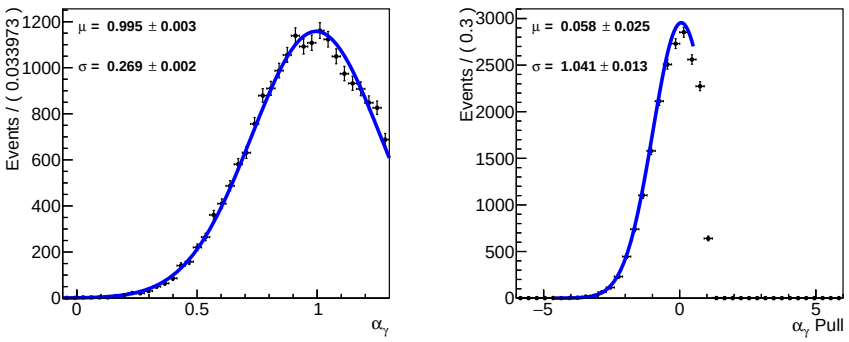

(a)

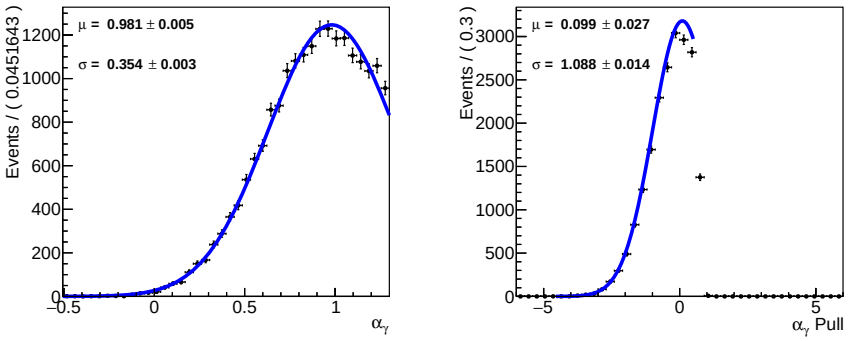

(b)

Figure A.33: Dispersion (left) and pull distribution (right) for α_γ fitted values for the $\Lambda_b^0 \to \Lambda\gamma$ pseudo-experiment study, considering the effect of fluctuating the α_Λ parameter, for the (a) loose and (b) tight configurations. The pseudo-experiments have been generated with $\alpha_\gamma = 1$. A Gaussian fit is superimposed.

A.8 Likelihoods and Feldman Cousins

Profile of the negative log likelihood along the photon polarization values for the combined, $\Lambda_b^0 \to \Lambda\gamma$ and $\overline{\Lambda}_b^0 \to \overline{\Lambda}\gamma$ samples. The photon polarization range differs for each sample since it depends on each signal PDF, that becomes negative for $\alpha_\gamma = \pm\frac{1}{\alpha_\Lambda}$, which at its turn depends on α_Λ, which differs for each sample.

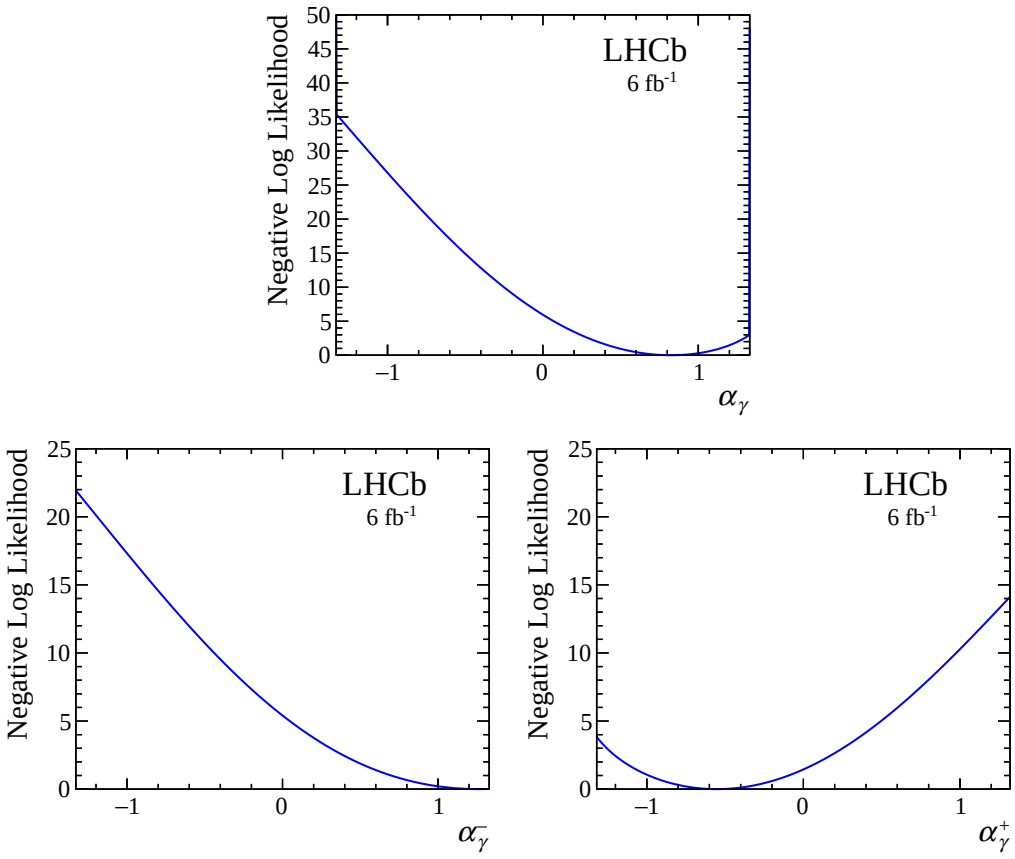

Figure A.34: Profile of the negative log likelihood along the (top) combined, (bottom-left) $\Lambda_b^0 \to \Lambda\gamma$ and (bottom-right) $\overline{\Lambda}_b^0 \to \overline{\Lambda}\gamma$ photon polarization values (α_γ, α_γ^- and α_γ^+, respectively).

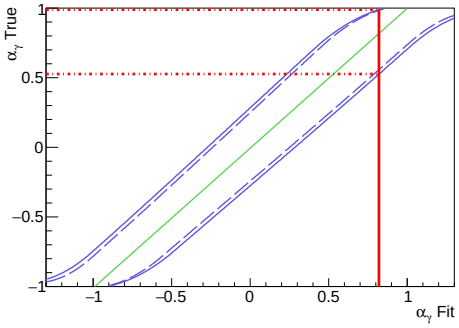

Figure A.35: Neyman confidence belt at 1σ showing the true value for α_γ as a function of the measured value of α_γ for the combined sample. The green line represents the relation between the true and the measured values, the dashed blue line is the Neyman belt considering only the statistical uncertainty, while the full blue line considers also the systematic uncertainty effects. The measured and true values of α_γ are represented by a red line.

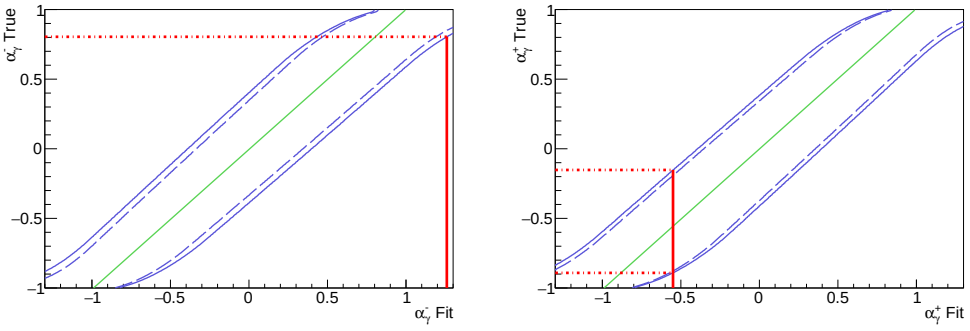

(a) (b)

Figure A.36: Neyman confidence belt at 1σ showing the true value for α_γ as a function of the measured value of α_γ for the (a) only $\Lambda_b^0 \to \Lambda\gamma$ and (b) $\overline{\Lambda}_b^0 \to \overline{\Lambda}\gamma$ samples. The green line represents the relation between the true and the measured values, the dashed blue line is the Neyman belt considering only the statistical uncertainty, while the full blue line considers also the systematic uncertainty effects. The measured and true values of α_γ are represented by a red line.

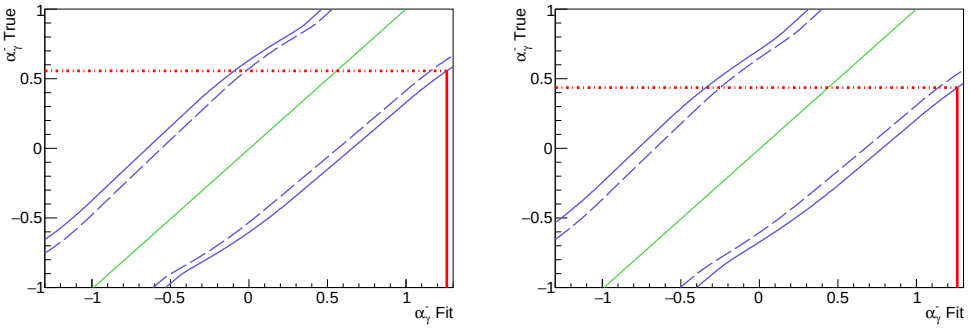

(a) (b)

Figure A.37: Confidence intervals on α_γ^- using the Feldman-Cousins approach within the physical limits of this parameter. The dotted green line is the relation between the central value measured by the fit and the true value, while the blue lines are the 90% (left) and 95% (right) confidence intervals including statistical (dashed) and statistical and systematic (solid) uncertainties. The red vertical line is the central value measured by the fit and the horizontal lines are the derived confidence interval.

Bibliography

[1] LHCb Collaboration, R. Aaij *et al.*, *Measurement of the photon polarization in $\Lambda_b^0 \to \Lambda\ \gamma$ decays*, Phys. Rev. D **105** (2022), no. 5 L051104, arXiv:2111.10194.

[2] LHCb Collaboration, *Internal Analysis Note: Measurement of the photon polarization in $\Lambda_b^0 \to \Lambda\gamma$ decays*, LHCb-ANA-2020-066 (2021).

[3] ATLAS Collaboration, G. Aad *et al.*, *The ATLAS Experiment at the CERN Large Hadron Collider*, JINST **3** (2008) S08003.

[4] CMS Collaboration, S. Chatrchyan *et al.*, *The CMS Experiment at the CERN LHC*, JINST **3** (2008) S08004.

[5] LHCb Collaboration, A. A. Alves, Jr. *et al.*, *The LHCb Detector at the LHC*, JINST **3** (2008) S08005.

[6] ALICE Collaboration, K. Aamodt *et al.*, *The ALICE experiment at the CERN LHC*, JINST **3** (2008) S08002.

[7] ATLAS Collaboration, G. Aad *et al.*, *Observation of a new particle in the search for the Standard Model Higgs boson with the ATLAS detector at the LHC*, Phys. Lett. B **716** (2012) 1, arXiv:1207.7214.

[8] CMS Collaboration, S. Chatrchyan *et al.*, *Observation of a New Boson at a Mass of 125 GeV with the CMS Experiment at the LHC*, Phys. Lett. B **716** (2012) 30, arXiv:1207.7235.

[9] LHCb Collaboration, *LHCb technical design report: Reoptimized detector design and performance*, CERN-LHCC-2003-030, LHCb-TDR-009 (2003).

[10] LHCb Collaboration, R. Aaij *et al.*, *LHCb Detector Performance*, Int. J. Mod. Phys. A **30** (2015), no. 07 1530022, arXiv:1412.6352.

[11] R. Aaij *et al.*, *Performance of the LHCb Vertex Locator*, JINST **9** (2014) P09007, arXiv:1405.7808.

[12] LHCb Collaboration, *LHCb VELO TDR: Vertex locator. Technical design report*, CERN-LHCC-2001-011, LHCb-TDR-005 (2001).

[13] J. Gassner, M. Needham, and O. Steinkamp, *Layout and Expected Performance of the LHCb TT Station*, .

[14] LHCb Collaboration, *LHCb magnet: Technical design report*, CERN-LHCC-2000-007, LHCb-TDR-001 (2000).

[15] LHCb Collaboration, *LHCb: Inner tracker technical design report*, CERN-LHCC-2002-029, LHCb-TDR-008 (2002).

[16] LHCb Collaboration, *LHCb: Outer tracker technical design report*, CERN-LHCC-2001-024, LHCb-TDR-006 (2001).

[17] LHCb Collaboration, *LHCb: RICH technical design report*, CERN-LHCC-2000-037, LHCb-TDR-003 (2000).

[18] P. A. Cherenkov, *Visible luminescence of pure liquids under the influence of γ-radiation*, Dokl. Akad. Nauk SSSR **2** (1934), no. 8 451.

[19] LHCb Collaboration, *LHCb calorimeters: Technical design report*, CERN-LHCC-2000-036, LHCb-TDR-002 (2000).

[20] A. Arefev *et al.*, *Beam test results of the LHCb electromagnetic calorimeter*, .

[21] LHCb Collaboration, *LHCb muon system technical design report*, CERN-LHCC-2001-010, LHCb-TDR-004 (2001).

[22] R. Calabrese *et al.*, *Performance of the LHCb RICH detectors during LHC Run 2*, JINST **17** (2022), no. 07 P07013, `arXiv:2205.13400`.

[23] M. Calvo Gomez *et al.*, *A tool for γ/π^0 separation at high energies*, Tech. Rep. LHCb-PUB-2015-016. CERN-LHCb-PUB-2015-016, CERN, Geneva, Aug, 2015.

[24] LHCb Collaboration, R. Aaij *et al.*, *Design and performance of the LHCb trigger and full real-time reconstruction in Run 2 of the LHC*, JINST **14** (2019), no. 04 P04013, `arXiv:1812.10790`.

[25] W. N. Cottingham and D. A. Greenwood, *An introduction to the standard model of particle physics*, Cambridge University Press, 4, 2007.

[26] M. E. Peskin and D. V. Schroeder, *An Introduction to quantum field theory*, Addison-Wesley, Reading, USA, 1995.

[27] S. Weinberg, *A Model of Leptons*, Phys. Rev. Lett. **19** (1967) 1264.

[28] M. Y. Han and Y. Nambu, *Three Triplet Model with Double SU(3) Symmetry*, Phys. Rev. **139** (1965) B1006.

[29] S. L. Glashow, *Partial Symmetries of Weak Interactions*, Nucl. Phys. **22** (1961) 579.

[30] A. Salam and J. C. Ward, *Electromagnetic and weak interactions*, Phys. Lett. **13** (1964) 168.

[31] P. W. Higgs, *Broken Symmetries and the Masses of Gauge Bosons*, Phys. Rev. Lett. **13** (1964) 508.

[32] UA2, P. Bagnaia *et al.*, *Evidence for $Z^0 \to e^+e^-$ at the CERN $\bar{p}p$ Collider*, Phys. Lett. B **129** (1983) 130.

[33] UA1, G. Arnison *et al.*, *Experimental Observation of Isolated Large Transverse Energy Electrons with Associated Missing Energy at $\sqrt{s} = 540$ GeV*, Phys. Lett. B **122** (1983) 103.

[34] N. Cabibbo, *Unitary Symmetry and Leptonic Decays*, Phys. Rev. Lett. **10** (1963) 531.

[35] M. Kobayashi and T. Maskawa, *CP Violation in the Renormalizable Theory of Weak Interaction*, Prog. Theor. Phys. **49** (1973) 652.

[36] L. Wolfenstein, *Parametrization of the Kobayashi-Maskawa Matrix*, Phys. Rev. Lett. **51** (1983) 1945.

[37] Particle Data Group, P. A. Zyla *et al.*, *Review of Particle Physics*, PTEP **2020** (2020), no. 8 083C01.

[38] LHCb Collaboration, B. Adeva *et al.*, *Roadmap for selected key measurements of LHCb*, arXiv:0912.4179.

[39] B. Pontecorvo, *Inverse beta processes and nonconservation of lepton charge*, Zh. Eksp. Teor. Fiz. **34** (1957) 247.

[40] Z. Maki, M. Nakagawa, and S. Sakata, *Remarks on the unified model of elementary particles*, Prog. Theor. Phys. **28** (1962) 870.

[41] S. L. Glashow, J. Iliopoulos, and L. Maiani, *Weak Interactions with Lepton-Hadron Symmetry*, Phys. Rev. D **2** (1970) 1285.

[42] K. G. Wilson, *Nonlagrangian models of current algebra*, Phys. Rev. **179** (1969) 1499.

[43] S. Descotes-Genon, D. Ghosh, J. Matias, and M. Ramon, *Exploring New Physics in $C_7 - C_{7'}$*, PoS **EPS-HEP2011** (2011) 170, arXiv:1202.2172.

[44] D. Atwood, M. Gronau, and A. Soni, *Mixing induced CP asymmetries in radiative B decays in and beyond the standard model*, Phys. Rev. Lett. **79** (1997) 185, arXiv:hep-ph/9704272.

[45] LHCb Collaboration, R. Aaij *et al.*, *First Observation of the Radiative Decay $\Lambda_b^0 \to \Lambda\gamma$*, Phys. Rev. Lett. **123** (2019), no. 3 031801, arXiv:1904.06697.

[46] LHCb Collaboration, R. Aaij *et al.*, *Search for the radiative $\Xi_b^- \to \Xi^-\gamma$ decay*, JHEP **01** (2022) 069, arXiv:2108.07678.

[47] BaBar Collaboration, B. Aubert *et al.*, *Measurement of Branching Fractions and CP and Isospin Asymmetries in $B \to K^*(892)\gamma$ Decays*, Phys. Rev. Lett. **103** (2009) 211802, arXiv:0906.2177.

[48] Belle Collaboration, D. Dutta *et al.*, *Search for $B_s^0 \to \gamma\gamma$ and a measurement of the branching fraction for $B_s^0 \to \phi\gamma$*, Phys. Rev. D **91** (2015), no. 1 011101, arXiv:1411.7771.

[49] LHCb Collaboration, R. Aaij *et al.*, *Measurement of the ratio of branching fractions $BR(B_0 \to K^{\star 0}\gamma)/BR(B_{s0} \to \phi\gamma)$ and the direct CP asymmetry in $B_0 \to K^{\star 0}\gamma$*, Nucl. Phys. B **867** (2013) 1, arXiv:1209.0313.

[50] BaBar Collaboration, B. Aubert *et al.*, *Measurement of Time-Dependent CP Asymmetry in $B^0 \to K^0_S\pi^0\gamma$ Decays*, Phys. Rev. D **78** (2008) 071102, arXiv:0807.3103.

[51] LHCb Collaboration, R. Aaij *et al.*, *Observation of Photon Polarization in the $b\to s\gamma$ Transition*, Phys. Rev. Lett. **112** (2014), no. 16 161801, arXiv:1402.6852.

[52] LHCb Collaboration, R. Aaij *et al.*, *First experimental study of photon polarization in radiative B^0_s decays*, Phys. Rev. Lett. **118** (2017), no. 2 021801, arXiv:1609.02032, [Addendum: Phys.Rev.Lett. 118, 109901 (2017)].

[53] LHCb Collaboration, R. Aaij *et al.*, *Measurement of CP-violating and mixing-induced observables in $B^0_s \to \phi\gamma$ decays*, Phys. Rev. Lett. **123** (2019), no. 8 081802, arXiv:1905.06284.

[54] LHCb Collaboration, R. Aaij *et al.*, *Strong constraints on the $b \to s\gamma$ photon polarisation from $B^0 \to K^{*0}e^+e^-$ decays*, JHEP **12** (2020) 081, arXiv:2010.06011.

[55] B. Grinstein, Y. Grossman, Z. Ligeti, and D. Pirjol, *Photon polarization in $b \to x\gamma$ in the standard model*, Phys. Rev. D **71** (2005) 011504.

[56] V. Cirigliano *et al.*, *Kaon Decays in the Standard Model*, Rev. Mod. Phys. **84** (2012) 399, arXiv:1107.6001.

[57] A. J. Buras, *Weak Hamiltonian, CP violation and rare decays*, in *Les Houches Summer School in Theoretical Physics, Session 68: Probing the Standard Model of Particle Interactions*, pp. 281–539, 6, 1998. arXiv:hep-ph/9806471.

[58] J. Bijnens, G. Ecker, and J. Gasser, *Chiral perturbation theory*, 11, 1994. arXiv:hep-ph/9411232.

[59] S. Scherer, *Introduction to chiral perturbation theory*, Adv. Nucl. Phys. **27** (2003) 277, arXiv:hep-ph/0210398.

[60] G. D'Ambrosio, G. Ecker, G. Isidori, and H. Neufeld, *Radiative nonleptonic kaon decays*, 11, 1994. arXiv:hep-ph/9411439.

[61] G. D'Ambrosio, D. Greynat, and G. Vulvert, *Standard Model and New Physics contributions to K_L and K_S into four leptons*, Eur. Phys. J. C **73** (2013), no. 12 2678, arXiv:1309.5736.

[62] LHCb Collaboration, R. Aaij *et al.*, *Search for the rare decay $K_S \to \mu^+\mu^-$*, JHEP **01** (2013) 090, arXiv:1209.4029.

[63] LHCb Collaboration, R. Aaij *et al.*, *Improved limit on the branching fraction of the rare decay $K^0_S \to \mu^+\mu^-$*, Eur. Phys. J. C **77** (2017), no. 10 678, arXiv:1706.00758.

[64] LHCb Collaboration, R. Aaij *et al.*, *Constraints on the $K^0_S \to \mu^+\mu^-$ Branching Fraction*, Phys. Rev. Lett. **125** (2020), no. 23 231801, arXiv:2001.10354.

[65] LHCb Collaboration, R. Aaij *et al.*, *Evidence for the rare decay $\Sigma^+ \to p\mu^+\mu^-$*, Phys. Rev. Lett. **120** (2018), no. 22 221803, arXiv:1712.08606.

[66] V. Chobanova *et al.*, *Probing SUSY effects in $K^0_S \to \mu^+\mu^-$*, JHEP **05** (2018) 024, arXiv:1711.11030.

[67] I. Dorsner *et al.*, *Limits on scalar leptoquark interactions and consequences for GUTs*, JHEP **11** (2011) 002, arXiv:1107.5393.

[68] C. Bobeth and A. J. Buras, *Leptoquarks meet ε'/ε and rare Kaon processes*, JHEP **02** (2018) 101, arXiv:1712.01295.

[69] E. Goudzovski *et al.*, *New Physics Searches at Kaon and Hyperon Factories*, arXiv:2201.07805arXiv:2201.07805.

[70] C. Marin Benito, L. Garrido Beltran, and X. Cid Vidal, *Feasibility study of $K^0_S \to \pi^+\pi^-e^+e^-$ at LHCb* , tech. rep., CERN, Geneva, 2016.

[71] D. A. Berningho, J. Albrecht, and V. Gligorov, *Internal Analysis Note: Bremsstrahlung Recovery of Electrons using Multivariate Methods*, Tech. Rep. LHCb-INT-2016-018 (2016).

[72] A. A. Alves Junior *et al.*, *Prospects for Measurements with Strange Hadrons at LHCb*, JHEP **05** (2019) 048, arXiv:1808.03477.

[73] L. Anderlini *et al.*, *The PIDCalib package*, tech. rep., CERN, Geneva, 2016.

[74] S. Tolk, J. Albrecht, F. Dettori, and A. Pellegrino, *Data driven trigger efficiency determination at LHCb*, tech. rep., CERN, Geneva, 2014.

[75] Belle Collaboration, Y. Ushiroda *et al.*, *Time-Dependent CP Asymmetries in $B^0 \to K^0_S\pi^0\gamma$ transitions*, Phys. Rev. D **74** (2006) 111104, arXiv:hep-ex/0608017.

[76] LHCb Collaboration, R. Aaij *et al.*, *Angular analysis of the $B^0 \to K^{*0}e^+e^-$ decay in the low-q^2 region*, JHEP **04** (2015) 064, arXiv:1501.03038.

[77] M. Gremm, F. Kruger, and L. M. Sehgal, *Angular distribution and polarization of photons in the inclusive decay $\Lambda_b \to X_s\gamma$*, Phys. Lett. B **355** (1995) 579, arXiv:hep-ph/9505354.

[78] LHCb Collaboration, R. Aaij *et al.*, *Measurement of b hadron fractions in 13 TeV pp collisions*, Phys. Rev. D **100** (2019), no. 3 031102, arXiv:1902.06794.

[79] T. Mannel and S. Recksiegel, *Flavor changing neutral current decays of heavy baryons: The Case $\Lambda_b \to \Lambda\gamma$*, J. Phys. G **24** (1998) 979, arXiv:hep-ph/9701399.

[80] G. Hiller and A. Kagan, *Probing for new physics in polarized Λ_b decays at the Z*, Phys. Rev. D **65** (2002) 074038, arXiv:hep-ph/0108074.

[81] CMS Collaboration, A. M. Sirunyan *et al.*, *Measurement of the Λ_b polarization and angular parameters in $\Lambda_b \to J/\psi\,\Lambda$ decays from pp collisions at $\sqrt{s} = 7$ and 8 TeV*, Phys. Rev. D **97** (2018), no. 7 072010, arXiv:1802.04867.

[82] LHCb Collaboration, R. Aaij *et al.*, *Measurement of the $\Lambda_b^0 \to J/\psi\Lambda$ angular distribution and the Λ_b^0 polarisation in pp collisions*, JHEP **06** (2020) 110, arXiv:2004.10563.

[83] L. M. García Martín *et al.*, *Radiative b-baryon decays to measure the photon and b-baryon polarization*, Eur. Phys. J. C **79** (2019), no. 7 634, arXiv:1902.04870.

[84] BESIII, M. Ablikim *et al.*, *Polarization and Entanglement in Baryon-Antibaryon Pair Production in Electron-Positron Annihilation*, Nature Phys. **15** (2019) 631, arXiv:1808.08917.

[85] M. Pivk and F. R. Le Diberder, *SPlot: A Statistical tool to unfold data distributions*, Nucl. Instrum. Meth. A **555** (2005) 356, arXiv:physics/0402083.

[86] G. Barrand *et al.*, *GAUDI - A software architecture and framework for building HEP data processing applications*, Comput. Phys. Commun. **140** (2001) 45.

[87] D. J. Lange, *The EvtGen particle decay simulation package*, Nucl. Instrum. Meth. A **462** (2001) 152.

[88] GEANT4, S. Agostinelli *et al.*, *GEANT4–a simulation toolkit*, Nucl. Instrum. Meth. A **506** (2003) 250.

[89] G. Corti *et al.*, *Software for the LHCb experiment*, IEEE Trans. Nucl. Sci. **53** (2006) 1323.

[90] T. Sjostrand, S. Mrenna, and P. Z. Skands, *A Brief Introduction to PYTHIA 8.1*, Comput. Phys. Commun. **178** (2008) 852, arXiv:0710.3820.

[91] LHCb Collaboration, M. Clemencic *et al.*, *The LHCb simulation application, Gauss: Design, evolution and experience*, J. Phys. Conf. Ser. **331** (2011) 032023.

[92] D. Müller, M. Clemencic, G. Corti, and M. Gersabeck, *ReDecay: A novel approach to speed up the simulation at LHCb*, Eur. Phys. J. C **78** (2018), no. 12 1009, arXiv:1810.10362.

[93] LHCb Collaboration, R. Aaij *et al.*, *Test of lepton universality with $\Lambda_b^0 \to pK^-\ell^+\ell^-$ decays*, JHEP **05** (2020) 040, arXiv:1912.08139.

[94] L. Breiman, J. H. Friedman, R. A. Olshen, and C. J. Stone, *Classification and regression trees*, Wadsworth international group, Belmont, California, USA, 1984.

[95] Y. Freund and R. E. Schapire, *A Decision-Theoretic Generalization of On-Line Learning and an Application to Boosting*, J. Comput. Syst. Sci. **55** (1997), no. 1 119.

[96] T. Chen and C. Guestrin, *XGBoost*, in *Proceedings of the 22nd ACM SIGKDD International Conference on Knowledge Discovery and Data Mining*, ACM, aug, 2016. doi: 10.1145/2939672.2939785.

[97] F. Pedregosa *et al.*, *Scikit-learn: Machine learning in python*, .

[98] LHCb Collaboration, R. Aaij *et al.*, *Measurement of the b-quark production cross-section in 7 and 13 TeV pp collisions*, Phys. Rev. Lett. **118** (2017), no. 5 052002, arXiv:1612.05140, [Erratum: Phys.Rev.Lett. 119, 169901 (2017)].

[99] HFLAV, D. Asner *et al.*, *Averages of b-hadron, c-hadron, and τ-lepton properties*, arXiv:1010.1589.

[100] T. Skwarnicki, *A study of the radiative CASCADE transitions between the Upsilon-Prime and Upsilon resonances*, PhD thesis, Cracow, INP, 1986.

[101] LHCb Collaboration, R. Aaij *et al.*, *Measurements of the $\Lambda_b^0 \to J/\psi\Lambda$ decay amplitudes and the Λ_b^0 polarisation in pp collisions at $\sqrt{s} = 7$ TeV*, Phys. Lett. B **724** (2013) 27, arXiv:1302.5578.

[102] G. J. Feldman and R. D. Cousins, *Unified approach to the classical statistical analysis of small signals*, Phys. Rev. D **57** (1998) 3873.

[103] D. M. Straub, *flavio: a Python package for flavour and precision phenomenology in the Standard Model and beyond*, arXiv:1810.08132.